Progress in Materials Science Vol. 33, pp. 223–315, 1989
Printed in Great Britain.

0079-6425

NANOCRYSTALLINE MATERIALS

H. Gleiter
Universität des Saarlandes und Institut für Neue Materialien, Gebäude 43,
D-6600 Saarbrücken, F.R.G.

CONTENTS

1. INTRODUCTION

In materials science and solid state physics progress has been made in many cases by one of the following two approaches. Either by developing and applying new methods of investigation or by preparing materials with novel structural features and/or properties. Transmission electron microscopy, Mössbauer spectroscopy, and tunneling microscopy are examples for the first approach. The discovery of metallic glasses, high temperature superconductors or quasi-crystals represent developments resulting in materials with novel structural features and/or properties. In the case of nanocrystalline materials, the generation of solids with new atomic structures and properties was attempted by utilizing the atomic arrangements in the cores of defects such as grain boundaries, interphase boundaries or dislocations.

1.1. *Basic Ideas*

The state of lowest free energy of a solid at low temperature is the perfect crystal, i.e. a three-dimensional periodic or quasi-periodic array of atoms.* However, since the early part of this century it is known that solids deviating from this perfectly ordered structure may exhibit attractive features. In fact, numerous structural studies of solids have revealed a wide variety of deviations. The various deviations may be divided in the following two classes. The first class is obtained by thermally disordering the crystalline structure of a material and by freezing-in the disordered state by means of quenching. Glasses, e.g. vitreous quarz obtained by rapidly solidifying the melt, the partially or fully disorder state of ordered alloys generated by quenching the disordered material from high temperatures or the frozen-in orientational disorder in certain molecular compounds, are structures belonging to this category. As an example, a two-dimensional hard sphere model of a glass is shown in Fig. 1 in comparison to a perfect crystal of hard spheres (Fig. 2). In most materials with glassy structures, the density and the nearest neighbor coordination varies typically by a few percent relative to the perfect crystal.

In the second class of disordered materials, the deviation from the perfect crystal is induced by incorporating defects such as vacancies, dislocations, grain or interphase boundaries. As may be seen from Figs 3, 4 and 5, the atomic displacements associated with the incorporation of defects significantly alters the atomic density and coordination in the defect core region. For example, the atomic density in the core region of grain boundaries is reduced typically

*In the case of certain polymeric solids, steric reasons prevent the formation of perfect crystals, e.g. due to bulky atactic side groups.

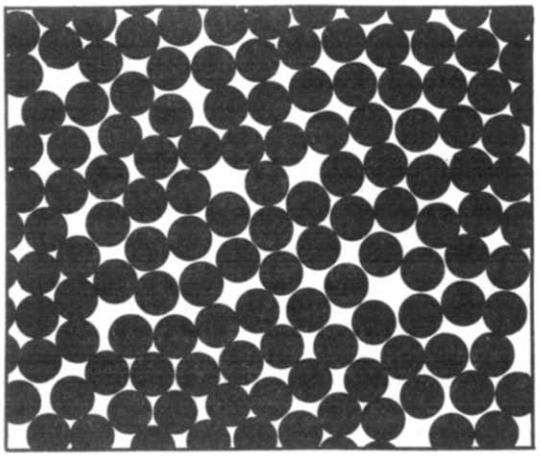

FIG. 1. Hard sphere mode of a two-dimensional glassy structure. The atomic density and nearest neighbor coordination is slightly changed relative to the perfect crystal lattice (Fig. 2).

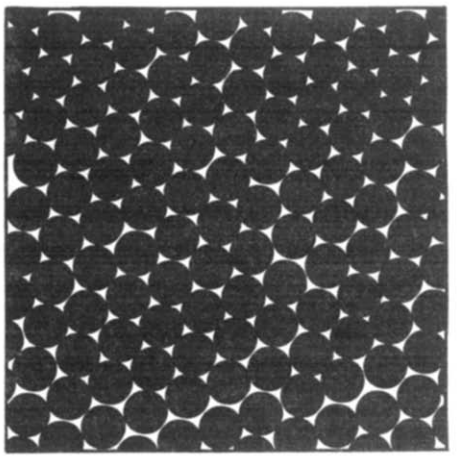

FIG. 2. Hard sphere model of the two-dimensional structure of a perfect crystal (hexagonal array of atoms).

by about 15 to 30% (cf. Figs 4 and 5 or Ref. 14) which is almost an order of magnitude more than the density difference between the glassy and crystalline state in most materials. The structural changes, caused by the incorporation of defects, differ from the structural changes obtained by freezing-in the high temperature atomic arrangement of the same material because both structures have different physical origin. The high-temperature structure is due to the thermal energy stored in the material whereas the defect core structure is caused by the incompatibility introduced into the lattice in the form of a defect and does not require any thermal energy. In fact, in the specific case of grain boundaries, there is ample experimental and theoretical evidence[15] that the atomic structure of the boundary core is a two-dimensional periodic arrangement of atoms (cf. Figs 4 and 5). It cannot be described in the form of a thin disordered or liquid-like glassy

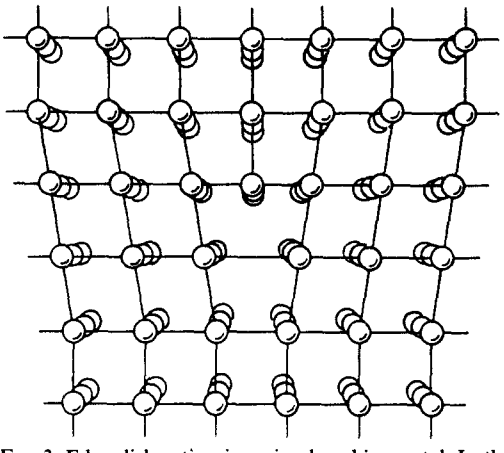

FIG. 3. Edge dislocation in a simple cubic crystal. In the dislocation core, the atomic density and coordination is changed in comparison to the perfect cubic lattice.

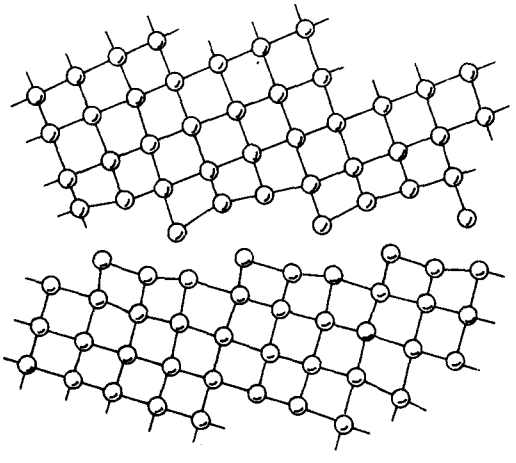

FIG. 4. Atomic structure of a $\Sigma = 5$, 310 grain boundary in NiO deduced from the high resolution electron micrograph shown in Fig. 5, section A.[14]

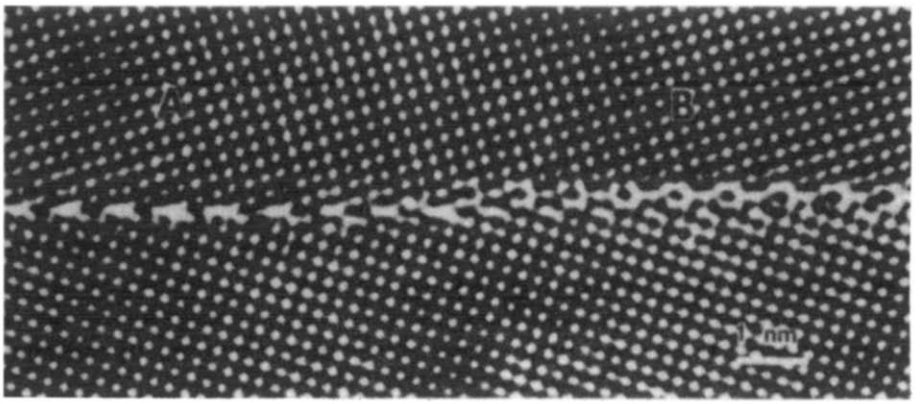

FIG. 5. Electron micrograph of a symmetric $\Sigma = 5$, 310 grain boundary in NiO.[14] The black regions represent the atomic positions. In the boundary core the atomic density and coordination is changed in comparison to the perfect lattice The boundary structures in the facets A and B are different due to the vertical displacement of the boundary plane relative to the two crystals.[14]

layer which indicates in another way the difference between thermally induced disorder and the structural changes induced by incorporating defect cores. As a matter of fact, the boundary core structure is the atomic arrangement of minimum energy in the potential field of the adjacent crystals. As a consequence, the boundary core structure depends on the interatomic bonding forces and the boundary crystallography (i.e. the misorientation between both crystals, the boundary inclination and the translational position of both crystals relative to one another). Hence in any given material (e.g. NiO) a very large variety of grain boundary core structures exist. One example is shown in Fig. 5. The small vertical displacement of the boundary plane in the section A relative to the section B results in two different core structures although all other parameters (crystal misorientation, boundary inclination, etc.) are unaltered. In conventional polycrystals (grain size typically $\geqslant 1\ \mu$m) the atomic structures of the boundary cores are not noticed in most structural investigations such as X-ray diffraction, EXAFS, spectroscopic studies, because the fraction of atoms located in the core of the boundaries is 10^{-4} or less. However, if one generates a material which contains such a high density of defects that 50% or more of the atoms are situated in the cores of defects, then the atomic structure of the entire material depends on the core structures of the defects.

It is the basic idea[1] of nanocrystalline materials to generate a new class of disordered solids by introducing such a high density of defect cores that 50% or more of the atoms (molecules) are situated in the cores of these defects. Depending on the type of defects utilized (grain boundaries, interphase boundaries, dislocations, etc.) nanocrystalline materials with different structures may be generated. Nevertheless, all of these materials have the following microstructural feature in common.[1,2,4–6] They consist of a large volume fraction of defect cores and (strained) crystal lattice regions. As an example, Fig. 6 shows the structure of a two-dimensional nanocrystalline material. The crystals are represented by hexagonal arrays of atoms with different crystallographic orientations. Hence the atomic structures of the core regions of the various boundaries between the crystals are different because their structure depends on the crystal misorientations and boundary inclinations. The boundary core regions (open circles, Fig. 6) are characterized by a reduced atomic density and interatomic spacings deviating from the ones in the perfect lattice. The physical reason for the reduced density and the non-lattice spacings between the atoms in the boundary cores

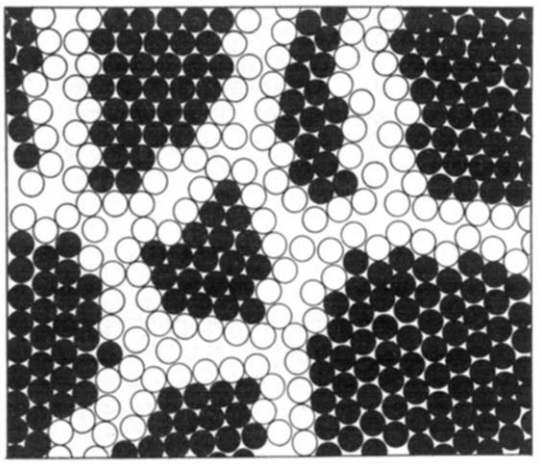

FIG. 6. Atomic structure of a two-dimensional nanocrystalline material. The structure was computed by following the procedure given in Ref. 13. The interaction between the atoms was represented by a Morse potential fitted to gold (cf. Ref. 13). The atoms in the centers of the "crystals" are indicated in black. The ones in the boundary core regions are represented by open circles.

is the misfit between the crystal lattices of different orientation joined along common interfaces.* In other words, the nanocrystalline system preserves in the crystals, a structure of low energy at the expense of the boundary regions which are regions at which all the misfit is concentrated so that a structure far away from equilibrium is formed. A structure of similar heterogenity is not formed in thermally induced disordered solids such as glasses. The misfit between the crystals not only reduces the atomic density in the interfacial region in comparison to the perfect lattice but also causes strain fields to extend from the boundary core regions into the crystallites. These strain fields remove the atoms from their ideal lattice sites. The amount of atomic displacement depends primarily on the interatomic potential. Hence different materials are expected to exhibit different atomic structures in the nanocrystalline state.

So far, all published studies of nanocrystalline materials have focused attention on nanocrystalline materials obtained by introducing a high density (typically 10^{19} per cm^3) of grain (or interphase) boundaries. In order to achieve such a high boundary density, a crystal size of a few nanometers (10 nm or less) is required. Nanocrystalline materials have also been called ultra-fine grained materials,[1] nanophase materials[5] or nanometer-sized crystalline materials.[3]

In order to limit the length of this review, we shall focus attention primarily on equiaxed nanocrystalline, bulk materials and thus exclude multilayer and filamentry nanometer-sized structures as well as thin films. At the end of this review a brief section will be added on an apparently newly emerging field of nanometer-sized structures called nanoglasses.[10–12] The development of our understanding of nanocrystalline material has been documented in several reviews.[2,4–10,16] These reviews clearly indicate that many of the studies performed so far are hampered by difficulties typical to newly developing areas; for example, by difficulties

*The atomic density in the boundaries of a nanocrystalline material is probably lower than in bicrystals or polycrysals with large crystal sizes due to the limited rigid body translations[13] in nanocrystalline materials. The boundaries of different atomic structure formed on opposite sides of a nanometer-sized crystal in a nanocrystalline material, require different rigid body translations to maximize the atomic density in both interfaces. If the crystal size is a few nanometers, the different rigid body translations would require unrealistic elastic distortions of the small crystal. This is not the case in bicrystals or coarse-grained polycrystals.

in specimen preparation, by a lack of reliable methods for specimen characterization and by the present limitations in modeling such systems theoretically.

The paper is organized as follows. Section 2 deals with the methods available to generate nanocrystalline materials. In the subsequent sections the structure (microstructure, atomic arrangement, Section 3) and the properties of nanocrystalline materials (Section 4) will be considered.

2. Synthesis

So far, the synthesis of nanocrystalline materials has been carried out most frequently by assembling pre-generated small clusters by means of *in situ* consolidation and sintering. Thus, we shall first review the various techniques belonging to this category. Subsequent sections will be devoted to the procedures which do not require pre-generated clusters. For reviews of the synthesis of small crystals we refer to Refs 17–24.

2.1. *Generation of Nanometer-Sized Clusters*

The techniques for the generation of nanometer-sized clusters may be divided into three broad categories:[17] vacuum, gas-phase and condensed-phase synthesis.

2.1.1. *Vacuum synthesis*

2.1.1.1. *Sputtering.* When ions of a suitable substance (for example, those of Ar or Kr), accelerated to high energies, are directed toward a surface, atoms and clusters, both neutral and ionic, are ejected. This method of vaporizing materials is called sputtering. The ratio of atoms to clusters and ions to neutrals produced depends on the mass and energy of the projectile ion and a variety of other experimental parameters. Today, primarily two types of sputtering sources are in use. Energetic ions are produced in an ion gun and accelerated toward the surface of the target material.[25] Clusters are ejected directly from the surface as a small fraction of the overall material sputtered. The fraction of atoms incorporated in the large-sized clusters produced with this source is rather low, typically 10^{-4} or less of the total number of atoms sputtered.

Alternatively, hollow cathode sputtering may be utilized.[26] The material to be vaporized is fabricated into a cylindrical cup perforated at one end. A coaxial electrode is placed within the cup and a high voltage is imposed between the cylinder and the internal electrode so as to make the former the cathode. When gas is passed through the system, a discharge is struck and the ionized gas (largely in the form of cations) is accelerated toward the inner surface of the cylinder, vaporizing a portion of it. The vapor is confined for a period of time within the hollow cathode, and if it becomes supersaturated, cluster growth can occur. Lineberger *et al.*[27] have used such a source effectively to make and study clusters.

A drawback to sputtering is that it usually produces small amounts of clusters and cluster intensity distributions that decrease exponentially with increasing cluster size. Most applications of this technique are for cluster ion formation inside or in proximity to a mass spectrometer. In a few cases, notably carbon and silicon, sputtering yields broader distributions of cluster ions.

2.1.1.2. *Laser ablation.* This technique uses high-power pulsed lasers to vaporize cluster ions from solid surfaces. The wavelength of the laser light has to be adjusted to the material.

For the ablation of metals, UV-lasers (e.g. excimer lasers) are required as the reflectivity of many liquid metal surfaces in the IR or visible regime is close to 100%. In one application,[28] laser ablation was utilized directly inside a Fourier-transform ion-cyclotron-resonance mass spectrometer, allowing monitoring of the cluster ions and their reaction products with an introduced reagent gas.

2.1.1.3. *Liquid-metal ion sources.* Liquid-metal ion sources are typically formed by a small tungsten wire with its tip shaped to a radius of a few microns and wetted with a metal above its melting point. When this tip is brought to a few kilovolts potential with respect to a grounded aperture, the liquid is pulled up into a cone as the electrostatic forces exceed the surface tension forces of the liquid. With the very high electric field at the end of the cone, ions are emitted by field evaporation. Atomic ions are the primary emitted species, but there is also significant emission of ionized clusters and even ionized droplets. These sources work for those metals whose vapor pressures are sufficiently low at their melting points not to interfere with maintaining the extraction voltage, e.g. Au, Ga and In.

The production of ionized clusters (droplets) from liquid-metal ion sources is rather like an ink-drop printer with a metal ink. A micron diameter beam of focused charged gold droplets has been realized in France[29] and the writing of metallic lines with such a beam has been suggested.[17] Because the droplets contain millions of atoms each, the deposition rate might be attractive, even in this serial pixel mode of pattern formation. Not much has yet been done to characterize the material produced with this kind of beam.

2.1.2. *Gas-phase synthesis*

2.1.2.1. *Inert gas condensation.* In the case of inert gas condensation the aggregation of volatilized monomers into clusters is achieved by (1) establishing a monomer population, (2) "cooling" the monomers by collisions with "cold" inert gas atoms, and (3) growth of clusters both by addition of monomer to individual clusters and by aggregation due to collisions between clusters. So far, oven sources, sputtering sources, electron gun evaporation, laser evaporation, pyrolysis, hydrolysis or supersonic expansion have been utilized.

2.1.2.2. *Oven sources.* The simplest technique for establishing a monomer population is by means of a heated crucible or oven. A wide variety of oven-based sources has been developed. Direct evaporation into a gas to produce an aerosol or smoke of clusters has been extensively studied by several groups.[30,31] Near the source, small clusters of fairly uniform size are observed. Farther from the source the clusters become larger with a broader size distribution. Finally, at some limiting distance from the oven, which depends on inert gas pressure and evaporation rate, the clusters reach a limiting size which increases with increasing evaporation rate and with the atomic weight of the inert gas.

The mean cluster size in such a source can be controlled by varying the evaporation rate from the oven and the pressure of the inert gas in the evaporation chamber. Clusters with mean diameters as small as 3–4 nm have been generated by this process. The clusters exhibit a log-normal size distribution. Such a distribution is characteristic of cluster–cluster aggregation which is also suggested by the different morphology of small and large clusters. The mean cluster size can be reduced and the size distribution sharpened by imposing a forced convective flow on the inert gas. Several sources based on this concept have been developed.[32–34] The short residence time of the clusters close to this source reduces cluster–cluster aggregation resulting in smaller clusters and a narrower size distribution. For example, a multiple-expansion cluster source[35] produces a size distribution with a constant full width

at half maximum of less than 0.5 nm and a controllable mean size ranging from less than 1 nm to approximately 5 nm.

Naturally, sublimation may also be utilized instead of evaporation for solids with high vapor pressures. This applies, for example, to MgO which has been heated in 200 Pa of He to temperatures of around 1,600°C (MgO melts at 2,852°C).[36] The material which sublimes was found to be oxygen deficient, but is fully converted to stoichiometric MgO by subsequent exposure to oxygen introduced into the vacuum chamber.

Oven-based sources suffer from the following drawbacks. The temperature limitations imposed by the oven or crucible material; chemical reactions occur between many metals and the frequently used refractory metal crucibles; inhomogeneous temperature distributions exist in the molten metal leading to unsatisfactory control and reproducibility; the production of alloy clusters is restricted by the different activities of the constituents; evaporation of technologically interesting ceramics such as Al_2O_3 is limited by the oxidation of refractory boats.

The preparation of oxide ceramics by oven-based sources has been achieved by evaporating the metallic component (Ti, Fe) in He so that a nanometer-sized metal powder was obtained. The loose metallic powder was subsequently oxidized by introducing oxygen (typical pressure 2 kPa) into the chamber.[37–40] X-ray diffraction of the as-prepared TiO_2 samples showed[40] that the stable rutile phase was the only phase present, with no evidence for unreacted Ti or other Ti-oxide phases. The composition of the sample was determined by Rutherford backscattering analysis to be oxygen deficient in the as-prepared state, $TiO_{1.7}$, but after sintering at 300°C it became nearly stoichiometric, $TiO_{1.95}$. At the same time, the color of the sample changed from black to white, the normal color of bulk rutile.[40]

Naturally, post oxidation is not limited to fully oxidized particles. For example, oxidation of small Al, Zn or Mg crystals has been utilized to generate nanometer-sized particles with metallic cores and oxidized surfaces. The method of reacting small metallic particles with a gaseous phase has been applied to generate nanometer-sized hydride particles (e.g. TiH_2) by evaporating the metallic component in an H_2 atmosphere of 50 kPa.[41] Subsequent heating of the TiH_2 particles (400°C, 1 min, vacuum) converted them into Ti with hcp-structure. Re-hydrogenation into TiH_2 was achieved by annealing the particles at 250°C for 5 min at 10 kPa H_2 pressure. Iwama and coworkers[42] have succeeded in producing a variety of transition-metal nitrides in ultrafine powder form by evaporating metals in either N_2 or NH_3 gas.

Recent experiments revealed that, at least in one case, control of the inert gas pressure affects not only particle size, but also the phase of the resulting material.[43] Ultrafine powders of Ti were found to react with oxygen to form rutile (TiO_2) particles of average diameter 12 nm, if He pressures of greater than 500 Pa were present during evaporation. However, if the He pressure used was less than 500 Pa and greater than about 10 Pa, small Ti particles were still formed, but these particles did not form rutile when exposed to oxygen. Instead, in this case, an unexpected amorphous phase was formed. While the reason for this unusual behaviour in Ti is not yet understood, what is clear is that this demonstrates that phase control using nanocrystalline processing is a potential future materials engineering application. Unexpected new phases of erbium oxides have also been produced via the nanocrystalline processing route.[44] In fact, compacted nanocrystalline erbium oxide (10 nm grain size) was found to be composed of two fcc forms of erbium oxides, one of which is a new fcc erbium sesquioxide with $a = 0.374$ nm, and a new Er_2O_3 phase with a monoclinic structure. This latter phase can be regarded as a distorted hexagonal structure caused by absorbing oxygen into the lattice of erbium during oxidation.

2.1.2.3. *Sputtering.* DC and RF magnetron sputtering have become standard procedures in thin film preparation. In fact, they can be applied equally well for the deposition of metals, metallic alloys, semiconductors and ceramics. Therefore, sputtering seems suitable for the production of nanocrystalline materials. The normal operating pressure of sputter sources (10^{-1} to 10^{-2} Pa), however, is several orders of magnitude lower than the pressure range required for particle formation during inert gas condensation in laboratory size evaporators (10^2 to 10^3 Pa). Relatively few data are available on sputtering yields in the pressure range of interest, although some pioneering work[45] has shown that simple diode sputtering could be used to produce ultrafine particles in the desired size range. Sputtering at such high pressures is possible since the width of the dark space in the plasma is inversely proportional to the gas pressure so that the number of collisions between accelerating ions and gas atoms in the dark space is independent of gas pressure. In addition to its wide applicability, sputtering has other advantages over most thermal evaporation techniques:

(i) The composition of the sputtered material is the same as that of the target, making alloy synthesis possible.
(ii) The sputtering conditions are stable and readily controllable by means of the plasma current.
(iii) The heat load on the chamber walls is far smaller than during thermal evaporation, reducing outgasing and subsequent impurity incorporation by the small particles.

The application of a commercially available magnetron sputtering device for preparation of metallic and ceramic clusters (Al, Mo, W, $Cu_{91}Mn_9$, $Al_{52}Ti_{48}$, TiO_2, NiO and ZrO_2) with diameters of 7 to 50 nm has been studied recently.[46,47]

2.1.2.4. *Laser ablation.* In the case of laser ablation, a high-power laser beam ablates a sample target located in an inert gas chamber. The resulting plume of metal, believed to be mostly neutral atoms, is entrained and cooled by the carrier gas, resulting in the required supersaturation and cluster growth. Metal densities are usually low enough that growth is dominated by successive monomer addition. Resulting cluster size distributions are broad.

The laser vaporization technique is general and versatile. Virtually any material that can be fabricated into an appropriate target may be used. Clusters of semiconductors,[48] transition metals[49] and main group metals[50] have all been generated in this way. Alloy targets have been used, and in general the clusters show the expected statistical distribution of atoms.[51] Another procedure combines laser vaporization of one metal with simultaneous laser pyrolysis of a gaseous precursor of another metal.[52] This precursor is mixed with the carrier gas so that both types of monomers are present in the clustering region. In this way, mixed clusters of elements that do not normally alloy can be prepared. Such clusters, as well as macroscopic materials made from them, may be found to have novel properties.

A modified, novel version of the laser ablation approach was recently utilized[53] to synthesize nanocrystalline composites of metallic and non-metallic species. A heated tungsten filament was simultaneously employed for evaporation and codeposition of W via chemical transport mechanisms. This process occurs in a reducing environment of hydrogen gas, where the evaporated species were produced by a laser-induced plume. Composite layers were formed on a Ni alloy substrate surface, at a rate of about 1 μm/sec. The matrix of the composite films was either Al or W, and the dispersed phase was amorphous silica fibers. The diameter of the fibers was between 25 nm and 120 nm, depending on the interaction times.

2.1.2.5. *Pyrolysis.* Laser pyrolysis is a technique designed to synthesize ultrafine refractories by rapidly heating with a laser a flowing reactant gas mixed with an inert carrier. This leads to rapid gas-phase decomposition of the reactants and produces a saturated vapor of the desired constituent atoms. Nucleation and growth of clusters then occur as the decomposition products are quenched by collisions with the atoms (molecules) of the carrier gas. The technique has been used[54] to synthesize ultrafine powders of Si, Si_3N_4, and SiC. ZrB_2, $FeSi_2$ B_4C, TiB_2 TiO_2, Al_2O_3 and TiO_2 have been obtained by a similar approach.[55–57] The synthesis of non-metals uses volatile hydrides, with H_2 as the by-product. Compounds of non-metals are produced by adding to the gas mixture ethylene to yield the carbide, ammonia to yield the nitride, etc.

Metals and compounds of metals, as well as complex compounds of non-metals, require a different approach. The metals are incorporated into compounds which are volatile under the experimental conditions. This is usually done with organometallic compounds, or with metal carbonyls. Rice and Woodie[58] have synthesized Si/N/C powder of 100 nm diameter spheres from the pyrolysis of $Me_3SiNHSiMe_3$. WC and W/C/O, as well as MoS_2 and MoS_2C_x, have all been synthesized by this approach; doping these materials with Co or Zn was also achieved. Unique FeC catalysts have also been synthesized by this procedure.[59]

Laser pyrolysis has the advantage of being a continuous process, which is scalable with laser power and reactant flow rate. The cost of materials produced by this approach is primarily determined by the cost of the chemicals.

The approach could be extended by the use of UV lasers, where photochemical decomposition may be utilized to produce the intermediates. This would lead to a low-temperature, supersaturated vapor where it is more likely that metastable phases will aggregate and be stabilized.

2.1.2.6. *Flame hydrolysis.* Flame hydrolysis is the reaction of volatile compounds, e.g. $TiCl_4$ or $SiCl_4$, in an oxygen–hydrogen flame. It leads to highly dispersed oxide clusters and has been applied to a wide variety of compounds[60–63] such as SiO_2, Al_2O_3, TiO_2, ZrO_2, Bi_2O_3, Cr_2O_3, Fe_2O_3, NiO, GeO_2, V_2O_5, etc. The major advantages of this technique are high purity, chemical flexibility, and the possibility to synthesize mixed oxides. Depending on the process condition, cluster sizes between 5 and 50 nm are obtained.

2.1.3. *Condensed-phase synthesis*

2.1.3.1. *Metals.* If a reducing agent is added to an acidic aqueous solution of metal ions, then small neutral metal clusters will form. Dialysis can be used to remove remaining ions and a thickener, such as gelatine, can be added to prevent aggregation of the particles. Relatively narrow size distributions have been achieved with this technique (e.g. Ag,[64] Au,[65] Pt[66]) with rough control of the mean cluster size similar to those achieved with inert-gas condensation.

The method of the growing small metal clusters by means of the microelectrode method has been utilized in recent years to generate small Ag clusters.[22,130] A solution containing a few 10^{-4} M Ag^+ ions was exposed to a short pulse of radiation producing a known amount of hydrated electrons in the 10^{-6} M range. The latter rapidly react with silver ions to form atoms, $Ag^+ + e_{aq}^- \rightarrow Ag^0$, which subsequently agglomerate to larger particles. At a certain particle size, i.e. after a certain time of agglomeration, metallic silver colloid was present, recognizable by the appearance of the 380 nm plasmon absorption. In a second study,[131] sulfonatopropylviologen (SPV) was used. The pulse of radiation produces known amounts of the radical anion SPV^- and of Ag^0 atoms. The Ag atoms agglomerate

into silver particles and grow further by the reaction $SPV^- + Ag^+ + Ag_n \rightarrow SPV + Ag_{n+1}$. Small gold clusters have been grown by a closely related method.[132] A solution containing 1.7×10^{-4} M $NaAu(CN)_2$ was exposed for 0.5 s to high-energy electrons. Under these circumstances all the gold complexes were reduced by hydrated electrons to yield gold atoms, $e_{aq}^- + Au(CN)_2^- \rightarrow Au^0 + 2CN^-$. One second after the electron irradiation occurred, the plasmon band typical of Au clusters was present. About 2 s later, indications of larger gold particles were noticed suggesting rapid particle growth. Metal clusters are generally short-lived in aqueous solution as they rapidly agglomerate. Hence, stabilization of intermediate cluster sizes would be of interest for the controlled growth of metal clusters of a pre-determined size. Such a stabilization has recently been achieved in the case of silver clusters formed in the radiolytic reduction of Ag^+ ions in the presence of sodium polyphosphate.[133] The latter is known to be an excellent stabilizer for many inorganic colloids. In this experiment, a solution containing 2×10^{-4} M Ag^+ ions, 2×10^{-4} M polyphosphate, and 0.1 M 2-propanol was γ-irradiated. Under these conditions, reducing radicals, i.e. hydrated electrons and 1-hydroxymethylethyl radicals, were generated which reduce the silver ions.

Colloidal suspensions of metal clusters in organic solvents have also been generated by depositing metal atoms into low-temperature organic solvents.[67] Cluster growth is eventually inhibited by strongly bound solvent molecules.

Furthermore, spark erosion has been utilized as a method for producing fine powders of metals, alloys, semiconductors, and compounds.[68] The technique involves maintaining repetitive spark discharges among chunks of material immersed in a dielectric liquid. As a result of the spark discharge there is highly localized melting or vaporization of the material. The powders are produced by the freezing of the molten droplets or the condensation and freezing of the vapor in the dielectric liquid. The powders are quenched *in situ* to the temperature of the liquid. Particles can be produced in sizes ranging from 5 nm to 75 μm. The average powder size and production rate depend on the power parameters, the material used, and the dielectric liquid.

The generation of metallic clusters by precipitation from a solid crystalline or glassy matrix has been used for numerous studies on isolated clusters.[139,151,152] In a few cases it has been possible to dissolve the matrix selectively without dissolving the clusters resulting in a colloidal suspension of clusters in the solvent.

2.1.3.2. *Semiconductors.* By control of temperature, concentration, and solvent during liquid phase precipitation of compound semiconductors it has become possible to make and stabilize crystallites with diameters < 5 nm.[69] Better size control and colloid stability can be achieved through the use of microscopically structured liquid mixtures, such as water–soap–heptane, in which the crystallites are stabilized in small (2–10 nm) water pools[70] termed "inverse micelles".

Small semiconductor clusters can also be prepared inside ionomers. Ionomers are a class of copolymers containing ionic side-chain groups such as COO^- and SO_3^-. These ionic groups tend to aggregate together forming domains, analogous to the formation of ionic pools in micelles. Metal ions, such as Cd^{2+} and Pb^{2+}, can be easily exchanged into these ionic domains where synthesis of desired semiconductor clusters can be conducted. For example, stable PbS clusters, ranging in sizes from mono-molecular to bulk, have been synthesized in ethylene-15% methacrylic acid copolymer.[71]

Silicate glasses have been used as hosts for the high-temperature synthesis of semiconductor clusters such as CdS_xSi_{1-x} and CuCl. In the case of CdS_xSe_{1-x} doped glasses, which are available as commercial color filters, elementary Cd, S and Se are first dissolved in the glass

melt in the presence of excess amounts of Zn. After the glass is formed upon cooling, CdS_xSe_{1-x} crystallites of various sizes can then be produced by controlled annealing.[72]

2.1.3.3. *Ceramics.* Decomposition and precipitation reactions in ionic materials have been utilized to generate nanometer-sized clusters. For example, decomposition of $Mg(OH)_2$ and $MgCO_3$ yielded MgO clusters with about 2 mm diameter.[73–75] The solution sol–gel method has been utilized in a variety of systems to generate small (< 10 nm) clusters of SiO_2, Al_2O_3, TiO_2.

Hydrothermal reactions (reactions of the water above its boiling point) have been proposed to be applied to synthesize small clusters.[60] The two reactions applied so far are hydrothermal precipitation and hydrothermal oxidation.[78] Both reactions yield suspensions of crystalline metal oxides in water. Simple oxides (ZrO_2, SiO_2, Al_2O_3, TiO_2, MgO, CaO), as well as mixed oxides (ZrO_2–Y_2O_3, ZrO_2–Y_2O_3–MgO, ZrO_2–MgO, ZrO_2, ZrO_2–Al_2O_3, $BaFe_{12}O_{19}$, $BaTiO_3$), have been prepared in the size ranges between 10 nm and 100 nm.

2.1.4. *Capped clusters*

In order to isolate macroscopic amounts of clusters from the liquid-phase reaction media, it is necessary to modify chemically the bare surface to prevent cluster fusion. Polymeric, highly ionic, inorganic phosphates have been used[79] to protect powders of Cd_3P_2, CdS, etc., which could then be re-dispersed in water. A direct organometallic synthetic method for surface reactions on clusters has recently been achieved in inverse micelle colloidal preparations.[180] This method chemically bonds organic groups to chalcogenide atoms on the cluster surface. The surface changes from hydrophilic to hydrophobic, and as a result the clusters precipitate as a pure, capped, cluster powder. They re-dissolve in typical organic solvents, can be dispersed in polymer films, and in general could be used in the synthesis of cluster-consolidated material. For example, the powder can be pressed into pellets without fusion of the clusters.

Extremely small monodisperse metal and semiconductor cluster molecules, consisting of 30 atoms or less, can be prepared and crystallized via direct chemical synthesis. Many examples, such as iron sulfur clusters[81] and gold–silver clusters,[82] have been reported in the literature. No attempt is made here to review this area of classical chemical synthesis.

2.1.5. *Cluster arrays*

The goal of this approach is to assemble clusters in well-defined three-dimensional arrays to form new types of solids. The principle of this idea has been demonstrated recently with the synthesis of CdS superclusters inside zeolites. In zeolite Y,[83] discrete $(CdS)_4$ cubes with a CdS bond length of 0.247 nm have been synthesized within the 0.5 nm sodalite cages. They are stabilized by the interaction between Cd atoms and framework O atoms. Cubes in the adjacent sodalite units further interact with each other, via super-exchange through the host lattice, to form an interlocking three-dimensional "supercluster" structure. The optical absorption spectrum of these superclusters lies between those of clusters and bulk. A novel orientational effect has also been observed. By changing the host from zeolite Y to A, the relative orientation of the cubes is changed from vertex-to-vertex to face-to-face. This results in a 0.3 eV blue-shift in the supercluster absorption spectrum, reflecting the change in the geometrical and electronic structures of the superclusters as imposed by the zeolite host. Using different zeolites as the template, superclusters with different structures and electronic properties can be built.

At present, because of the presence of defects in both the zeolite hosts and the semiconductor clusters, CdS superclusters in zeolites are broken into small domains. To

remove this problem, better quality zeolite crystals and improved synthetic procedures are needed.

Another approach toward the same goal was proposed by Umemura.[84] In order to generate a regular array of small particles on a silicon substrate for microelectronic applications such as memories, a two step process has been made. In the first step, a square lattice of carbon was deposited on the Si by means of a narrow electron beam. By depositing subsequently a Au or KCl particle into every square, a regular array was obtained. The accuracy of the lattice is still inferior in comparison to the quality achieved by modern microfabrication methods. If the accuracy can be improved, this approach would open the way to design quantum-well devices. A somewhat related approach is the generation of small particle devices called "superatoms".[85–87] These particles are composed of two semiconductor substances arranged regularly as a core and a shell which resembles functionally the core and electron shell of an atom, respectively. The application of such structures requires the availability of monodisperse small particles.

2.2. *Cluster Deposition*

One approach to fabricate a bulk piece of a nanocrystalline material is to deposit the small clusters generated by one of the methods discussed in the previous section on a solid substrate. The following three methods of cluster depositions have been studied so far.

2.2.1. *High speed deposition*

Kashu *et al.*[88] have deposited nanometer-sized clusters of Ag, Fe, Ni, Cu, Au, Ti, Pb, Zn, TiN and RuO_2 by using clusters entrained in a gas jet (Fig. 7). A glass, metal, or plastic substrate surface located close and normal to the jet is exposed for colliding with the clusters. With a sufficiently high velocity (>100 m/s) of jet flow against the substrate, the clusters had sufficient energy which was released during the collision to make them stick to the substrate and to one another. With a tiny nozzle (≈ 0.3 mm diameter), a line pattern of as-deposited clusters 0.3 mm wide was generated. For the deposit, a green density of over 55% for Ag, Cu, Ni, etc., which corresponds to a conventional powder compact made by using high pressure consolidation was obtained. If a conventional millimeter-sized fine powder was used instead of the nanometer-sized clusters, no solid deposit was formed. Codeposition of different materials, e.g. Ag–Fe, Pb–Zn, from a single nozzle is possible, regardless of the specific density of each component. The microanalysis records indicate uniform distribution

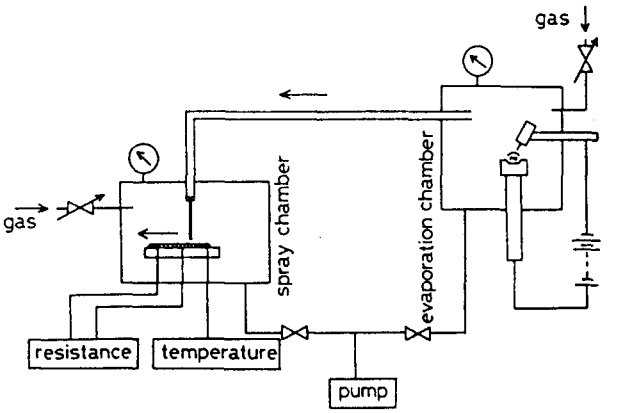

FIG. 7. Arrangement of the "spray deposition" method for small as grown particles.[88]

of the components. The electrical resistivity of a gas-jet deposited Ni pattern was higher than the one of conventional silver paste. The resistivity of a RuO_2 deposit could be manipulated by varying the deposition parameters between $10^{-1}\,\Omega\,cm$ and $\approx 4 \times 10^{-4}\,\Omega\,cm$, which is applicable to commercial applications.[88] The deposition process may be performed at ambient temperature, but a lower temperature carrier gas may also be used if a higher gas flow is employed. In classical metallurgical terms this process seems to be based on low-temperature ballistic consolidation. An interesting, slightly different application of this method is a gas jet containing frozen CO_2 fine particles.[88] The colliding CO_2 particles remove organic films on glass, ceramics, or metal substrates. Solid CO_2 particles have a hardness sufficient to strip-off layers of a photoresist on chromium oxide coated glass, without causing any damage to the chromium oxide coating. Solid CO_2 particles also seem applicable for removal of acrylic or styrene plastics.

2.2.2. *Deposition by ionized cluster beams*

Takagi and Yamada[89,90] have pioneered thin film deposition by "ionized cluster beams". These beams are generated by expanding a vapor beam adiabatically through a nozzle. During expansion, a fraction of the atoms condenses in the form of small clusters containing typically 1,000 atoms. An electron beam post-ionizes a small fraction of the clusters, which can then be accelerated to a deposition substrate with any desired impact energy, typically about 1 eV per atom of the cluster. There is no mass selection; atoms, small clusters, and neutral large clusters as well as the ionized large clusters strike the substrate. The ionized and accelerated clusters are pictured as dissociating at the moment of impact on the substrate, desorbing loosely bonded atoms and impurities and giving mobility to atoms that have already landed at the surface as well as those of the dissociated clusters. In one sense, the ionized cluster beams are an "ion assisted" process, since at most only a few percent of the total amount of material being deposited is believed to consist of ionized clusters. Most of the deposit is probably made up of neutral atoms or perhaps small clusters. Such sources have been utilized to generate thin films, e.g. epitaxial aluminum on silicon,[90] and it is being used commercially for gold mirror coatings.[91]

2.2.3. *Consolidation*

The first attempt to generate and study bulk nanocrystalline materials was based on the collection and consolidation of small clusters.

A schematic picture of an ultra-high vacuum apparatus developed for this purpose is illustrated in Fig. 8.[92–94] At this time, only the inert gas condensation method for producing the particles has been employed for the synthesis of nanocrystalline materials. As shown in Fig. 8, the particles are produced by a two step process. The substance (e.g. Cu) is evaporated by resistivity heating from a refractory metal boat. The evaporated atoms transfer their thermal energy to the inert gas and condense in the form of small crystals. The crystals are carried by a convective current of inert gas to a liquid-nitrogen cooled coldfinger. Subsequently, the inert gas is removed and the particles are scraped from the coldfinger and funneled into a piston and anvil-like device where they are compacted using pressures of about 1–5 GPa. Cooling or heating of the specimen during compaction is easily possible. As a consequence of the clean handling conditions, the powders become partially sintered during compaction and have densities of about 70–90% of the bulk. Clearly, the processing technique allows for great versatility: composite materials can be produced by using two or more evaporaton sources; oxide or other ceramic materials can be produced by mixing or

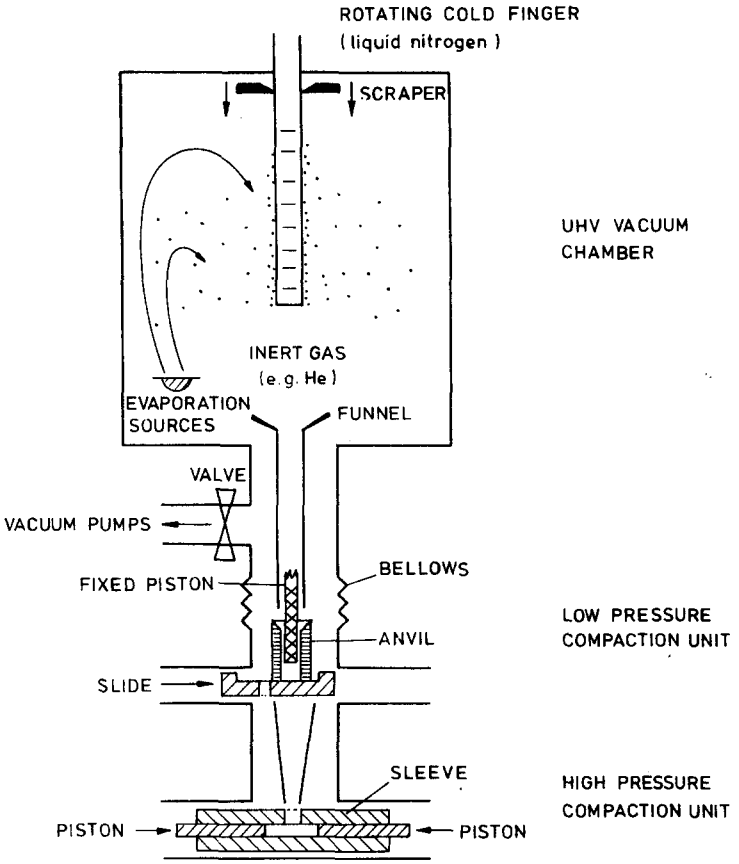

FIG. 8. Schematic drawing of a gas-condensation chamber for the synthesis of nanocrystalline materials.[92-94] The material evaporated condenses in the inert gas in the form of small crystallites and is transported via convection to the liquid-nitrogen filled cold finger. The powder is subsequently scraped from the cold finger, collected via the funnel and consolidated first in the low-pressure compaction device and then in the high-pressure compaction unit. Both units are kept under UHV conditions. If the inert gas is in the chamber, it is separated by a valve from the pumps. Instead of an evaporation device, a sputtering source has been utilized successfully.[46,47]

replacing the inert gas with a reactive gas; particle size can be controlled by the evaporation rate and the condensation gas pressure.[92-94]

Although the general features of synthesis seem to be clear, the detailed processes which take place during compaction and the resulting structure of the material are not yet well characterized. During the collection of the powder on the coldfinger, some particles agglomerate and form grain boundaries; in compound powders, both grain boundaries and heterogeneous interfaces may form. Most interfaces, however, are formed during the compaction process. Before two particles (nanometer-sized crystals) are brought into contact, their atoms lie on regular lattice sites, with possible relaxations at the free surfaces. As contact is made between the two crystals, an interface is formed with an atomic structure controlled by the parameters discussed in the first section.

Further improvements in powder consolidation seem to be possible by utilizing the "core extrusion process" which has been successfully applied to the consolidation of metallic glasses.[95] When a billet of powder, packed into a cylindrical container, is extruded, an

inhomogeneous, porous bulk glassy material was found to result. The homogeneity of the extruded material may be improved by placing a core of a suitable material in the central axis of the container to be extruded. The published observations[95] demonstrate that the coextrusion of the core and the container results in a homogeneous glassy body with a residual porosity of less than 0.1%. The same technique seems applicable to the processing of nanocrystalline materials.

2.3. *Other Methods*

2.3.1. *High-energy milling*

The reduction of grain size in powder samples to a few nanometers during heavy mechanical deformation was investigated by several authors.[96–100] By high-energy ball milling, the grain size of pure bcc metals (Cr, Nb, W), metals with hcp structure (Zr, Hf, Co, Ru) and intermetallic compounds with CsCl structure (CuEr, NiTi, AlRu, SiRu) and immiscible systems (FeAl) can be reduced to nanometer scales. The deformation is localized at the early stage in shear bands with a thickness of about 1 μm. Nanometer-sized grains are nucleated within these shear bands. For longer durations of ball milling this results in an extremely fine-grained microstructure with randomly oriented grains (5–13 nm in diameter) separated by high angle grain boundaries. Thermal analysis of these samples allowed for a quantitative determination of the enthalpy stored in these materials and an estimation of the related grain boundary energies. Excess enthalpies of up to 40% of the heat of fusion and excess heat capacities of up to 20% in comparison to the underformed state have been achieved, exceeding by far any values determined for conventional deformation processes. These values also exceed the energy of grain boundaries in fully equilibrated polycrystals. The values are comparable, however, to the excess enthalpies and the excess heat capacities reported (cf. Section 4.4) for nanocrystalline materials prepared by consolidation of nanometer-sized clusters according to the method discussed in the previous paragraph (Section 2.2.3).

The ball milling method does not seem applicable to metals with fcc structure. If metals with fcc lattice structure are subjected to high-energy ball milling they are found to sinter to larger particles up to one millimeter in size. Fcc metals appear to be too soft for effective energy storage. High-energy ball milling seems also suitable for generating nanocrystalline alloys. For example, using a planetary-ball mill or an attritor allowed Schlump and Grewe[98] to produce an equiaxed crystalline structure with a grain size of < 10 nm in an Fe–Ta–W alloy. Generally they found that systems outside the metastable solid solution field or in the two-phase amorphous/crystalline region could lead to a nanocrystalline structure. Nanocrystalline cermets, such as from Ti–Ni–C, could be produced by the same method. Similar results were obtained by Shingu and coworkers[97] who generated nanostructures in both Al–Fe and Ag–Fe. Here, competition took place between the formation of a nanocrystalline and an amorphous structure. As a matter of fact, it turned out that the chemical composition strongly influenced the amorphization. For example, a small amount of Ti in the Al–Fe system favored the formation of the amorphous phase. Cryomilling (i.e. high-energy ball milling in liquid nitrogen) leads to a matrix of aluminum (for example) with a fine grain size (< 50 nm) of dispersed AlN particles.[99] A major advantage of the mechanical alloying approach to production of nanocrystalline materials is that it is a "quantity" process permitting several kilograms of material to be produced in times of up to 100 hr.[98]

2.3.2. *Mixalloy processing*

The mixalloy processing utilizes the turbulent mixing of impinging alloy streams and *in situ* chemical reactions.[101–103] Two or more turbulent streams of molten metal alloys are directed into a mixing chamber. There the streams impinge at high velocities. Due to the highly turbulent flow, small scale eddies provide rapid and effective mixing and permit chemical reactions on a nanometer scale. For example, if one of the molten streams is a Cu–B alloy and the other stream is a copper alloy containing a strong boride-forming element such as Ti, nanometer-sized TiB_2 crystals are formed in the zone of mixing. Subsequent rapid solidification results in fine-grained material containing nanometer-sized thermally stable dispersions.

2.3.3. *Deposition methods*

During thin film generation, the formation of nanocrystalline structures has been reported by numerous authors. For example, thin films of $Fe_{60}Co_{40}$ produced by *electron beam evaporation* and ultra-high vacuum conditions led to crystal sizes of about 8 mm.[104] The films were shown to consist of the small crystallites and (about 30 vol%) grain boundaries. Thin films produced *by laser breakdown* chemical vapor deposition from nickel and iron carbonyls led to grain sizes smaller than 10 nm.[96] Rapid *solidification* has been demonstrated for several pure metals as well as alloys to result in nanocrystalline structures.[106–108] Furthermore, *electrodeposition* of Ni–P alloys under suitable conditions leads to nanocrystalline structures.[109–112]

In the case of silicon, *chemical transport* in a low-pressure hydrogen plasma has been utilized.[113] The crystal size (and hydrogen content) varied from 5 nm (12%) to 15 nm (1%) as the deposition temperature was increased from 110–400°C. A chemical transport process for generating nanocrystalline, high-strength iron whiskers (crystal size between 5 and 30 nm) was developed.[114,115]

Chemical vapor deposition (CVD) has been utilized to synthesize nanocrystalline materials based on the nitrides and carbides of titanium and silicon.[116] The CVD reactor used was a computer controlled hot-wall reactor. Layered deposits were produced by pulsing the reactant gases judiciously under software control. The development of a columnar structure which is endemic to most CVD materials was suppressed by the above procedure. The same procedure was applied to grow nanocrystalline carbon films and filaments from methane–hydrogen mixtures by RF-plasma assisted CVD. Crystal sizes as small as 2 to 3 nm were obtained.

2.3.4. *Sol–gel method*

Nanometer-sized ceramic structures have been generated by means of a sol–gel technique. Both structural and compositional nanometer structures are obtained by "seeding" of a ceramic precursor with crystalline sols of the final equilibrium phase to catalyse nucleation.[117–127] This process, which consists of introducing crystalline nuclei in a matrix in order to lower the nucleation energy required to form the expected phase, has been known for a long time in the case of liquids and glasses.

A significant advantage of the sol–gel technique in comparison to methods involving high temperatures (e.g. calcination, evaporation) is the low temperature of the method. The preparation of stoichiometric compounds containing one or more components with a high vapor pressure, e.g. Pb in $(BaPb)TiO_3$ ferroelectrics, poses serious problems due to the Pb loss. This difficulty can be avoided by the sol–gel approach. In fact, the specific surface

area of (BaPb)TiO_3 sol–gel derived powders have been found to be about 50 m^2/g in comparison to 4 m^2/g for powders prepared by calcined mixed oxides.[129]

3. Structure

Most of the studies published so far on the structure of nanocrystalline materials have been carried out by using nanocrystalline solids generated by consolidation of small clusters produced by inert gas condensation.

3.1. *Chemical Composition*

Systematic studies of the impurity content of some nanocrystalline metals (Cu, Pd, Fe) have been performed utilizing mass spectrometry, gas chromatography, X-ray fluorescence, atomic absorption spectroscopy, X-ray photoelectron spectroscopy, Auger electron spectroscopy and PIXE analysis. The studies revealed the following impurities.[134–136] Metallic impurities owing to the evaporation process and the compaction procedure lie in the order of 10^{-4} at% up to 5%. In conventional evaporators (no baking) the oxygen content of metallic samples with low oxygen affinity (Pd, Cu) is of the order of about lat%. For metals with a higher oxygen affinity (Fe) about 4 at% oxygen was noticed. Baking of the evaporator walls reduces it to about 10^{-2} at% so that even reactive materials can be prepared in the nanocrystalline form. In all cases the concentration of helium was < 50 ppm.

Most of the metallic impurities result from the pistons of the consolidation unit, from the evaporator material (e.g. the W boat), or is scraped off from the cold-finger surface. Hence the concentration of metallic impurities may be reduced by about one order of magnitude if the small crystals are produced by sputtering (instead of evaporation) and by coating the surfaces of the cold finger and the pistons with the same material as the nanocrystalline substance to be generated.

In nanocrystalline oxides generated by post-oxidation of nanocrystalline metallic powders, non-stoichiometric compositions have been noticed.[137] For example, X-ray diffraction of a TiO_2 sample prepared by oxidizing nanocrystalline Ti powder showed that the stable rutile phase was the only phase present, with no evidence for unreacted Ti or other Ti-oxide phases. The composition of the sample was determine by Rutherford backscattering analysis to be oxygen deficient in the as-prepared state, $TiO_{1.7}$, but after sintering at 300°C, it became nearly stoichiometric, $TiO_{1.95}$. At the same time, the color of the sample changed from black to white, the normal color of bulk rutile. Similarly, nanocrystalline ZrO_2 specimens prepared by post-oxidation of the metal particles obtained by DC-sputtering of Zr in an Ar-atmosphere or by reactive RF-sputtering of Zr in an Ar/O_2 atmosphere had a chemical composition of $ZrO_{2\pm0.2}$. X-ray diffraction experiments indicated the presence of both monoclinic and tetragonal phases in nanocrystalline ZrO_2.[137] The preparation of alloys made up of components with different vapor pressures seems to be possible by means of sputtering and has been successfully tested for $Ti_{48}Al_{52}$ and $Cu_{91}Mn_9$.[137]

3.2. *Density*

The density of metallic nanocrystalline materials varies between 75% and more than 90% of the crystalline density (depending on the material), approaching 100% after grain growth. The initial density of nanocrystalline specimens obtained by consolidation of small particles seems to depend on the specimen thickness and the chemical composition. Nanocrystalline Fe and W (7 nm grain size, about 0.1 mm thickness) exhibit a density of about 70% of a

single crystal. Under similar conditions densities of about 90% or more are achieved for Cu and Pd. Lower densities are noticed for the same material if the specimen thickness increases. In the case of thin specimens, a large fraction of the density deficit seems to result from the reduced atomic density in the boundaries. For example, the density of nanocrystalline specimens of Fe (7 nm) or Pd (10 nm) was observed to increase from about 75% and about 90%, respectively, in the as-compacted state, to nearly 100% after annealing at 700°C and 300°C.[135,138] No open porosity was detected (gas permeation, BET measurements) for as-compacted nanocrystalline fcc metals (Pd, Cu). Metallographic investigations of as-compacted nanocrystalline Cu and Pd revealed between 1 and 8 vol% closed porosity in Cu and practically no pores in Pd for similar consolidation conditions and grain sizes. Nanocrystalline refractory metals (e.g. W) seem to exhibit open porosity in the as-compacted state. The residual porosity may be reduced to virtually zero b extruding the as-consolidated material.

The density of several nanocrystalline Si films deposited by means of chemical transport in a low pressure plasma has been measured.[119] The temperature of deposition was varied between 180°C and 260°C. The measurements were performed on samples which were peeled off the substrates (molybdenum, glass) using the flotation technique in a solution of thallium-formate/malonate with water. A fairly reproducible density of 2.33 g cm^{-3} ± 2% was found for the four samples measured. This value agrees well with the density of crystalline silicon. The density of amorphous hydrogenated silicon with a hydrogen content larger than 10 at% is generally lower.[140]

The density of ceramic nanocrystalline specimens in the as-compacted state seems to be controlled to a large extent by open porosity. A detailed study on this question has been performed by Hahn *et al.*[141,142] for nanocrystalline TiO_2. The density was measured while the samples had open porosity by the nitrogen adsorption method (BET), and by gravimetry otherwise. Simultaneously the grain size was monitored by X-ray diffraction and transmission and/or scanning electron microscopy. Plotted in Fig. 9 are the grain sizes and densities of nanocrystalline TiO_2 as a function of the sintering temperature. The initial density after compaction at 150°C was about 75% of pure bulk rutile (4.25 g/cm^3). This green body density

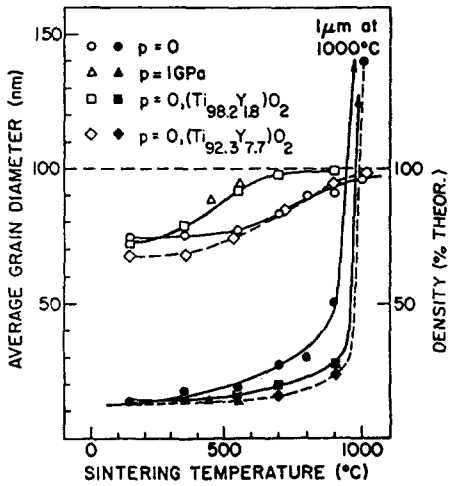

FIG. 9. Density (open symbols) and grain size (closed symbols) of nanocrystalline TiO_2 as a function of sintering temperature; included are data for pressure-assisted sintering and Y-doped nanocrystalline TiO_2. The sintering times in all cases were 15 hr.[142]

is remarkably high in view of the fact that ideal packing of a monodispersed distribution of spheres yields a density of 78%. The high density was attributed to a combination of processing factors. During the initial oxidation of the Ti powder, temperatures rise well over 600°C so that particles in close proximity are able to sinter and form dense agglomerates. The compacted powder is thus comprised of a bimodal distribution of dense agglomerates and small particles for which high densities are easier to achieve. Densification during the consolidation process was thus suggested to occur by a combination of grain boundary sliding and fracture of agglomerates as the green body density is found to be a strong function of compaction pressure. Little densification was found to occur during pressureless sintering at temperatures below $\approx$550°C (Fig. 9). Above 600°C, however, the density increased with temperature, reaching a value of 96–99% bulk density at 900°C. These sintering temperatures are far lower than those required for standard titania powders. For example, it was observed that densification of TiO_2 with an initial particle size of 1.3 μm required temperatures in excess of 1,100°C for complete densification.[142] The reduced sintering temperature in nanocrystalline TiO_2 is readily explained by the small crystal size.[143] While densification begins at 600°C, Fig. 9 illustrates that the grain size remains stable until the sintering at temperatures of 1,000°C or more. Although various microstructural features can suppress grain growth, pore drag was suspected to be the stabilizing force below 800°C. To increase the driving force for densification but not for grain growth, nanocrystalline TiO_2 was sintered by hot isostatic pressing using about 1GPa at 450 and 550°C. As may be seen from Fig. 9, the densification is significantly enhanced by this procedure, attaining densities in excess of 95% at 550°C, while grain growth is suppressed. Doping treatments can also influence grain growth as indicated in Fig. 9 for additions of 1.8 and 7.7 at% Y to TiO_2. In both cases, grain growth is notably reduced while densification is enhanced.

Comparative positron annihilation studies of the densification process of nanocrystalline and conventional ceramics during annealing lead to a similar picture.[144] The simple two-state positron annihilation behavior observed in TiO_2 samples with grain sizes of 12 nm and 13 μm (both consolidated at 1.4 GPa) indicates that both materials began to densify rapidly above 500°C. However, the nanocrystalline material did so more rapidly with increasing temperature than the coarser-grained sample, resulting in a smaller void or pore density at 900°C. The intensity I_2 (Fig. 10) of the lifetime signal corresponding to positron annihilation from void-trapped states decreases more rapidly with temperature in the nanocrystalline sample than in the coarser-grained one, indicating a more rapid decrease of void density. The positron lifetime measurements, which are sensitive to varying pore sizes when they are small, also indicate smaller pore or void sizes in the nanocrystalline sample relative to the coarser-grained material through the smaller values of the void-trapped positron lifetime τ_2 at all the sintering temperatures investigated (Fig. 10).

3.3. *Microstructure*

3.3.1. *Nanocrystalline metals*

The microstructure of nanocrystalline metals was investigated by transmission and scanning electron microscopy, tunneling microscopy, small angle X-ray and neutron diffraction and X-ray texture analysis.

3.3.1.1. *Electron microscopy.* Studies by conventional and high resolution transmission electron microscopy (TEM) indicate that nanocrystalline metals consist of small crystallites of different crystallographic orientations separated by grain boundaries (Fig. 11). The distribution of grain sizes measured by TEM is shown in Fig. 12 and seems to agree roughly

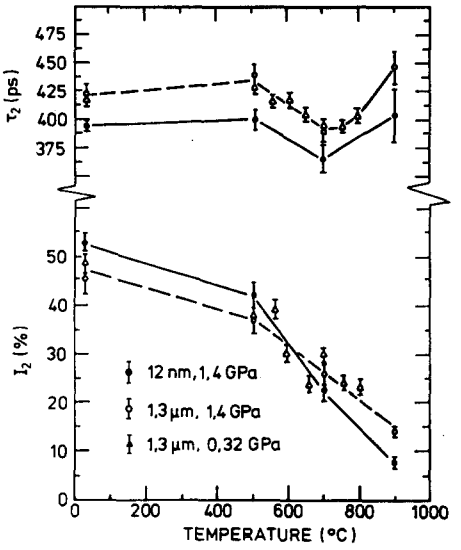

FIG. 10. Results of a two-component lifetime fit to positron annihilation lifetime data from the 12 nm, 1.4 GPa nanocrystalline samples (filled circles) are compared to those from 1.3 μm, 1.4 GPa (open circles) and 1.3 μm, 0.32 GPa (triangles) samples compacted from commercial powder as a function of sintering temperature. The positron annihilation data were measured at room temperature; no sintering aids were used.[144]

with the results obtained by small angle X-ray or neutron scattering (Fig. 13). In as-prepared specimens of Pd, Cu and Fe the micrographs gave little evidence for a large volume fraction of macroscopic pores.[145] A study[146] of the atomistic structure of the grain boundaries by high resolution TEM suggested a similar boundary structure and width as in conventional polycrystals. However, these results may have to be considered with care. The preparation of thin specimens (the specimen thickness for high resolution TEM has to be less than the

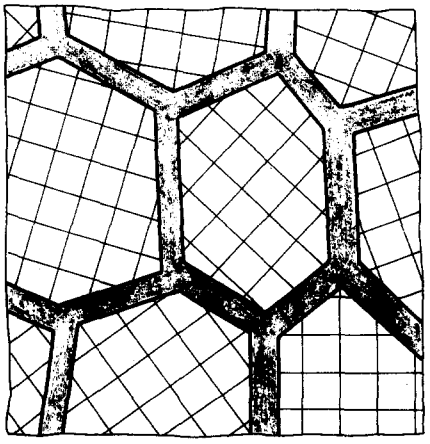

FIG. 11. Microstructure of a nanocrysalline material deduced from the methods mentioned in Section 3.3. The cross-hatched areas represent the crystals of different crystallographic orientations. The grey regions separating the crystals are the grain boundaries.

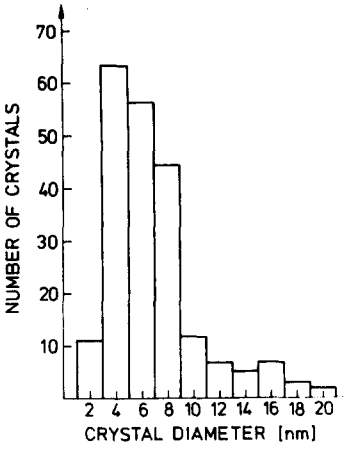

FIG. 12. Crystal size distribution in nanocrystalline Fe measured by transmission electron microscopy.[138]

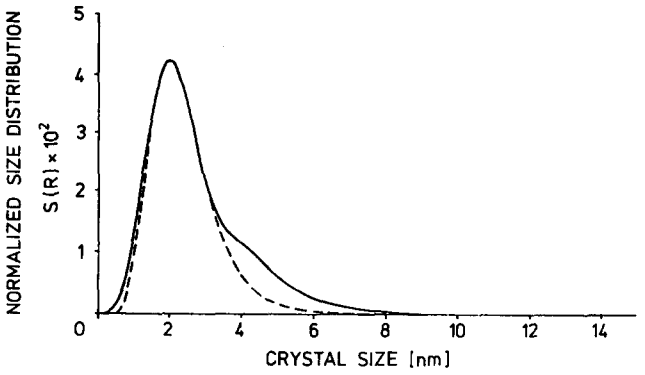

FIG. 13. Normalized size distribution of nanocrystalline Pd obtained from the small angle neutron scattering measurements by fitting the experimental data (Fig. 14) by means of the procedure discussed in Refs 147 and 148. The broken line represents the log-normal distribution.[147,148]

crystal diameter) transforms the three-dimensional crystal arrangement of a bulk nanocrystalline specimen into a two-dimensional arrangement. This process may change the boundary structure as it alters the forces between neighboring crystals and induces new forces due to the energy of the free surface of the thin specimen. Furthermore, due to the high diffusivity in nanocrystalline materials (cf. Sections 4.2 and 4.3) atoms may diffuse from the free surface of a thin specimen into the grain boundaries at ambient temperatures within a time much shorter than the time of specimen preparation. This process may alter the boundary structure as well.

3.3.1.2. *Small angle X-ray and neutron diffraction.* In order to characterize the microstructure of nanocrystalline Pd (grain size distribution, average atomic density in the grain boundaries), studies by means of small angle X-ray and neutron scattering had been performed.[147,148] Small angle scattering is diffuse scattering at small values of the scattering vector $\mathbf{q}(|\mathbf{q}| = q = 4\pi \sin\theta/\lambda)$. It is caused by correlations in the arrangement of scattering centers extending over distances larger than the interatomic spacing. If scattering from a particle of average scattering length density ρ_p embedded in a matrix of average scattering length density ρ_m is considered, the scattering cross-section (SCS) is given by:

$$\frac{d\sigma}{d\Omega}(\mathbf{q}) = \left| \Delta\rho \int_{-\infty}^{+\infty} F(\mathbf{r})\, e^{i\mathbf{q}\mathbf{r}}\, d\mathbf{r} \right|^2$$

where $\Delta\rho$ is $(\rho_m - \rho_p)$, and $F(\mathbf{r})$ is the form function of the particle: $F(\mathbf{r}) = 1$ inside, $F(\mathbf{r}) = 0$ outside the particle.

If N particles are distributed in the sample in an uncorrelated way, the SCS is enhanced by a factor N. If correlations in the arrangement of different particles are important, the SCS is changed in a way characteristic of the specific correlation. Following Porod[149] one may qualitatively distinguish two types of correlation: "liquid"-type correlations causing a decrease of the SCS at small q. This kind of correlation arises, for example, from dense packing of spherical particles. "Gas"-type correlation causes an increase of the SCS at small q and may arise from dense packing of non-spherical particles that touch one another in many places.

Figure 14 shows the SCS of neutrons for a nanocrystalline Pd sample. The solid line was computed from the size distribution $S(R)$ shown in Fig. 13 of scattering units obtained from

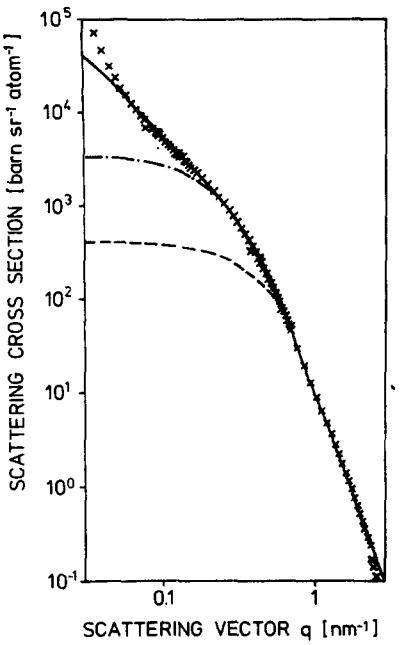

FIG. 14. Small angle neutron scattering cross section of nanocrystalline Pd. The solid line corresponds to the calculated scattering cross section obtained from the size distribution of Fig. 13 in the entire R range admitted ($R_{max} = 200$ nm). The dash-dotted line corresponds to the size distribution of Fig. 13, truncated at $R = 15$ nm; the broken line gives the log-normal distribution approximated to the section of the size distribution shown in Fig. 13 at small crystal sizes.[147]

experimental data by the method given by Glatter.[150] The size distribution shown in Fig. 13 may be divided into two regions: the region of small radii ($R \leqslant 15$ nm)—containing the asymmetric peak at 2 nm—reflects the size distribution of Pd crystallites. The contribution at $R > 15$ nm is due to correlations in the arrangement of the crystallites.

The crystallite size distribution centered at $R \approx 2$ nm is similar to the log-norm distribution found for isolated crystallites.[31] The measured size distribution agrees reasonably well with direct measurements by transmission electron microscopy.[138] The measured size distribution dominates the behavior of the SCS at large q. In this range the SCS calculated from the size distribution of Fig. 13, truncated at 15 nm, coincides with the experimental curve (compare the dash-dotted line in Fig. 14). At small q-values the SCS is enhanced above the one expected for the crystallites due to special correlations between the crystals. Evidently this correlation is of "gas"-type. In other words, the crystallites are not spherical and may touch in many places. At the smallest q-values contributions from very large scattering units, possibly voids of some μm size are observed. Additional information about the microstructure may be obtained from the evaluation of the SCS in absolute units. For this purpose the nanocrystalline material was assumed to consist (Fig. 11) of crystallites with an average density ξ_c (equal to the density of single crystalline Pd). A volume fraction, v_c, of the total volume of the material is filled with crystallites. The boundaries occupy a fraction of $1 - v_c$. The crystallites are assumed to be embedded in a uniform matrix of grain boundaries with a uniform density. On the basis of this model, the boundary density may be computed from the measured SCS in absolute units and the macroscopic sample density. The measurements performed[147] yield a boundary density of about 60% of the lattice density. This is a

remarkably low density for a solid state structure. In fact it is much lower than the density of glasses which usually deviate by a few percent from the crystalline density. On the other hand, such a reduced density in the interfacial regions seems consistent with the densities of computed grain boundary structures[15] as well as with the reduced density observed in the core of grain boundaries[201] and dislocations.[153] In fact, it has been pointed out in the first section that the small size of the crystallites in nanocrystalline materials is likely to result in a reduced boundary density due to the very limited rigid body relaxation.

Clearly, the measured boundary density is correct only if assumption applies that the SCS due to the residual porosity of a nanocrystalline sample is negligible in comparison to the scattering originating from the density difference between crystals and the surrounding grain boundaries. The similarity of the grain size distribution by means of TEM (Figs 12 and 15) and SCS (Figs 13 and 16) seems to support this assumption. Measurements of the residual porosity by means of conventional metallography using scanning electron microscopy (Section 3.2) suggest a maximum error of 30% for the measured boundary density in nanocrystalline Pd. In other words, the average boundary density in nanocrystalline Pd seems to be between about 60% and 70% of the crystal density. An interfacial density of about 60% to 70% of the lattice density would indicate a rather "open" atomic structure with a much broader distribution of interatomic spacings than in a liquid or glass, the density of which differs from the crystalline density by a few percent. The low interfacial density agrees with the enhanced hydrogen solubility, specific heat, diffusivity, the reduced elastic constants of nanocrystalline specimens as well as with the arguments put forward in Section 1. It is presently not known how the free volume is distributed between the grain boundaries and the triple junctions formed at the intersection between three boundaries.

Measurements of the [111] and [200] pole figures of as-prepared nanocrystalline Pd and Cu revealed no prefered orientation of the crystallites. Hence isostatically consolidated nanocrystalline materials seem to be free of any strong texture.

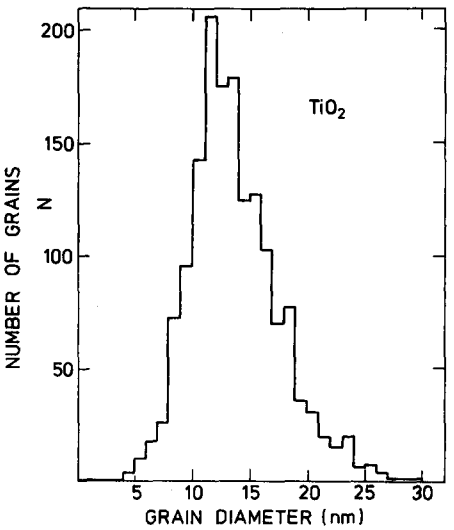

FIG. 15. Grain-size distribution for an as-compacted TiO_2 (rutile) sample determined using TEM.[154]

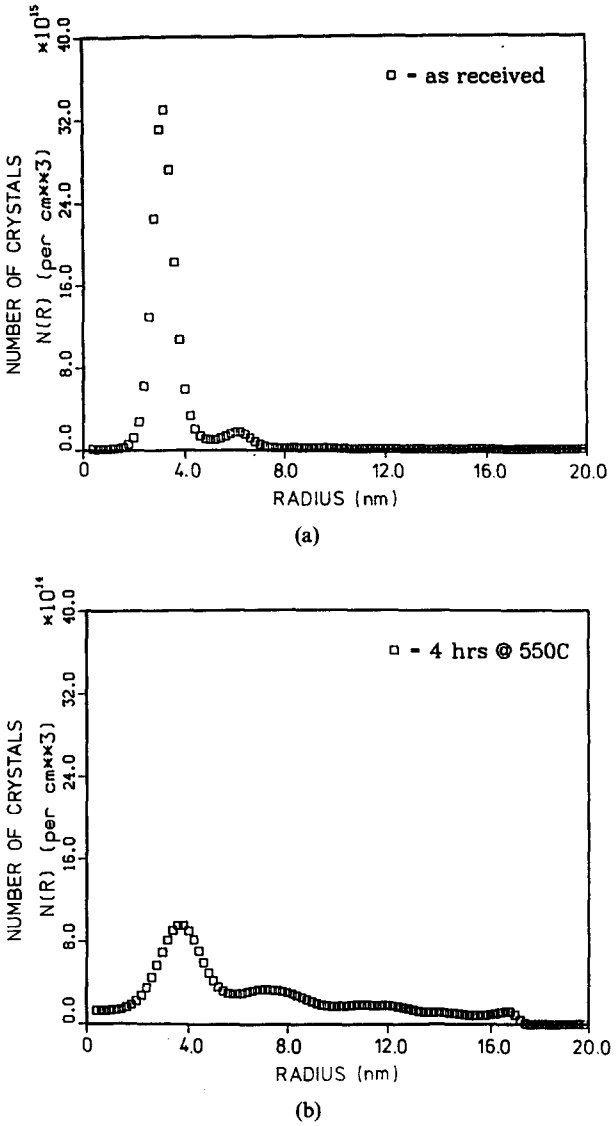

FIG. 16. Size distributions determined by the maximum entropy method for: (a) the as-compacted nanocrystalline TiO_2 sample and (b) the same sample after isothermal sintering for 4 hr at 550°C.[155]

3.3.2. *Nanocrystalline ceramics*

3.3.2.1. *Grain size distribution and boundary density.* The grain size distribution and boundary density of nanocrystalline ceramics has been studied so far for TiO_2 most extensively. Figures 15 and 16 show the grain size distribution measured by scanning transmission electron microscopy[141,154] and small angle neutron scattering.[147,148,155]

Figure 17 shows a scanning electron micrograph of the fracture surface of as-compacted and annealed nanocrystalline TiO_2.[141] The individual grains of the as-prepared sample (Fig. 17a) have an average size of 30 nm. As this is about twice the size measured by transmission electron microscopy and X-ray diffraction, most of the particles visible

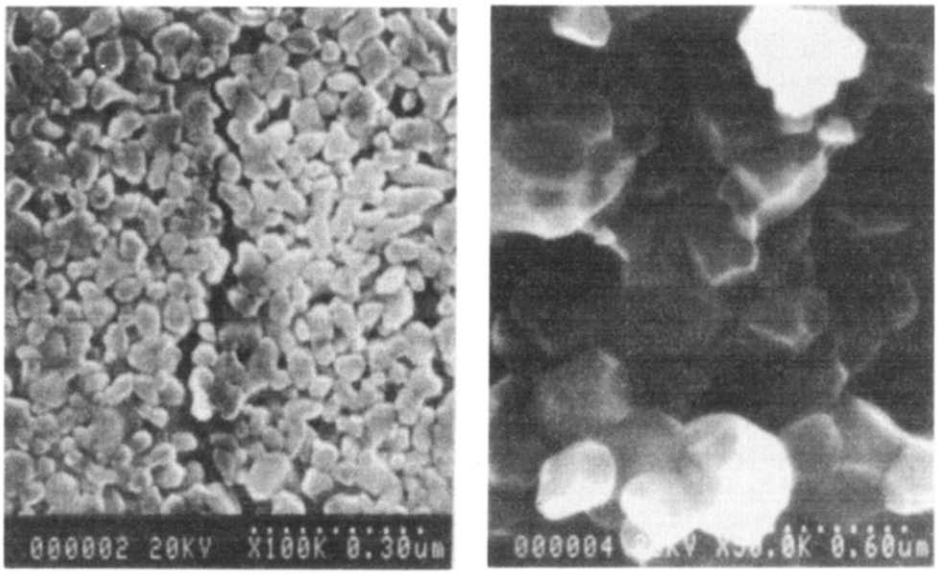

(a) (b)

FIG. 17. High resolution scanning electron micrographs of nanocrystalline TiO_2. Left side (a): as prepared; right side (b): annealed for 14 hr at 1,173 K in an oxygen atmosphere.[141]

in Fig. 17 are suspected to consist of several crystals. After sintering at 1,173 K for 14 hr a much denser structure than in Fig. 17a with more facetted grains was observed. No porosity was detected after annealing. In fact, the density was more than 90% of the crystalline value.

Small angle neutron scattering studies have been performed in the as-consolidated condition and after isothermal sintering anneals up to 23 hr at 550°C.[155] The data obtained was analyzed by the maximum entropy method. This method devises a way to estimate the power spectrum of a given real function by mapping it onto the unit circle of the complex z-plane. The power spectrum of the given function is then completed by fitting the function in the z-plane by a suitable polynomial of the form of a finite Laurent series. For the as-consolidated material a boundary density of about 60% to 70% of the crystal density was found, assuming the crystals to be ideal. The average boundary width was about 0.5 nm.

3.4. *Effect of Consolidation Pressure on Microstructure*

The effect of the consolidation pressure on the structure of nanocrystalline metals was studied by means of Mössbauer spectroscopy and positron annihilation for Fe (7 nm crystal size) and Ni (70 nm crystal size), respectively. The Mössbauer spectra (Fig. 18) observed[156] suggest the formation of a growing volume fraction of grain boundaries with increasing pressure approaching a constant value beyond about 3 GPa. Studies by electron microscopy support this result. Increasing pressure reduces the pore density and replaces free surfaces (e.g. pore surfaces) by grain boundaries.

Figure 19 summarizes the positron lifetime and the lattice constant of the nanocrystalline Ni as a function of consolidation pressure. In fact, the positron lifetime spectrum[157,158] consisted of a short and a long component. The short one corresponded to single vacancies whereas the long one indicates clusters of about 8 vacancies (cf. Section 3.7.1). The vacancies

and vacancy clusters, the concentration of which is found to be about 10^{-4}, are proposed to originate from the migration of grain boundary dislocations during consolidation. The high vacancy concentration may enhance the diffusivity in these materials and thus result in rapid densification.

3.5. *Thermal Stability*

3.5.1. *Nanocrystalline metals*

The thermal stability of nanocrystalline metals was studied by transmission electron microscopy, Mössbauer spectroscopy, small and wide angle X-ray diffraction and positron annihilation. Nanocrystalline metals exhibit crystal growth at elevated temperatures. Roughly speaking, in metals with a crystal size of about 10 nm, significant crystal growth (doubling of the crystal size in about 24 hr) was noticed at ambient temperature or below if the equilibrium melting temperature, T_m, was lower than about 600°C (e.g. in nanocrystalline tin or lead). However, if T_m was higher, the stability against grain growth seems to be enhanced; for example, for Fe to $\leqslant$200°C, for Pd to $\leqslant$150°C and for Cu to $\leqslant$100°C. An example[138] is shown in Fig. 20. The same picture emerges from studies by means of Mössbauer spectroscopy and X-ray diffraction.

Figure 21 shows a comparison of the Mössbauer spectra of the same specimen before and after annealing at 500°C in vacuum.[138] The second spectrum (Fig. 21b) coincides with the one of conventional Fe whereas the first one consists of a component which corresponds to the α-Fe spectrum and a broad component due to the grain boundaries (cf. Section 3.7.3). No change of the Mössbauer spectrum was noticed if the same specimen was annealed in vacuum for 10 hr at 100°C. In order to avoid oxidation effects all specimens were never exposed to air before and after annealing.[138]

X-ray diffraction studies (cf. Section 3.6.1) of nanocrystalline Fe with an initial grain size of 6 nm indicate the following effects. Annealing (1 hr at 500°C) reduces the peak width and the background intensity to the values characteristic for a conventional polycrystal[156] suggesting that the majority of the grains have grown to a size beyond about 30 nm. A systematic study of the annealing behavior of nanocrystalline Pd by means of positron annihilation (cf. Section 3.7.1) was performed by Schaefer *et al.*[159] and led to the following results. In as-prepared specimens, the spectra suggest predominantly two lifetimes, $\tau_1 = 183 \pm$ ps and $\tau_2 = 391 \pm 2$ ps. These two lifetimes were interpreted in terms of positron annihilation at sites in the boundaries associated with a free volume of about one vacancy and spherical clusters of about eight vacancies. This result seems consistent with the expected "open structure" of the boundaries (Figs 4, 5 and 6) and the remarkably low density in the boundaries (Sections 3.3.1 and 3.3.2).

In the positron lifetime measurements after isochronal annealing, the following four temperature regimes were noticed (cf. Fig. 22).

(I) 20°C–350°C: The increase of mean positron lifetime was attributed to a re-ordering and growth of interfacial free volumes. The numerical analysis of the spectra shows that the lifetime increase (Fig. 22) is initially due to an increase of ratio I_2/I_1 of the two lifetimes observed in these materials at 150°C without significant changes of τ_1 or τ_2 (Fig. 23). This indicates a relative increase of the number of sites with larger free volume at the expense of vacancy-sized free volumes in the boundaries. The concentration decrease of vacancy-sized free volumes is unlikely to occur in the crystallites because high-temperature studies of bulk Pd crystals indicate that monovacancies are frozen-in below 120°C.[160] The increase of τ_1 and τ_2 above 180°C is attributed to an agglomeration of vacancy-sized free volumes and vacancy

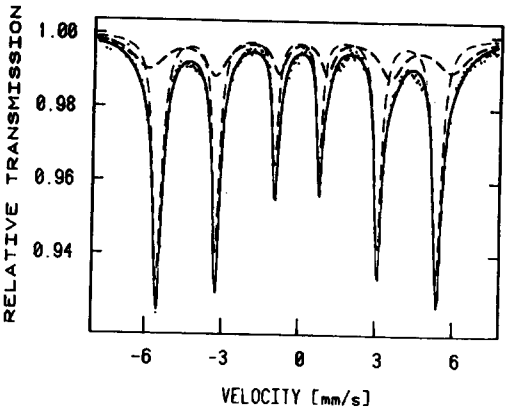

PRESSURE 27.5 MPa T = 77 K

(a)

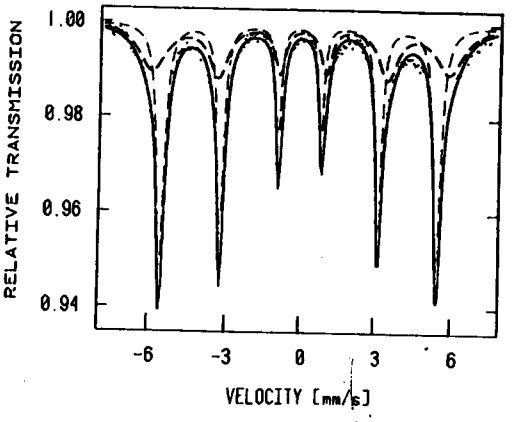

PRESSURE 30 MPa T = 77 K

(b)

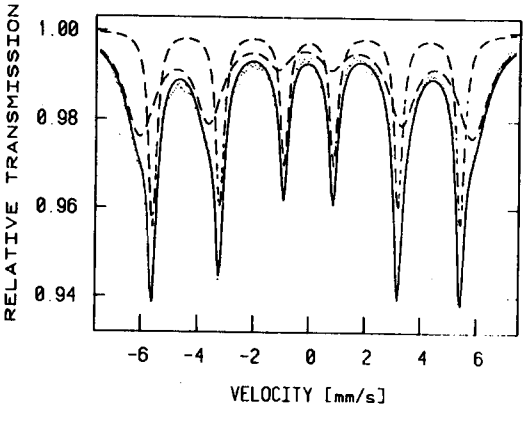

PRESSURE 32.5 MPa T = 77 K

(c)

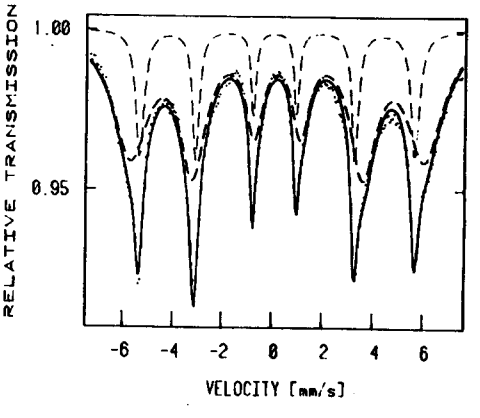

PRESSURE 75 MPa T = 77 K

(d)

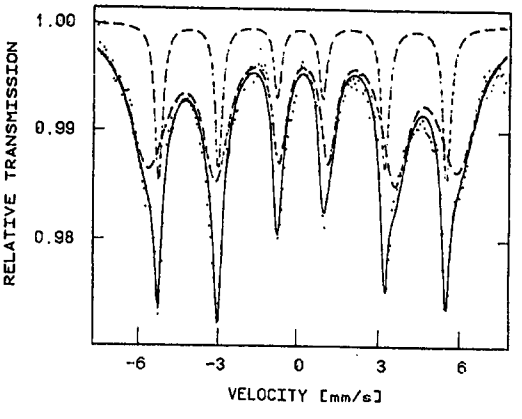

PRESSURE 85 MPa T = 77 K

(e)

FIG. 18(a–e)

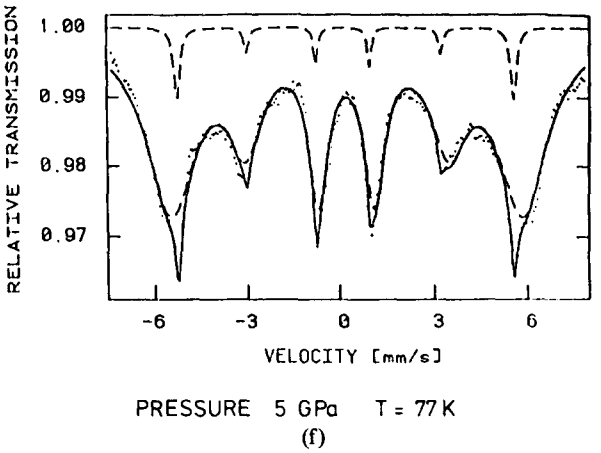

FIG. 18. Mössbauer spectra of nanocrystalline Fe as a function of consolidation pressure. The narrow six-line component results from Fe atoms situated in the α-Fe crystal lattice. The residual broad component is due to the grain boundaries.[156]

aggregates. The phenomena observed in this temperature range are proposed to occur in the boundaries without any displacement of these interfaces by crystal growth which appears to be negligible.[161]

Irreversible re-ordering phenomena in the interfaces apparently occur even below the annealing temperatures where changes in $\bar{\tau}$ are observed.

(II) 350°C–500°C: The decrease of $\bar{\tau}$ in Fig. 22 arises from a decreasing ratio I_2/I_1. This change was interpreted in terms of the annealing-out of vacancy aggregates.

(III) 500°C–900°C: mean positron lifetime $\bar{\tau}$ remains unaltered although substantial crystallite growth is observed.[161] This observation may be understood in terms of the positron diffusion length $L^+ \approx 100$ nm[162] in the crystallites. L^+ still by far exceeds the crystallite diameter d and therefore the positrons can arrive quantitatively at the interfacial traps, the atomic structure of which appears to be unchanged during crystal growth according to the observed unaltered lifetimes τ_1 and τ_2.

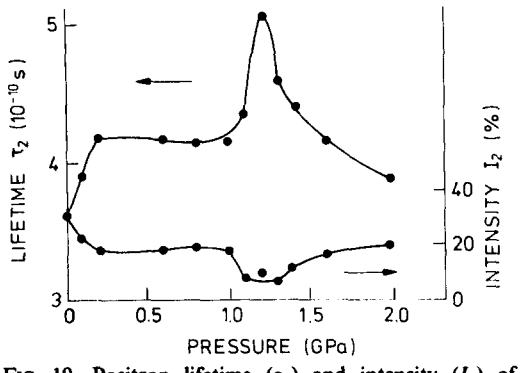

FIG. 19. Positron lifetime (τ_2) and intensity (I_2) of nanocrystalline Ni as a function of the consolidation pressure.[157]

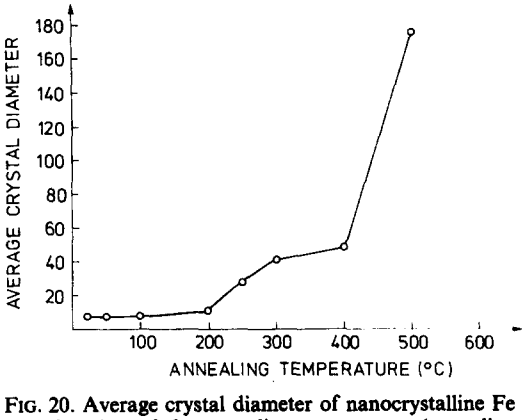

FIG. 20. Average crystal diameter of nanocrystalline Fe as a function of the annealing temperature (annealing time was 10 hr at any one of the temperatures given in this figure).[138]

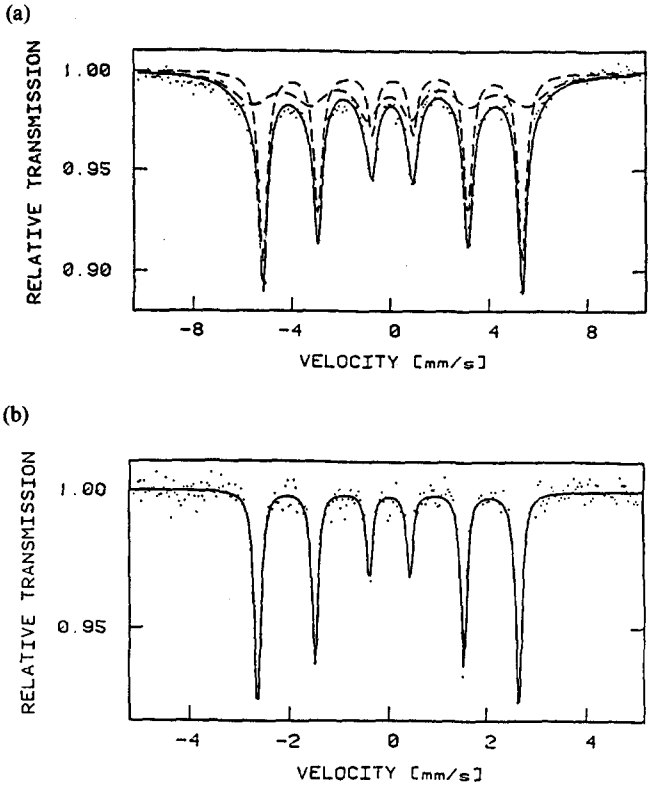

FIG. 21. Comparison of the Mössbauer spectra of the same nanocrystalline Fe specimen before (a) and after (b) annealing (10 hr at 500°C).[156]

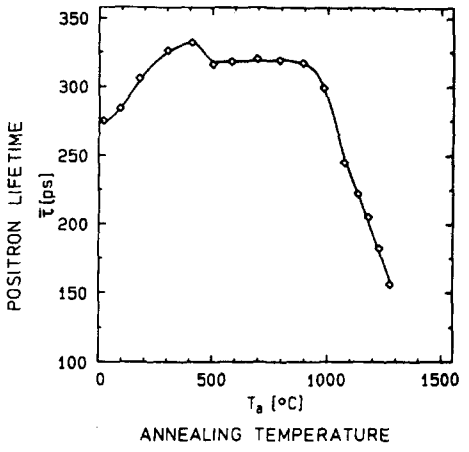

FIG. 22. Variation of the mean positron lifetime after isochronal annealing ($t_a = 30$ min) of nanocrystalline Pd in high vacuum.[159]

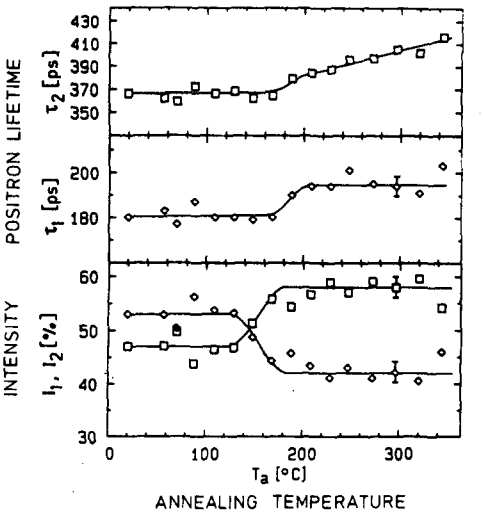

FIG. 23. Positron lifetimes τ_1 and τ_2 as well as the corresponding relative intensities I_1 (◇◇) and I_2 (□□) after isochronal annealing ($t_a = 60$ min) nanocrystalline Pd in high vacuum.[159]

(IV) Annealing above 900°C: Above 900°C the mean lifetime $\bar{\tau}$ decreases because $d > L^+$ so that a measurable fraction of positrons is annihilated in the free delocalized state in undisturbed larger crystallites. From the mean positron lifetime longer than τ_f, positron lifetime in the free "delocalized" state, at $T_a = 1{,}280$°C one is led to conclude, that even at these high annealing temperatures a measurable number of interfaces with positron traps is present in the specimens. In fact, it appears that the nanocrystalline structure is partly stable up to annealing temperatures close to the melting point. This is confirmed by transmission electron microscopy (TEM) studies after prolonged (several hours) annealing at 1,280°C[163] showing nanocrystalline regions with crystallite sizes smaller than 100 nm coexisting with large recrystallized grains.

Similar results were obtained from small angle X-ray scattering experiments[147,148] performed during annealing of nanocrystalline Pd samples (initial grain size 8 nm, annealing time 1,800 s at 520 K and 1,023 K, respectively). The results of these measurements are compared in Fig. 24 with the data of the as-prepared specimen (300 K). Two regions may be discerned, which behave differently on recovery: at large q-values the functional dependence of the scattering cross section on the diffraction vector (**q**) remains nearly unchanged, but the scattered intensity decreases by about a factor of 2 at 1,023 K. At small values of q, the decrease of the scattering cross section with q gets steeper after annealing, so that the intensity remains nearly unchanged at the smallest q-values measured. These observations are compatible with the transformation of a part of the crystallites either into some large crystals, or into a system of crystallites with high "gas"-type correlation. A fraction of the crystallites remains rather unaffected by the annealing up to 1,000 K, and causes the unchanged scattering signal at large q. One reason for the apparent stability of some regions of a nanocrystalline material may be the high excess entropy (cf. Sections 4.4 and 4.5).

Gryaznov *et al.*[164] studied the processes occurring during annealing of nanocrystalline Cu and Ni specimens (grain size 50 to 70 nm) by measuring the shrinkage of porous specimens. The high rates of shrinkage observed during the initial stage of sintering were interpreted in terms of a diffusional motion of individual crystallites as well as by a boundary energy induced rotation. These processes were suggested because the shrinkage rate observed exceeded the one expected on the basis of volume and boundary diffusivity by about three orders of magnitude. In view of the high diffusivities measured in nanocrystalline samples (cf. Sections 4.1 and 4.2), the high shrinkage rates observed appear to be consistent with a conventional sintering model as well. Similar studies[165–167] were performed by other authors utilizing positron lifetime spectroscopy to characterize the defects involved in

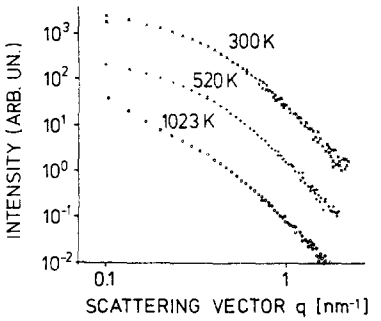

FIG. 24. Small angle scattering cross section of X-rays for nanocrystalline Pd, annealed at the temperatures indicated.[147]

sintering and grain growth of nanocrystalline Ni and Cu. In the initial state of sintering and grain growth, a high concentration (about 10^{-4}) of excess vacancies was observed. These vacancies are proposed to originate from boundary migration. Evidently, a high concentration of vacancies may enhance the rate of sintering by many orders of magnitude, as was observed. A conceivable application of this effect was proposed in terms of the the sintering of materials with high melting points[168,169] such as W, Mo, etc. If such materials are mixed with a nanocrystalline substance with the same or with different chemical composition, e.g. W, Mo, Ni, etc., grain or interphase boundaries between the nanocrystalline and the coarse-grained material are formed. These interfaces act as efficient vacancy sources and thus enhance the diffusivity and the sintering rate. This idea was tested for two systems: W, Mo (1–10 μm) with additives of nanocrystalline Ni (70 nm) and c (7 nm), and W, Mo (1–5 μm) with additives of nanocrystalline W (39 nm) and Mo (50 nm). In both cases the sintering temperatures were found to be reduced, e.g. for W with nanocrystalline W by 400°C. The same applies for the formation of carbides if nanocrystalline C has been added.

A variation of the type of chemical bonding was found to affect the growth rate significantly. For example, silicon and germanium exhibited grain growth at ambient temperature whereas antimony was stable up to 400°C. Just as in conventional polycrystals, grain growth in nanocrystalline materials may be inhibited by second-phase particles and/or impurity drag. The stability of multiphase nanocrystalline materials depends on the mutual solubility of the phases involved. If all phases are mutually insoluble and if the concentration of each phase is below the percolation limit, the system cannot exhibit grain despite the energy stored in the interfaces.

An effect of this type has been noticed in the Al/AlN system. Cryomilling (mechanical alloying in liquid nitrogen) led to a matrix of Al with a fine grain size (< 50 nm) with dispersed AlN particles.[170] This microstructure proved to be very resistant against coarsening, even at temperatures approaching the melting point of Al.

Similar grain growth effects have been noticed in nanocrystalline ceramics.[141–143,171] So far most of the studies on nanocrystalline ceramics have been limited to TiO_2 (Fig. 9). Up to about 600°C the grain size remains unchanged. Rapid growth takes place at 800°C or more. Hot isostatic pressing increases the driving force for densification and reduces grain boundary mobility. Hence, a pressure/temperature window exists at which dense, nanocrystalline ceramics may be obtained. Doping may also influence grain growth as illustrated in Fig. 9 for various additions of Y to TiO_2. Positron studies of the grain growth process[144] (Fig. 10) indicate that the intensity of the lifetime signal corresponding to void-trapped states decreases more rapidly with temperature in nanocrystalline samples than in coarser-grained materials. This result suggests a more rapid decrease of void density. The same picture emerges from the BET measurements by Hahn *et al.*[172] Annealing at elevated temperatures was noticed to remove the smallest pores first. This behavior may be rationalized in terms of the high free energy of these pores resulting in Ostwald ripening of the pores.

3.6. *Atomistic Structure*

The atomistic structure of nanocrystalline materials was studied by X-ray diffraction and EXAFS experiments. Structural investigations by means of high resolution transmission electron microscopy suffer from the difficulty that atomic rearrangements may occur during specimen preparation. The preparation of sufficiently thin foils (thickness less than one grain diameter, i.e. less than a few nanometers) transforms the three-dimensional crystal

arrangement of the real material into a two-dimensional one and thus may permit the atoms in the boundaries to rearrange by diffusional processes during specimen preparation.

3.6.1. *X-ray diffraction studies*

The purpose of the X-ray diffraction studies[2] was to obtain information about the structure of the interfacial component by comparing the interference function deduced from the X-ray diffraction experiments with the one calculated from different structural models of nanocrystalline materials. The simplification made in this computation is to assume that the nanocrystalline material consists of crystals (with a perfect crystal structure, Fig. 25) and grain boundary core regions where the atoms may have relaxed away from ideal lattice sites. All crystals together form the "crystalline component" of the material. The atoms in the boundary cores constitute the "boundary component". Hence the boundary component is actually the sum over numerous (about 10^{19} per cm^3) boundaries with different atomic structures according to the ideas discussed in the first section. Due to the small size of the crystallites of a nanocrystalline material, the numbers of atoms located in the crystalline component and in the interfacial component are comparable. Hence, the computation of the X-ray scattering of a nanocrystalline material requires the computation of the scattering due to the differently oriented crystals as well as the computation of the scattering originating from the interfacial regions. The existence of X-ray scattering from interfacial regions and its usefulness to obtain information about the atomic structure of interfaces has been demonstrated by Sass *et al.*[173] It has been shown[175] that the scattering of the differently oriented crystals of a polycrystalline material with a random texture may be computed by means of the following procedure. A single crystal the size of which is equal to the average crystal size of the polycrystalline material is considered. This crystal represents the ensemble average of the individual crystallites of the polycrystal. For the crystal the interference function I(**s**) for a specific orientation characterized by a diffraction vector **s** of the crystal with respect to the incident X-ray beam is computed. This procedure was repeated for all possible orientations of the crystal and the different resulting interference functions I(**s**) were averaged for $s = \text{const}$. If the averaging procedure is repeated for all possible values of s, the

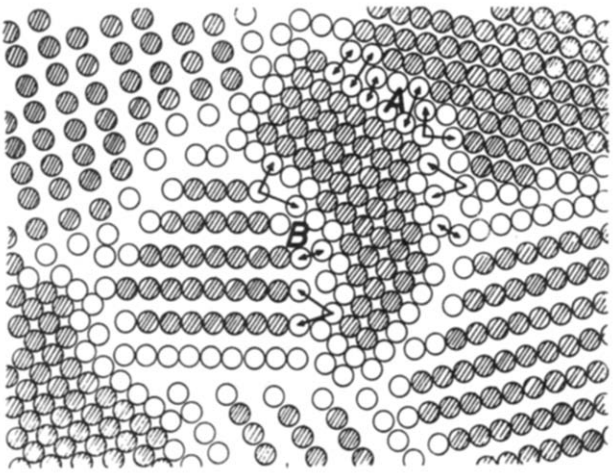

FIG. 25. Schematic cross section through a nanocrystalline material illustrating the approach used in Ref. 173. The arrows indicate the interatomic spacings in the boundary core region. For further details we refer to Section 3.6.1.

resulting function $I(s)$ is[175] the interference function of the polycrystal with a random texture. By following the same procedure, the scattering from the crystalline and interfacial components of nanocrystalline material was computed.[2] In fact, for the specific case of the nanocrystalline Fe, the crystalline component was modeled by a cube-shaped α-Fe-(bcc) crystal representing the ensemble average of the crystalline component. The volume of this cube was matched to the average volume of the crystallites of the nanocrystalline Fe. The ensemble average of the interfacial component was simulated by an assemblage of atoms whose structure was varied between the two conceivable extremes: an ordered structure and a structure without any order. A variation of the ensemble average between order and disorder covers all conceivable boundary structures. This approach was used as the exact structure of the ensemble average over all boundary cores is not known. The interfacial component consisted of an assemblage of atoms arranged in the form of two layers of atoms with α-Fe structure attached coherently at the outer surface of the cube. Subsequently, the atoms in the three outer layers were displaced by non-lattice vectors into randomly chosen directions. These displacements do not imply that the atoms in any particular grain boundary of a nanocrystalline material are displaced in random directions from their original lattice sites.[146] In fact, the displacements are used to model the average over the interatomic spacings between the atoms in the "surface region" of one crystal relative to the atoms in the opposite "crystal surface region", i.e. the interatomic spacings indicated by the arrows in the boundaries A and B (Fig. 25). As was pointed out in the first section (Figs 4 and 5), the misfit and the atomic displacements in the boundary cores result in a reduced density and a broad distribution of interatomic spacings. Both features are modeled by the random atomic displacements of the atoms in the "surface regions" of both crystals. In other words, the two outer layers are supposed to model the "surface layer" of atoms of one crystal (e.g. crystal A, Fig. 25) and the "surface layer" of atoms of the adjacent crystal (e.g. crystal B, Fig. 25). As both crystals have different crystallographic orientations, a variety of interatomic spacings (arrows in Fig. 25) exist between the atoms of both layers. In the core of a real grain boundary the assumed variety of interatomic spacings exist as may be seen from Figs 4 and 5 in Section 1. The different interatomic spacings are formed because in the boundary region two differently oriented crystal lattices are joined together. A variation of the number of layers was used to simulate boundaries of different widths. The effects of crystallite size and crystallite size distributions were accounted for by adjusting the size of the cube to the measured values of the average crystallite size obtained by X-ray diffraction and electron microscopy. By varying the magnitude of the random atomic displacement in the second and third outer layer of the cube, the elastic displacements of the atoms in the crystal lattices close to the boundary were simulated. The lower density of the grain boundary core region relative to the density of the crystallites (cf. Sections 3.3.1 and 3.3.2) was taken into account by uniformly lowering the average atomic density in the "surface layers" representing the boundary cores. The thermal diffuse scattering of the crystalline component at room temperature was simulated by randomly displacing the crystal atoms by 3% of the nearest neighbor distance which corresponds to the attenuation of the diffraction peaks of α-Fe at room temperature. The effect of interparticle interference is not included in the computed interference function $I(s)$. Interparticle interference has been shown to yield only non-vanishing scattering in the small-angle region[176] which was not within the scope of the study. The interference function of the crystalline and the interfacial component was computed in the classical way, by summing-up the contribution of the scattering amplitudes of all atoms with the correct phase factor. The computed three-dimensional function was reduced to a one-dimensional plot by averaging over many diffraction vectors. All computed interference

functions were convoluted by a Gaussian instrument function in order to simulate the effect of instrumental broadening of the diffractometer used for the experiments.

A comparison of the experimental and the computed interference functions is shown in Fig. 26 assuming a short-range-ordered grain boundary structure. Neither the peak width, peak height or the background intensity is reproduced correctly. The boundaries were assumed to have a thickness of four atomic layers, which agrees with the present knowledge of the atomic structure of grain boundaries in metal (see for example Ref. 177). In a second set of computations, an attempt was made to match the experimental data by assuming a grain boundary component with the following structure (Fig. 27). The average over the interatomic spacings between the atoms at the "surface" of one crystal and the "surface atoms" of the second crystal (arrows in Fig. 25) were assumed to be random. Therefore, the atoms of the outer layer were displaced by 50% of the nearest neighbor distance from their lattice sites in random directions. The resulting wide variety of interatomic spacings are assumed to represent the interatomic spacings in the boundary core region due to the lattice misfit and due to the atomic relaxations (Figs 4 and 5). In order to model the strain at and near the boundary core the atoms of the second and third outermost layers were displaced by 25% of the nearest neighbor distance from their lattice sites in random directions. It may be seen from Fig. 27 that the computed I (s) curve reproduces not only the heights and widths of all the peaks, but also matches approximately the background intensity, especially in the regime between $s = 0.1$ and 0.45 where the fit with the model assuming a short-range-ordered interfacial component was particularly poor (cf. Fig. 26). Furthermore, it was not possible to reproduce the experimental data by assuming an enhanced thermal diffuse scattering but

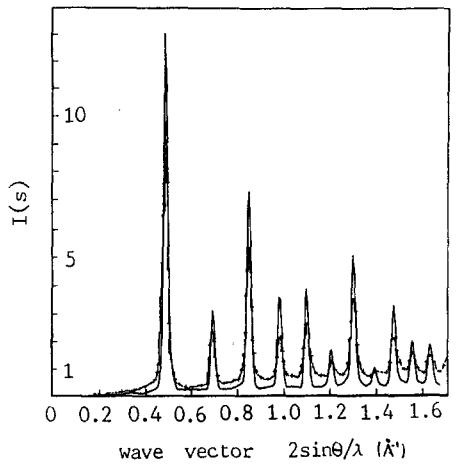

FIG. 26. Comparison of the measured (– – + – –) and computed (——) interference functions for nanocrystalline Fe. The model system assumed for the computations is a boundary structure consisting of four atomic layers in which atoms are displaced in random directions. The displacement distance of the atoms corresponding to the two layers in the boundary core are assumed to be 15% of the nearest neighbor distance, in the two adjacent layers the displacements are 7% of the nearest neighbor distance. The displacement of 15% of the nearest neighbor distance corresponds to the average nearest neighbor displacement of the atoms in a $Fe_{80}B_{20}$ glass.[173]

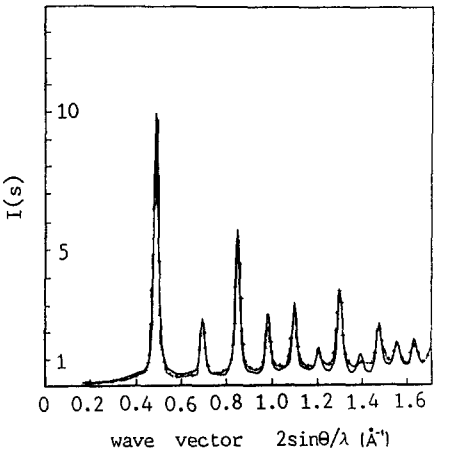

FIG. 27. Comparison of the measured (– – + – –) and computed (——) interference functions of nanocrystalline. The model computed is a mixture of 6 nm (75 vol.%) and 4 nm (25 vol.%) crystals in which the boundary atoms are displaced in random directions. The displacement distances were chosen as follows. The outer layer of atoms was displaced by 50% and the second and third layer by 25% of the nearest neighbor distance. The outer layer is supposed to model the interatomic spacings between adjacent crystals (arrows in Fig. 25). The second layer models the displacements of the boundary core atoms (open circles in Fig. 25) from their ideal lattice sites.[173]

no scattering of the boundary region as was suggested by other studies.[178] The accuracy of the computations was tested by comparing the measured and computed interference functions of 6 nm Au crystals which were isolated from one another by a thin water layer so that no grain boundaries can be formed. The computed and experimental data agreed (no adjustable fit parameters) within the accuracy of the measurements.

A different approach to analyze the structure of the grain boundaries in nanocrystalline metals has recently been proposed.[179] In comparison to Zhu's[3] computations, several simplifications were introduced. In order to shorten the computation of the interference function, the real (three-dimensional) nanocrystalline material was replaced by a one-dimensional model consisting of two linear arrays of scatters. One array represents the periodicities in the grain interior, while the other one, with a larger periodicity, corresponds to the boundary region. The volume fraction of the boundaries was taken into account by multiplying the diffracted amplitude of the boundary scatters by a corresponding weight factor. The different boundary structures and the density difference between the boundaries and the crystals was accounted for by varying the density in the boundary region between 60 and 100% of the bulk density. The spacing between the scatters ranged from 50 to 150% of the scatterer density in the "grain interior". The random orientation distribution was approximated by assuming that every "crystal" (row of scatterers) has either (111), (200), (220), (311) or (311) interatomic spacings. A random number generator was used to average over the spacings. The measurements were simplified by replacing the commonly used transmission measurements allowing quantitative measurements of the interference function (with the appropriate corrections) by a reflection measurement on a glass slide. The unavoidable background had to be subtracted, which was only possible to a limited extent. Due to the numerous simplifications in the computational and the experimental part of the work, no direct comparison (without free fit parameters as in Zhu's[3] work) was possible. Hence, the computed and measured interference functions were fitted together in a suitable chosen scattering angle, 2θ. The angle selected was $2\theta = 55°$, well away from any Bragg peak to match the background as well as possible. Despite this curve fitting procedure, the computed and measured intensity of the Bragg peaks deviated by a factor between 8 and 12. In order to reduce this discrepancy, the assumption of 20% vacancies in the "crystals" was made. Evidently, this assumption appears unrealistic and is at variance with many observations e.g. with the hydrogen absorption data on nanocrystalline Pd (cf. Section 3.7.4). The paper seems to demonstrate that reliable information about the grain boundary structure of nanocrystalline materials cannot be obtained by simplified models and X-ray diffraction measurements limited to relative intensities only.

The X-ray diffraction behavior of thin nanocrystalline Ag–Cu and Ag–Ge films generated by vapor-quenching has been analyzed[178,180] in terms of the interference function of an ensemble of small strained crystallites. The boundaries were modeled by an appropriately chosen Debye-Waller factor for the crystallites. In other words, the real structure (boundaries and crystals) is modeled as an arrangement of small, elastically strained, isolated crystals. The boundaries are represented by means of lattice strains. All other boundary features (cf. Section 1) are not included. As far as the diffraction properties of those two systems are concerned this model seems to be satisfactory. Nevertheless, a model of this kind does not seem applicable to obtain information about the atomic structure of the boundary core components. For example, the EXAFS measurements reported in the subsequent section not only suggest displacements of the atoms in the boundary core but also a reduction in the number of nearest neighbors which cannot be described by a model limited to small strained crystallites. Furthermore, the application of a model assuming a nanocrystalline material to

consist of small, strained crystallites only (without any scattering from the boundary core regions) seems inconsistent with the reported small angle X-ray diffraction measurements (Sections 3.3.1.2 and 3.3.2.1). The strain required to match the peak widths and peak heights does not reproduce correctly the observed background of nanocrystalline Fe. This means physically that in addition to the scattering by strained Fe-crystallites, the X-rays are also scattered by Fe-atoms displaced by large distances from lattice sites.

As the atomic structures in the cores of boundaries depend strongly on the interatomic forces (cf. Section 1), it may well be that the diffraction behavior of chemically different nanocrystalline materials deviate strongly from one another. Hence any structural model deduced for a particular material cannot be extended to other materials unless tested experimentally. Hence the diffraction of nanocrystalline Ag–Cu alloys may well differ from nanocrystalline Fe. On the other hand, any model describing the diffraction of nanocrystalline materials in terms of strained crystallites only (without any scattering contribution from the boundary core) seems inconsistent with the small angle X-ray diffraction experiments and the work of Sass *et al.* (e.g. Refs 173 and 181). These experiments have demonstrated that grain boundary core regions generate specific diffraction effects which originate from the displacements of the atoms in the boundary core from lattice sites. A "strained crystallite" model seems also inconsistent with the spectroscopic evidence (Section 3.7) indicating that nanocrystalline materials contain a high density of vacancy-like free volume and a considerable fraction of atoms in sites with non-lattice symmetry.

3.6.2. *EXAFS studies*

EXAFS studies[190] appear to be particularly suitable to investigate the structure of nanocrystalline materials because they yield information about the short-range order of a solid in terms of the coordination numbers, the nearest neighbor distances, the Debye-Waller factors, etc.[182–184] In fact, if a nanocrystalline material consists of an (ordered) crystalline component and a grain boundary component formed by atoms displaced from their ideal lattice sites, then the EXAFS oscillations of a nanocrystalline material result from the crystalline component only, because materials with a wide variety of interatomic spacings yield little or no oscillations in the EXAFS signal.[182] Hence, in terms of such a model the amplitudes of the EXAFS oscillations of a nanocrystalline material in comparison to the amplitudes of a conventional polycrystal with the same mass are expected to be reduced by a factor comparable to the fraction of atoms located in the boundary cores if these atoms are displaced significantly from ideal lattice sites and if the interatomic spacings within the boundary core (arrows in Fig. 25) are distributed randomly. In fact, it is this feature which has been observed in all EXAFS studies performed so far. In Fig. 28a the weighted EXAFS oscillations χk^3 of nanocrystalline and polycrystalline Cu are compared. The corresponding Fourier transformed FT(χk^3) are summarized in Fig. 28b. Pd showed similar results. The following three features are apparent.

(i) The radii of the different shells in polycrystalline and nanocrystalline materials coincide, the deviation is below 0.02 Å (Fig. 28b).

(ii) The amplitudes of FT(χk^3) of the first shell are reduced by an amount comparable to the volume fraction of the grain boundary component. The same effect has been reported recently for $Fe_{60}Co_{40}$ alloys.[191]

(iii) The reduction of the amplitude of FT(χk^3) increases with increasing shell number.

These features agree with the idea that nanocrystalline materials consist of an (ordered) crystalline component with the same atomic arrangement as in bulk crystals and a grain

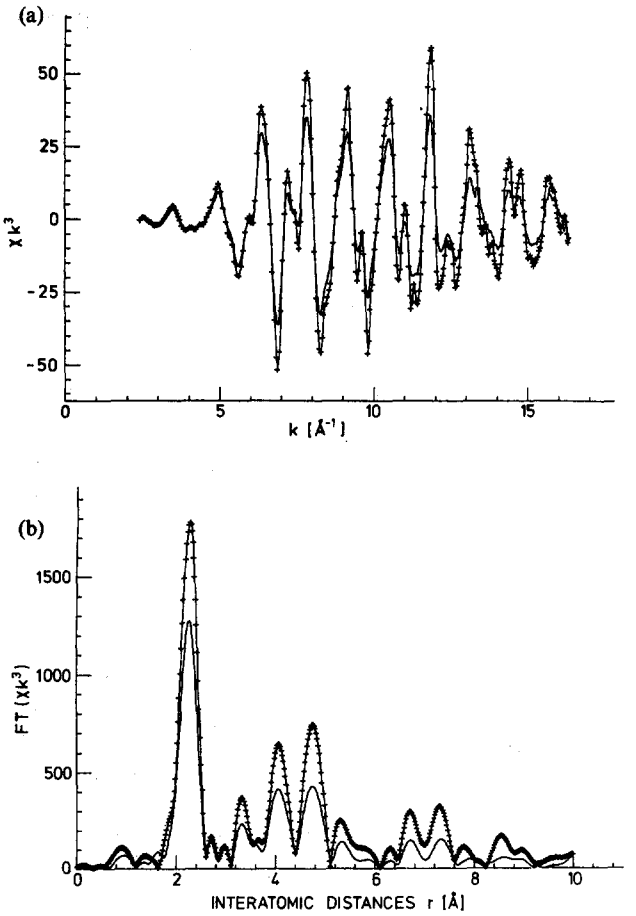

FIG. 28. The weighted EXAFS oscillations χk^3 (a) and the Fourier transform FT (χk^3) (b) (phase shift is not included) of a nanocrystalline Cu sample (——) (crystalline diameter = 10 nm) in comparison with polycrystalline Cu (+ + +). In the nanocrystalline sample the amplitude of the EXAFS oscillations and the FT (χk^3) are weaker than in the polycrystal.[190]

boundary component with a broad distribution of interatomic spacings. The features (ii) and (iii) cannot be interpreted in terms of internal surfaces and/or voids because the observed reduction of the EXAFS amplitudes would require an area of internal surfaces or voids which are inconsistent with the results of positron lifetime spectroscopy[185] and small angle diffraction.[147,148] The X-ray diffraction studies (Section 3.6.1) indicated that the interatomic spacings in the small crystallites deviate little from the equilibrium (bulk) value.[186,187] Hence, the radii of the different shells of polycrystalline and nanocrystalline materials are expected to coincide as was observed. Atoms with a wide spectrum of interatomic spacings relative to their neighbors cannot contribute to the amplitudes of the FT(χk^3). Thus, the reduction of the amplitude of the first shell should be comparable to the fraction of interfacial atoms, as was observed. The results rule out a glassy (short range ordered) boundary structure. In the case of glassy boundary structures, the intensity of the first shell of the FT(χk^3) is reduced by 10 to 30% in comparison to the crystalline counterpart. Higher order shells of glasses in the FT(χk^3) plot are either weak or invisible.[184,188] Hence, if the boundary component of a nanocrystalline material would have a glassy structure, the intensity loss of the first shell in

the FT(χk^3) should be about 10 to 30% of the fraction of boundary atoms. This was not observed. Furthermore, a significant reduction of the higher order shells (second, third, etc.) relative to the first shell should be observed. This was also not the case. The results are not consistent with a glassy boundary structure with a large Debye-Waller factor for the following reasons. The mean square displacements (static or dynamic) in the Debye-Waller factor cannot explain a density reduction in the grain boundary component which was deduced to be about 60 or 70% of the bulk density (cf. Sections 3.3.1.2 and 3.3.2.1).[147,148] Recent measurements at 20 K show the same reduction of the EXAFS amplitudes as at 77 K indicating that there is, up to 20 K, no temperature dependence of the reduction. This observation clearly contradicts a Debye-Waller factor being the reason for the amplitude reduction. Hence, one is led to conclude that the observed deviation of the EXAFS signal between the polycrystalline and nanocrystalline material is primarily due to a wide distribution of bond lengths in the grain boundaries.

It has been argued on the basis of hard sphere and soap bubble models[189] that a structural model of a nanocrystalline material suggesting a measurable fraction of the boundary atoms to be displaced by 50% of the nearest neighbor spacing from lattice sites is unrealistic. This objection seems to be based on a misunderstanding of the model used to compute the interference function of a nanocrystalline material.[2] As was pointed out above (Section 3.6.1), the random atomic displacements of 50% of the nearest neighbor spacing were used to model the ensemble average over the interatomic spacings between adjacent crystals (i.e. the spacings indicated by the arrows in Fig. 25). On the other hand, the EXAFS observations reported in the previous paragraph and the strong background observed for nanocrystalline Fe seem to indicate unambiguously that a large fraction of the atoms of a nanocrystalline material are displaced from lattice sites.

3.7. *Spectroscopy*

3.7.1. *Positron lifetime spectroscopy*

Positron lifetime spectroscopy has been demonstrated to be particularly well suited for studying defects in crystals[192–194] and structural fluctuations in amorphous materials[195] because they permit an estimate of free volume fluctuations in condensed matter. Hence positron lifetime spectroscopy appeared to be a promising tool to obtain independent information about the structure of nanocrystalline materials. So far, studies of this type were performed for Cu, Fe, Pd and Si.[196–200]

The lifetime spectra (Fig. 29) measured for the nanocrystalline metals differ from those obtained on uncompacted crystallites or on the metallic glass $Fe_{85}B_{15}$[196] and can be analyzed with good variances ($\chi^2 \leqslant 1.1$) by three components with lifetimes τ_1, τ_2, τ_3 and intensities I_1, I_2, I_3. These parameters are given in Table 1 together with the lifetimes τ_f in perfect crystals and τ_{LV} in lattice vacancies and can be interpreted as follows.

The lifetime τ_1 is attributed to free volumes of the size of about a lattice vacancy as their values are similar to τ_{LV} (see Table 1). The vacancy-size free volumes are expected to be located in the interfaces because of their thermal stability and the increase of the ratio I_1/I_2 with compacting (see Ref. 198). The presence of vacancy-size free volumes in NiO grain boundaries has recently been suggested by a comparison of high-resolution electron microscopy and image simulation.[201]

The lifetime τ_2 (Table 1) is attributed to boundary regions at which the local free volume is larger than a single vacancy. For example, the core of a triple junction between three

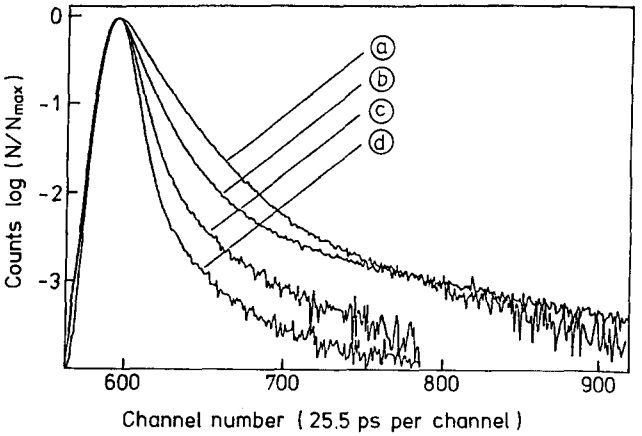

FIG. 29. Positron lifetime spectra of: (a) an uncompacted (6 nm) iron powder; (b) a nanocrystalline (6 nm) iron specimen; (c) amorphous $Fe_{85.2}B_{14.8}$ alloy; and (d) polycrystalline bulk iron, with the background of the spectra substracted.[199]

boundaries may represent such a region. The lifetime τ_2 was attributed to triple junctions because τ_2 was observed even after prolonged grain growth. For topological reasons triple junctions cannot anneal out whereas other large free volumes, e.g. microvoids in boundaries may disappear.[196–200] The long-lived component (τ_3) was interpreted by ortho-positronum (o-Ps) formation in larger voids.[198,199] Some indication of interfacial free volumes smaller than vacancies were deduced from the decrease between 295 K and 77 K in nanocrystalline Fe and in nanocrystalline Cu.

3.7.2. *Muon spin rotation studies*

In order to obtain spectroscopic information about the microscopic magnetic structure of nanocrystalline materials the muon spin rotation technique (μ^+SR) has been employed. By this method—which probes magnetic fields and their dynamics at the μ^+ sites in crystals[202]—structural defects acting as μ^+ traps may be characterized. Two muon spin precession frequencies f_1 and f_2 and a longitudinal muon spin relaxation rate Γ_{long} have been observed (Table 2) for a fraction of the muons. The precession frequencies f_1 and f_2 are similar to those observed for interstitial μ^+ in the Fe (f_f)[203] and for μ^+ trapped at lattice vacancies (f_{IV}).[204] Therefore, it was assumed that f_1 is characteristic for μ^+ on interstitial sites in the crystallites and f_2 for muons trapped in well-defined free volumes, namely of the size of about a lattice vacancy, in the interfaces. This interpretation agrees with the positron annihilation data reported in the previous section. The ratio A_1/A_2 of the signal amplitudes of the

Table 1. Positron Lifetimes τ_1 (ps) and Intensities I_1 (%) Measured on Nanocrystalline Copper, Palladium and Iron Consolidated Under Pressure p. For Comparison, Positron Lifetimes Measured in the Free Bulk State (τ_f), in Monovacancies (τ_{Liv}) and after Plastic Deformation (τ_{plast}) in the Corresponding Bulk Crystals are Given (see Ref. 198)

	Nanocrystalline materials					Crystalline materials		
p (GPa)	τ_1 (ps)	τ_2 (ps)	I_1/I_2	τ_3 (ps)	I_3 (%)	τ_f (ps)	τ_{Lv} (ps)	τ_{plast} (ps)
Cu 5.0	165 ± 3	322 ± 4	0.57	2600 ± 300	0.2 ± 0.0	112	179	164
Pd 5.0	142 ± 3	321 ± 6	0.72	700 ± 100	2.6 ± 0.7	96	Pt: 169	171
Fe 4.5	185 ± 5	337 ± 5	0.63	4100 ± 400	8.5 ± 0.5	106	175	167

Table 2. Muon Spin Precession Frequencies f_1, f_2 and the Ratio A_1/A_2 of their Signal Amplitudes, as well as the Longitudinal Muon Spin Relaxation Rate Γ_{long} at Two Different Temperatures. The Precession Frequencies f_I and f_{IV} of the Muons at Interstitial Sites and Muons Trapped in Vacancies in Crystalline Iron are Included for Comparison

	Nanocrystalline Fe				Crystalline Fe	
T (K)	f_1 (MHz)	f_2 (MHz)	A_1/A_2	Γ_{long} (10^8 s^{-1})	f_I (MHz)	f_{IV} (MHz)
300	48.9	31.5	0.5	2.9	48.7*	
4.2	53.8	32.6	2.1	0.3	53.3*	
90						29.5†

*Ref. 203.
†Ref. 204.

frequencies f_1, f_2 decreasing with increasing temperature indicates that at 300 K more muons decay in the interfaces and less in the crystallites than at 4.2 K. This result is in qualitative agreement with the μ^+ jump rates[203] Γ (4.2 K) $= 4 \cdot 10^8$ s^{-1} and Γ (300 K) $= 10^{10}$ s^{-1} making a diffusion of μ^+ to the interfaces more likely at the higher temperature. From higher precision data combined with a study of the crystallite size distribution, one may even expect a quantitative determination of the μ^+ diffusivity. Only a fraction of the μ^+ was detected in the μ^+ precession signals. The missing fraction was attributed to muons trapped in interfacial regions with varying interatomic distances and hence a wide distribution of local magnetic fields leading to a fast relaxation of the μ^+SR signals which is beyond the resolution of the apparatus.

3.7.3. *Mössbauer spectroscopy*

The Mössbauer spectrum of nanocrystalline iron is shown in Fig. 30.[205] Two sub-spectra were used to fit the experimental data, the hyperfine parameters of which are given in Table 3. Since wide-angle X-ray scattering and EXAFS (cf. Sections 3.6.1 and 3.6.2) gave little evidence for large lattice distortions in the center of the crystals, the initial fit parameters

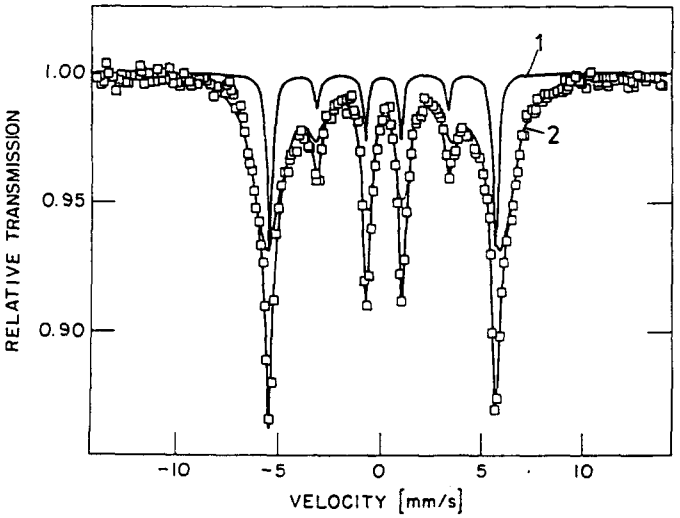

FIG. 30. Mössbauer spectrum of a nanocrystalline iron sample. The spectrum was measured at 77 K. Two sub-spectra (1, sharp lines; 2, broad lines) were used to fit the experimental data (squares).[205]

Table 3. Hyperfine Parameters of Sub-spectra 1 and 2 of Fig. 30

	Sub-spectrum 1	Sub-spectrum 2
IS (mm/s)	0.10	0.14
Linewidth at half-maximum (mm/s)	0.32	1.6
H (kOe)	343	351

of sub-spectrum 1 were chosen as the values of crystalline iron which was confirmed by the fit procedure; the fit parameters of sub-spectrum 2 deviated from the crystalline values (Table 3).

The absorption intensity of spectrum 2 relative to spectrum 1 may not be a reliable way to estimate the fraction of atoms located in the interfaces because magnetic ordering extends over more than interatomic distances. Hence, atoms inside the crystals are also influenced by the interfacial component even if they have a well ordered crystalline environment. This is not so for materials (e.g. FeF_2 which will be discussed later) in this section where the interaction with the neighboring atoms is of short range character.

Sub-spectrum 2 (Table 3) shows an enhanced hyperfine magnetic field (*H*), a larger linewidth, and an increased isomer shift (*IS*) in comparison to the crystalline component. All of these features may be understood if it is assumed that sub-spectrum 2 originates from the interfacial component of the nanocrystalline material. This interpretation agrees with the following observation. If the grain boundaries are removed from a nanocrystalline material (by grain growth at elevated temperatures), sub-spectrum 2 ceases to exist (Fig. 21).[138,205] The enhanced *IS* (Table 3) reflects a reduction of the electron density of the interfacial component. In contrast, from high-pressure Mössbauer experiments it is known that compression of iron leads to a smaller *IS* value as a result of higher electron density.[206,207] The reduction of electron density in the case of nanocrystalline Fe may be directly related to the observed lower mass density which implies a volume expansion in the interfacial component. This result agrees with the small angle scattering data suggesting a mass density of 60 to 70% in the boundaries (cf. Sections 3.3.1.2 and 3.3.2.1). The enhanced hyperfine field (*H*, Table 3) may also be interpreted in terms of the reduced interfacial density. The Bethe–Slater curve, which relates the exchange energy to the atomic geometry, supports this correlation. Again, high-pressure experiments show that a compression of α-Fe results in the opposite effect, i.e. a reduced hyperfine field.[207] The broadness of the Mössbauer lines (Table 3) suggests the interfacial component to represent an atomic structure in which a wider spectrum of interatomic spacings exists than in the glassy or crystalline state of the chemically identical material. A structure of this type should lead to a broad distribution of hyperfine fields.

Figure 31 summarizes the measured temperature variation of the hyperfine field of both components. The larger value of *H* of the sub-spectrum 2 is followed by a faster decrease which may be interpreted as a lower Curie temperature T_c of the interfacial component. Similar curves are known from the observations on thin films[208,209] although the temperature dependence of *H* found there could not be confirmed for nanocrystalline Fe. In order to obtain an estimation of this effect, the total resonant absorption of the sample was determined as a function of temperature by measuring the area under the absorption lines. The total resonant absorption was fitted with a Debye equation leading to a Debye temperature of 345 K which has to be compared with the bulk value of 467 K.[210]

Mössbauer spectroscopy has also been applied to study the structure of nanocrystalline materials (FeF_2, α-Fe_2O_3, γ-Fe_2O_3 and CoO) with ionic bonding. The Mössbauer spectrum of nanocrystalline FeF_2 (average crystal size 8 nm, produced by inert gas condensation; Figs 32 and 33) shows a quadrupole distribution.[211] With the assumption of an average value for the quadrupole splitting, two doublets were identified (Fig. 32) having nearly equal

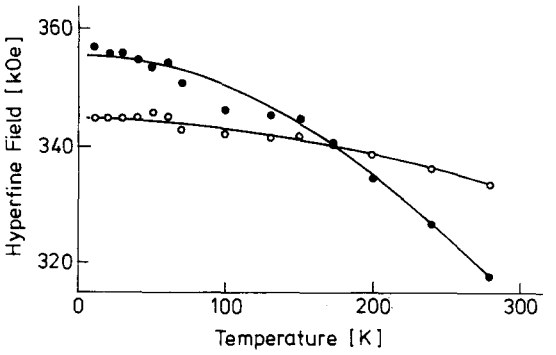

FIG. 31. Hyperfine magnetic field $H(T)$ of sub-spectra 1 and 2 (Fig. 34) obtained by least-squares fits.[205]

isomer shift. One doublet corresponds to bulk FeF_2. The second doublet exhibited a broad distribution of quadrupole splittings with an average value of 1.97 mm/sec (Fig. 33). This component was suggested to originate from the Fe atoms located in the grain boundaries. In addition, low temperature measurements indicated an antiferromagnetic transition temperature extending over about 70 K instead of the sharp transition observed in a FeF_2 single crystal.[256] The smearing out of the antiferromagnetic transition seems to be an indication of a wide variety of atomic (non-lattice) configurations in the grain boundaries. A comparable wide range of antiferromagnetic transition temperatures (242 K to 135 K) compared to the

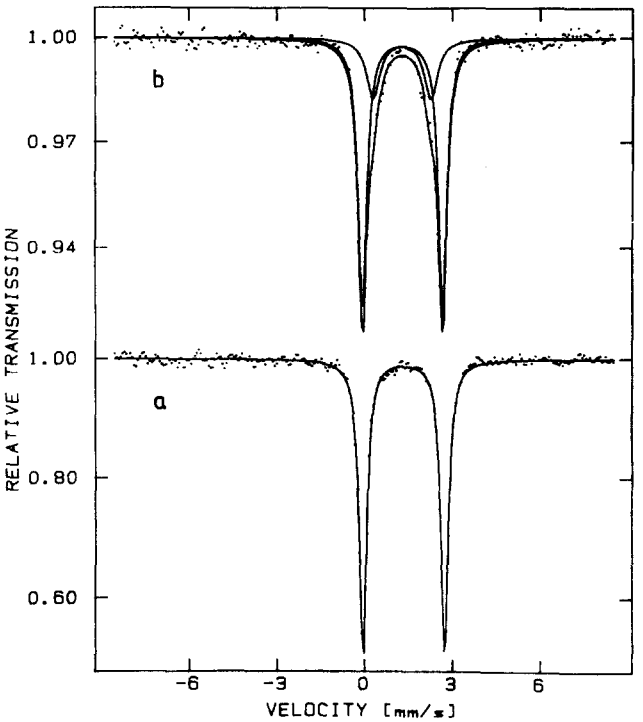

FIG. 32. Quadrupole splitting (Q.S.) of the Mössbauer spectra of (a) commercial and (b) nanocrystalline (8 nm) FeF_2 specimens.[211]

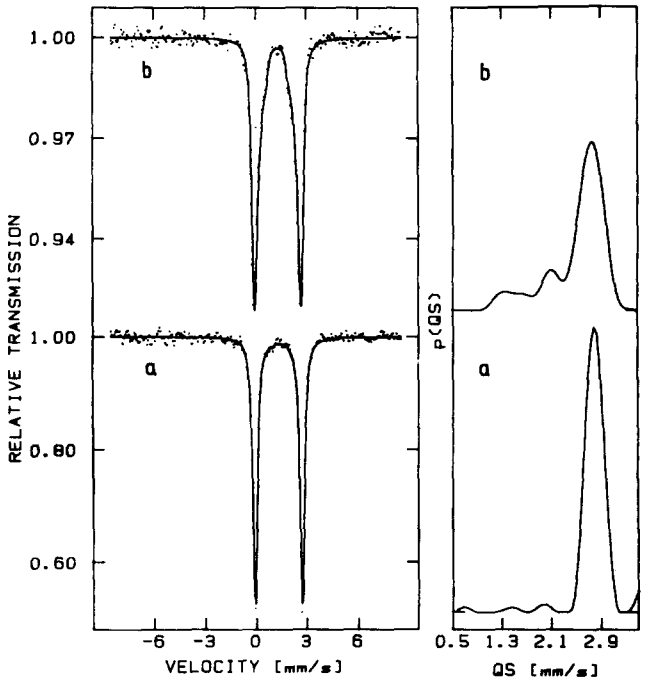

FIG. 33. Mössbauer spectra and the Q.S. distributions of (a) commercial and (b) nanocrystalline FeF_2 specimens.[211]

bulk transition at 288 K was noted in CoO[258,259] and attributed to atoms in non-lattice sites. A comparable distribution was noticed in the hyperfine field of nanocrystalline α-Fe suggesting the non-lattice arrangement of atoms in the grain boundaries of metallic as well as ionic nanocrystalline materials. Similar results were obtained[212] for nanocrystalline γ-Fe_2O_3 and α-Fe_2O_3 (6 nm crystal size). Figures 34 and 35 show the Mössbauer spectra of both materials. Just like in the case of nanocrystalline Fe and FeF_2, the spectra deviated from the ones of the corresponding single crystalline substances with the same chemical composition. In addition to the spectra of the single crystalline material, a second broad component was observed in the nanocrystalline form. The characteristic features of this second component are summarized in Table 4. The reduced hyperfine field and the increased line width suggest

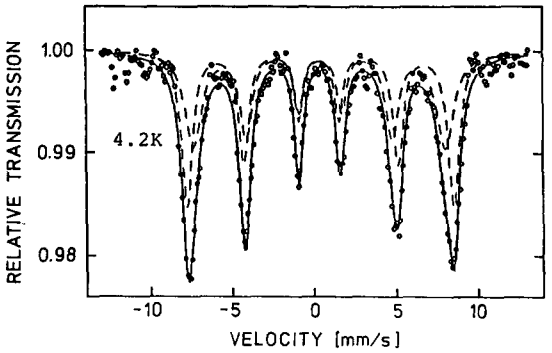

FIG. 34. Mössbauer spectrum of nanocrystalline γ-Fe_2O_3 (5 nm) recorded at 4.2 K.[212] The broken lines indicate the narrow (lattice) and broad (boundary) component of the spectrum (cf. Table 4).

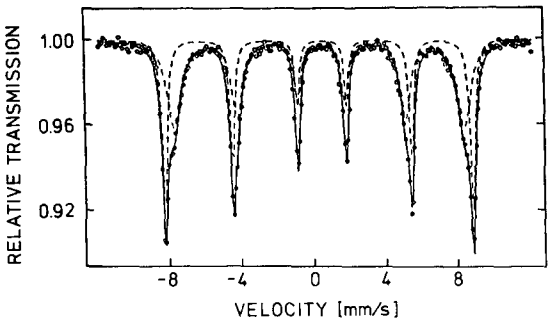

FIG. 35. Mössbauer spectrum of nanocrystalline α-Fe_2O_3 (8 nm) recorded at 10 K.[212] The broken lines indicate the narrow (lattice) and broad (boundary) component of the spectrum (Table 4).

a spectrum of different sites with non-lattice arrangements for the Fe atoms in the grain boundaries of nanocrystalline α-Fe_2O_3 and γ-Fe_2O_3. A similar reduction of the hyperfine field as indicated in Table 4 was also reported by Ayyub *et al.*[257] who studied nanocrystalline (5 to 70 nm diameter) α-Fe_2O_3 by Mössbauer spectroscopy. The results of the structural studies on nanocrystalline FeF_2, α-Fe_2O_3 and γ-Fe_2O_3 and CoO seem at variance with investigations by means of Raman scattering (cf. Section 3.7.5) on nanocrystalline TiO_2.

3.7.4. *Hydrogen absorption*

In many non-crystalline materials hydrogen can be incorporated into interstitial sites, the energy of which depends on the local atomic arrangement. Hence the grain boundary component of a nanocrystalline material may be expected to exhibit a continuous spectrum of hydrogen site energies whereas the crystallites exhibit discrete spectrum of sites such as octahedral and/or tetrahedral sites. In other words, measurements of the hydrogen solubility as a function of the hydrogen potential yield structural information about a given material. This method was applied to study the structure of nanocrystalline Pd. The measured[213] solubility of hydrogen in crystalline and nanocrystalline Pd is compared in Fig. 36. Because only one type of site is occupied by hydrogen in a Pd single crystal, the emf follows Nernst's law (emf linearly dependent for hydrogen concentrations). Above 1% hydrogen, a phase separation occurs at 293 K in the single crystal. For the nanocrystalline palladium the hydrogen solubility is larger by about one to two orders of magnitude due to the higher density of sites into which the hydrogen can be incorporated in the boundary regions. This result is consistent with the reduced atomic density (cf. Sections 3.3.1.2 and 3.3.2.1) in the boundaries. As the sites within the grains are probably the same as in a macroscopic single crystal, the local concentration of hydrogen has to be the same in the grains as in the single crystal for a given equilibrium pressure of hydrogen. Therefore, from the difference between the total concentration in nanocrystalline Pd and that in single-crystalline Pd the amount of

Table 4. Mössbauer Data of Nanocrystalline α-Fe_2O_3 and γ-Fe_2O_3

		Hyperzne field (kOe)	Isomer shift (mm/s)	Quadrupole splitting (mm/s)	Line width (mm/s)
α-Fe_2O_4 (10 K)	Crystalline component	532	−0.09	0.431	0.35
	Interfacial component	501	−0.05	0.431	0.93
γ-Fe_2O_3 (4.2 K)	Crystalline component	505	−0.02	0.46	0.81
	Interfacial component	478	+0.01	0.37	1.25

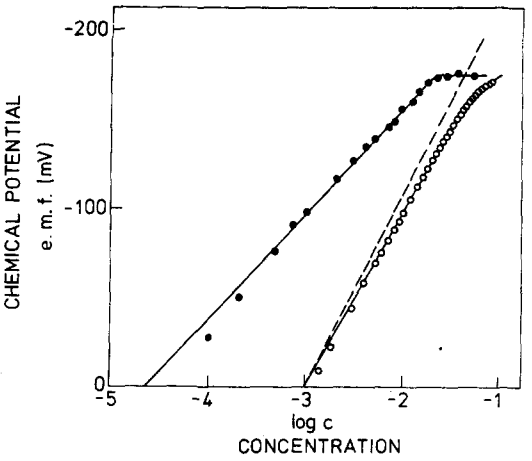

FIG. 36. Emf or chemical potential of hydrogen in a single crystal of Pd (●) and in nanocrystalline Pd (○) as a function of hydrogen concentration (ratio of hydrogen to palladium atoms) at 293 K. The straight line through the data points for the single crystal has the theoretical slope of RT/F (where R is the gas constant and F is the Faraday constant). The lines through the data points for the nanocrystalline Pd are calculated by assuming a gaussian distribution of site energies for hydrogen within the grain boundaries (---, without H—H interaction).[213]

hydrogen segregated at grain boundaries may be calculated. It has been shown[214] that the segregated hydrogen does not follow a simple Langmuir–McLean equation because a spectrum of site energies exists for the hydrogen atoms in the grain boundaries whereas the Langmuir–McLean equation assumes all sites to be energetically equivalent. If a gaussian distribution for the hydrogen sites in the boundaries with a width of 15 kJ $(\text{mol}H)^{-1}$ is assumed, the measured solubility may be described satisfactorily for lower concentrations (cf. Fig. 36). At higher concentrations, the concentration at the grain boundaries becomes so high (greater than 10%) that hydrogen–hydrogen interactions have to be included. This was done by the quasi-chemical approach using the interaction parameter of polycrystalline Pd.[214] As may be seen from Fig. 36 this approach yields remarkable agreement between calculated and measured solubilities.

If a phase separation occurs in metal/hydrogen systems, the chemical potential or the hydrogen pressure remains constant within the two-phase region, although the total hydrogen concentration in the system increases. This behavior was observed in crystalline and nanocrystalline Pd. The experimental results, presented in Figs 37 and 38, show that the β phase is formed in nanocrystalline Pd (Fig. 38) as a plateau occurs at the same hydrogen activity at which the β phase is formed in polycrystalline Pd (Fig. 37). However, less hydrogen is absorbed in nanocrystalline Pd (44at%) in comparison to a polycrystalline Pd specimen (58at%), before the activity rises again, which was attributed to the exclusion of a considerable volume fraction of the sample from the phase transformation. This volume fraction belongs to the distorted regions at the grain boundaries. The β phase forms within the grains of nanocrystalline Pd because they offer the same octahedral sites for hydrogen occupation as in a single crystal of Pd, suggesting that the small crystallites do not contain a high density of defects to which the hydrogen can segregate. The electronic or elastic hydrogen–hydrogen interaction causes the β phase to form at the same hydrogen activity, whereas the distorted regions in or close to the grain boundaries do not permit a phase transformation. The same effect was noticed in glassy metals. This result may be understood

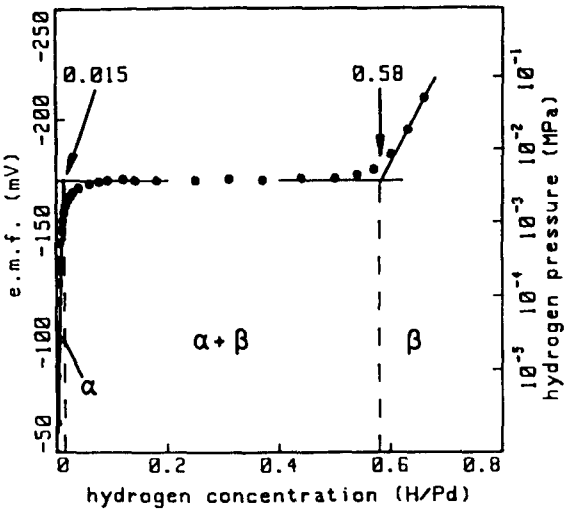

FIG. 37. Pressure-composition isotherm (333 K) for hydrogen in polycrystalline Pd (average diameter, 20 μm). The pressure plateau between H/PD = 0.015 and 0.58 corresponds to the coexistence range of the α and β phases.[213]

if it is assumed that the width of the distribution of the hydrogen sites is larger than the H–H interaction energy.[215]

From the different widths of the two-phase region in polycrystalline and nanocrystalline Pd (average grain diameter, 20 μm and 11 nm), the volume fraction of the grain boundary regions to which the hydrogen can segregate may be calculated assuming the boundaries to be excluded from the β phase formation. A value of 0.27 is obtained for the boundary volume fraction,[216] yielding a grain boundary thickness of about 1 nm.

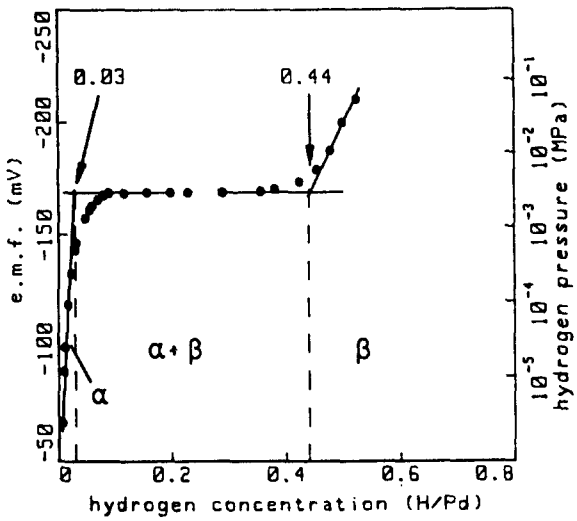

FIG. 38. Pressure-composition isotherm (333 K) for hydrogen in nanocrystalline Pd (average grain diameter, 8–12 nm). The pressure plateau between 0.03 and 0.44 is proposed to be smaller because the solubility of hydrogen is larger in the α phase[140] and because the β phase is formed within the grains only but not within the grain boundary regions.[213]

3.7.5. *Raman scattering*

The structure of nanocrystalline silicon was found, by Raman spectroscopy, to consist of a relatively sharp crystalline feature and a more or less pronounced shoulder at lower frequencies attributed to an amorphous-like component.[217,218] Figure 39 shows a set of Raman spectra for samples deposited at various temperatures, other deposition conditions being kept constant (for experimental details cf. Ref. 218). For comparison, spectra of single crystalline Si (111) wafer (labeled c-Si (111)) and an X-ray amorphous silicon, prepared by a glow discharge decomposition of silane (labeled a-Si), have been included as well. With decreasing deposition temperature, i.e. with decreasing crystallite size, the crystalline component (Fig. 39) broadens and its maximum shifts towards lower frequency. The shoulder seen in the Raman spectra on the lower frequency side of the main peak is more difficult to interpret unambiguously. In some cases it can be resolved into two components (e.g. spectra

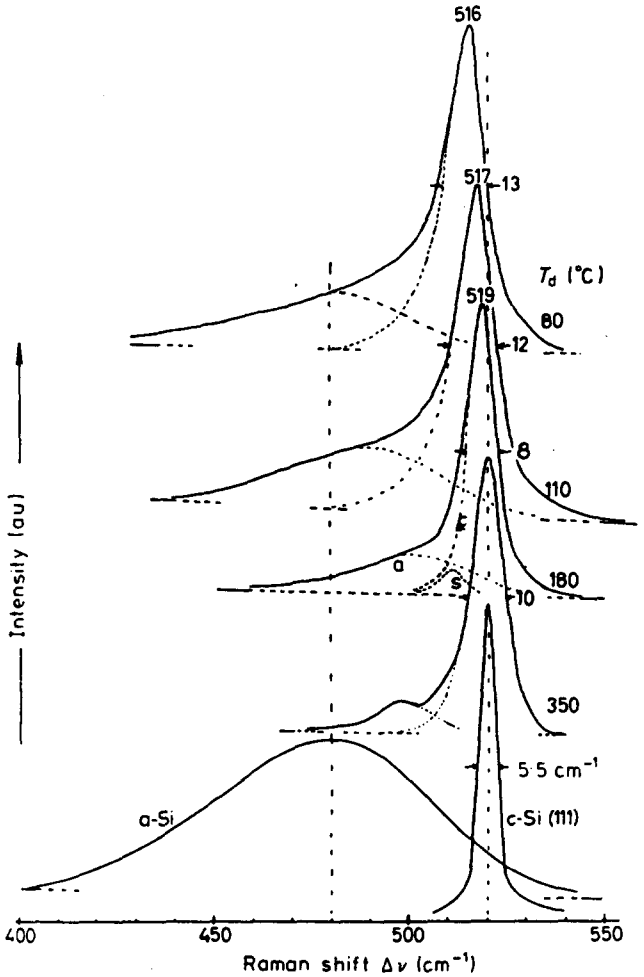

FIG. 39. Raman spectra of polycrystalline silicon films deposited at various temperatures between 80 and 350°C. The 180°C sample was deposited on single-crystal Si (111) wafers, the others on amorphous metals. Raman spectra of single crystal (c-Si (111)) and an X-ray amorphous (a-Si) silicon are shown for comparison as well.[213]

for $T_d = 180°C$, Fig. 39). The component closer to the main peak may be due to surface phonons. In most cases, however, the feature denoted s in Fig. 39 cannot be resolved unambiguously. The integrated intensity of the component denoted a (Fig. 39) increases and the position of its maxima shifts towards lower frequencies with decreasing deposition temperature. It finally reaches a value of about 480 cm^{-1} for a sample deposited at 80°C which is typical of X-ray amorphous silicon.[219] The ratio of the integrated intensities of this component as well as of the crystalline component allows a rough estimate of the ratio of the "amorphous-like" and of the crystalline component in the sample, if proper values for Raman scattering cross sections at a given frequency of the exciting laser light are taken into account. This ratio corresponds approximately to the relative amount of Si atoms at the "surfaces" of the Si crystallites. This interpretation is based on the following structural model. The films are proposed to consist of crystallites embedded in an "amorphous" matrix.* However, on the basis of the present data one also cannot exclude the possibility that the films are built up of thin, quasi two-dimensional crystallites as would be expected according to the theoretical model of Kanellis *et al.*[220] The volume fraction of the "amorphous-like" component as the crystal size was reduced finally merging into the Raman spectrum of X-ray amorphous silicon.[219] This result may be understood as follows. If the crystal size is reduced further and further, the total free energy stored in the boundaries of the nanocrystalline material finally becomes larger than the free energy of a piece of glassy Si with the same number of atoms. In this case, the misfit concentrated in the intercrystalline interfaces de-localizes into a glassy structure because this process reduces the total free energy. In the case of silicon this transition was observed at a crystal size of about 2 nm.[218]

Raman studies have also been performed for nanocrystalline TiO_2 with average grain diameters of about 10 to 100 nm.[221] Although the volume fraction of grain boundaries varied (grain size variation) in different samples between about 3 to 30%, no Raman spectral component was observed other than those from the rutile phase of TiO_2. Hence it was concluded that all grain boundaries of nanocrystalline TiO_2 are comprised of the local atomic structural units of rutile and no other type of disorder exists. This conclusion is at variance with the reported results of X-ray diffraction measurements, the EXAFS data and the various types of spectroscopic studies. In particular, the Mössbauer studies of FeF_2, α-Fe_2O_3 and γ-Fe_2O_3 (Figs 32–35, Section 3.7.3) revealed unambiguously[211,212] that grain boundary structures in ionic nanocrystalline materials consist of local atomic structural units different from the crystalline structure of FeF_2 or Fe_2O_3 (cf. Section 3.7.3). Obviously, this contradiction disappears if the grain boundary component of the TiO_2 had a structure which was not Raman active, and hence no Raman spectral component can be noticed. Unless complimentary measurements by infra-red absorption are performed, the proposed structural interpretation of the Raman data for TiO_2 remains ambiguous.

3.8. *Nanocrystalline Alloys*

By analogy to nanocrystalline materials, nanocrystalline alloys may be generated by simultaneously evaporating or sputtering several components in an evaporator of the kind shown in Fig. 8. Under suitable evaporation conditions[222] a uniform mixture of crystallites with different chemical compositions may be obtained. The subsequent consolidation results in a material which has been termed a "nanocrystalline alloy".[223] In fact, these alloys are

*The term amorphous was used in the sense of non-crystalline and does not necessarily imply glassy.

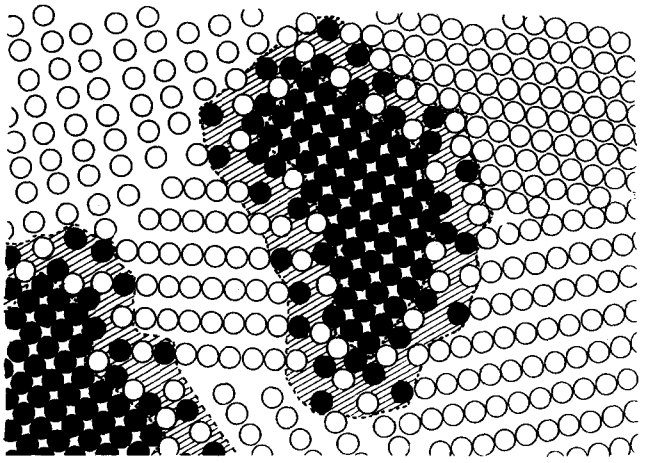

FIG. 40. Schematic model of a nanocrystalline Ag–Fe alloy according to the data of Mössbauer spectroscopy (Fig. 41). The alloy consists of a mixture of nanometer-sized Ag and Fe crystals. In the (strained) interfacial region between Ag and Fe crystals, solid solutions of Fe-atoms in Ag and Ag-atoms in Fe are formed although both components are immiscible in the liquid and/or solid state. For the sake of simplicity the formation of Ag/Fe alloys in the Ag and Fe grain boundaries has been omitted although it is likely to occur as suggested by the grain boundary segregation[222].

polycrystals with a crystal size of a few nanometers consisting of crystallites differing in orientation as well as in chemical composition (Fig. 40). It is one of the attractive features of these alloys that the chemically different atoms (molecules) of the various crystallites are mixed (alloyed) in the interfaces as nearest neighbors irrespective of bulk miscibility, etc. Thus, nanocrystalline alloys permit for example the alloying of metals and ionic materials. Contrary to conventional powder metallurgical alloys, nanocrystalline alloys are expected to exhibit new properties due to the following two factors:

(1) The high density of interphase boundaries between the various components. In these boundaries, atomic structures are formed which do not exist in the crystalline and/or glassy state.

(2) Effects due the small size of the crystallites.

An effect of the first kind was recently observed in nanocrystalline alloys of Cu/Fe and Ag/Fe. Both alloys have been prepared[222] by co-evaporating the two components in He (pressure 1 to 20 mbar). The two systems were selected because they have little (< 100 ppm Cu/Fe) or no (Ag/Fe) measurable mutual solubility at ambient temperature in the bulk. In fact, Ag/Fe are even immiscible in the molten state close to the melting point. The alloy compositions studied were Cu–62 at% Fe, Cu–33 at% Fe and Cu–16 at% Fe. The concentration of several Ag–Fe alloys was less than 50 at% Fe. The crystal sizes in the alloys varied between 6 and 11 nm for Fe, between 7 and 14 nm for Cu and between 6 and 8 nm for Ag. Electron microscopy revealed a homogeneous spacial distribution of the crystallites of both constituents in all alloys studied. This result was confirmed by small angle X-ray scattering. Interference effects between the crystallites of the constituents were noticed which implies that the crystallites are mixed on a length scale ranging between 2 and 50 nm. The atomic structure in the vicinity of the Ag/Fe interphase boundaries was studied by means

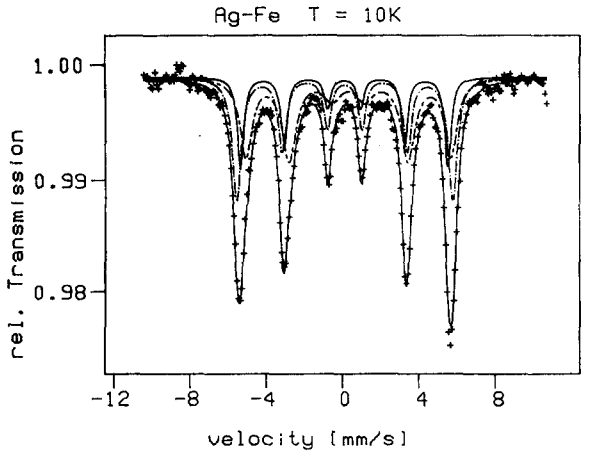

FIG. 41. Mössbauer spectrum of a nanocrystalline Fe–Ag alloy (30 at% Fe, 10 K, crystal size 8 nm). The spectrum consists of the following three components. (i) α-Fe (——), (ii) Fe atoms dissolved in Ag (-.-) and (iii) Ag atoms dissolved in Fe (---)[222].

of Mössbauer spectroscopy (Fig. 41). The observed spectra consist of the following three components.

(i) Fe atoms situated in an Fe crystal with an α-Fe crystal lattice.
(ii) Fe atoms in an Fe–Ag solid solution which consisted primarily of Ag atoms, and
(iii) Fe atoms in an Fe–Ag solid solution which consisted predominantly of Fe atoms and contained only a few Ag atoms.

The structural model proposed to interpret these results is indicated in Fig. 40. In the strained lattice regions in the vicinity of the Ag/Fe interphase boundaries, the solubility of Fe in Ag and the one of Ag in Fe is proposed to be enhanced.* An enhanced solute solubility due to elastic strains has been demonstrated in the past theoretically[224–227] and experimentally[228] for various alloys. The enhanced solubility of Ag in the strained Fe lattice and of Fe in the strained Ag lattice would explain the second and third component of the Mössbauer spectrum. No such components are noticed in conventional polycrystals with the same chemical composition. Hence, the newly formed solid solutions were suggested to be formed at or close to the interfacial regions of the nanocrystalline materials as indicated in Fig. 40. The alternative interpretation in terms of trapped Fe or Ag atoms in Ag or Fe crystals during evaporation was ruled out by separating the vapor sources so far that all evaporated Fe and Ag atoms had condensed in separate regions of the evaporator (Fig. 8) in the form of small crystallites. In fact, similar interfacial alloying effects have been reported by Shingu *et al.*[229] in nanocrystalline Fe–Al alloys generated by ball milling. If the above observations can be generalized, nanocrystalline alloys would open the way to generate solid solutions of components which are immiscible even in materials obtained by rapid cooling. For example, Ag–Fe alloys cannot be generated by rapid solidification or evaporation methods. The interpretation of the Mössbauer spectrum in terms of an interfacial component between Fe and Ag crystals agrees with the results of a Mössbauer study on α-Fe/Cu layer structures.[260] The layer structures exhibited two hyperfine fields, one of which was identical with bulk α-Fe (346 kOe at 4.2 K) and a reduced field (306 ± 8 kOe) which was observed only in specimens

*In addition boundary segregation of Ag and Fe at the grain boundaries between Fe and Ag crystals may also occur.

with a high density of α-Fe/Cu interfaces. Therefore, this component was attributed to Fe atoms located at, or in the vicinity of the α-Fe/Cu interfacial region.

Effects due to the small size of particles have been reported in numerous papers. The main emphasis of this field lies presently on the study and potential use of quantitization effects due to the small particle sizes. The present state of the art in this field has been summarized in several excellent reviews.[230,231] If a small cluster of n atoms or diatoms grows into an sp^3 hybridized bulk semiconductor three regimes may be distinguished as far as the band structure is concerned.[232] For small n, clusters appear to be entirely molecular in that the bulk unit cell is not present, and each cluster n has a different structure. In the second regime, for about $10^2 < n < 5 \times 10^3$ a hybrid molecular-solid state regime occurs. Here, a small crystallite with the unit cell of the bulk material is observed; however, the electrons remain in discrete molecular orbitals. In both these regimes, the cluster interacts with the electromagnetic field via the transition dipole moment, as normally occurs in the molecular spectroscopy. Polariton phenomena are not present. The third regime should occur at about 15 nm diameter. At this point, the crystallite interaction with the field switches from weak to strong, so that local field effects and higher multiple moments become important. This will have an effect on both the linear and non-linear spectroscopy.

In the second regime, the elementary theory of semiconductor clusters predicts a number of interesting phenomena, as discrete molecular orbital electronic states evolve into continuous solid-state bands with increasing size. The solid-state physics community terms these larger clusters "quantum dots" or "zero-dimensional excitons". These small crystallites show quantum confinement of the electron and hole in three dimensions; in the quantum-well thin-layer superlattices studied extensively by solid-state physicists, there is one-dimensional confinement. Optical absorption, fluorescence, and resonance Raman techniques have proven valuable for characterization of semiconductor clusters in the second regime, in liquid colloids, and in transparent dielectrics. Perhaps the most instructive measurement is the size dependence of the crystallite absorption spectrum that occurs when the cluster diameter is comparable to or smaller than the electron-hole exciton diameter in the bulk semiconductor. These diameters are quite large (e.g. about 5 nm for CdS and about 20 nm for GaAs) because of the strong electron delocalization and small effective masses in these materials. The crystallites show discrete states (molecular orbitals) instead of continuous bands in the band-gap region. Figure 42 shows the expected pattern of molecular orbitals for spherical crystallites of CdS (7 nm) and GaAs (14 nm).[233] The strongly allowed transitions conserve the principal quantum numbers, giving the expected pattern of discrete transitions shown at the bottom of the figure. In practice, the blue shift of the lowest 1s to 1s exciton is clearly and easily observed (Fig. 43). Particles larger than about 6 nm, i.e. larger than the size of an exciton in the macrocrystalline material, start to absorb close to 515 nm (or 2.4 eV photon energy), corresponding to the band gap of bulk CdS. With decreasing size, the absorption threshold shifts to shorter wavelengths. CdS consisting of particles below 2.2 nm is colorless. It can be recovered as a white powder from the aqueous solution where it was formed by precipitating Cd^{2+} ions with H_2S in the presence of a small amount of sodium polyphosphate (the solid powder obtained after removal of the solvent also contains the polyphosphate; it prevents the small particles from coming into close contact). In the case of semiconductors having a band gap smaller than that of CdS, the color changes are even more drastic. For example, cadmium phosphide, a black material with a band gap of 0.5 eV, can be made in all colors of visible light by varying the particle size between 10 and 2 nm.[234] The fluorescence band of the coloids is also blue-shifted with decreasing particle size.

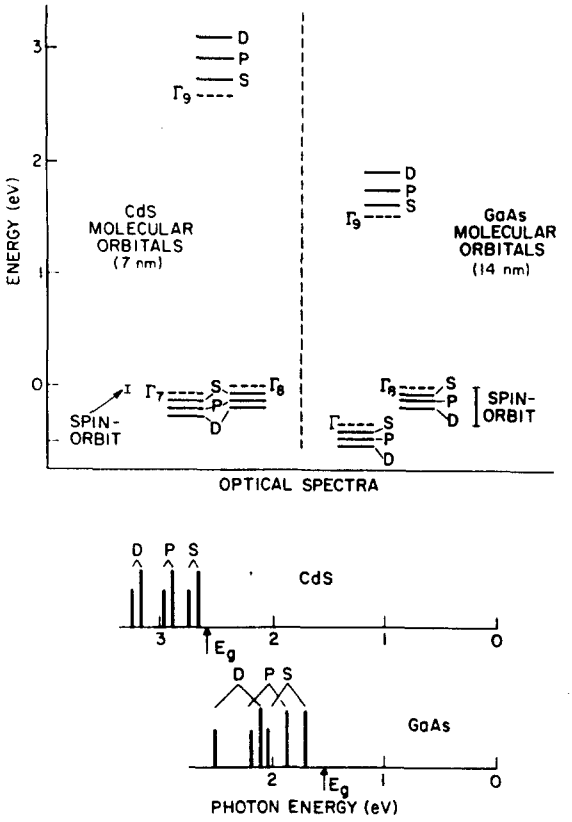

FIG. 42. Expected pattern of molecular orbitals and allowed discrete electronic transitions, for spherical crystallites of CdS (7 nm) and GaAs (14 nm).[233]

The strong transitions seen in optical absorption involve internal crystallite molecular orbitals that have nodes on the crystallite surface.[235,236] These spectra are not sensitive to surface conditions, nor to adsorption of foreign molecules. The cluster luminescence is, by contrast, quite sensitive to surface conditions, and appears to occur from surface localized states. A large percentage of the atoms in a nanometer particle are on the surface, where dangling bonds, adsorbed species, etc. produce traps for electrons and holes. The fate of the charge carriers generated by light absorption is strongly dependent on the existence of these traps. Fluorescence experiments are suitable to demonstrate this fact. Figure 44 illustrates an example. The fluorescence spectrum of a CdS sample is shown here before and after surface modification. CdS colloids made by adding H_2S to a cadmium salt solution have generally a very weak red fluorescence, peaking at a photon energy about 0.4 eV below the absorption threshold. This fluorescence is explained as radiative recombination of trapped charge carriers, the competing radiationless recombination being the dominant process. After surface modification by the addition of Cd^{2+} ions and an increase in pH, a bright green–blue fluorescence is present, the quantum yield exceeding 50%. The maximum of this fluorescence lies at the absorption threshold; i.e. one is dealing with band-gap recombination of the free charge carriers.

Similar effects have been demonstrated for CdSe covered with phenylligands[237] and CdS with CH_3S groups attached to the surface.[238,240] While few hard facts concerning surface

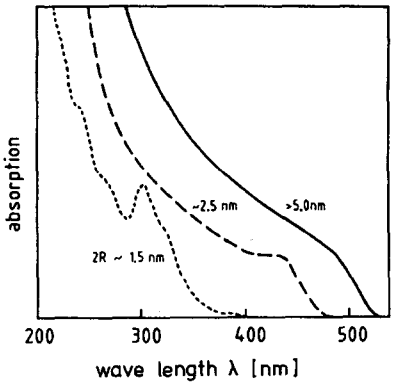

FIG. 43. Absorption spectrum of CdS in aqueous solution: different mean particle sizes.[230]

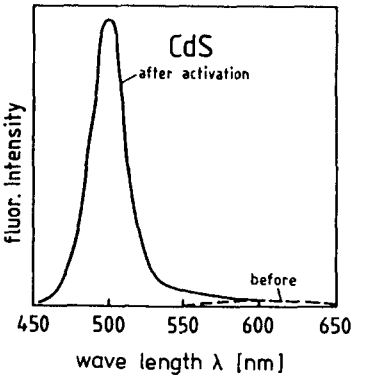

FIG. 44. Fluorescence spectrum of CdS before and after surface modification.[230]

states are presently known, there is a body of indirect evidence that surface adatoms and/or vacancies, adsorbed molecules of the correct redox potentials, and possibly atoms at vertices and/or on edges, provide localized surface states that trap electrons and holes. The trapped electron and hole can recombine either radiatively or non-radiatively. The emission is strongly coupled to lattice phonons, giving a broad continuum strongly red-shifted from the absorption spectrum. The non-radiative recombination shows strong thermal activation typical of strong coupling to lattice phonons. In CdS clusters, there appears to be a correlation between the distance between the trapped charges and the energy of the broad emissions, in a fashion analogous to that of distant donor-accepted pair emission in bulk semiconductors.

Recent work on the coupling of phonons to the internal 1s to 1s absorption transition in about 4.5 nm diameter CdSe crystallites shows there is weak coupling to LO phonons, and stronger coupling to low frequency acoustical phonons. At 4 K the homogeneous width is on the order of 100 cm^{-1}. The coupling to LO phonons also shows up in the resonance Raman spectra of these crystallites. These results apply to isolated, non-interacting semiconductor clusters in dielectric media. Very little is known about the corresponding optical properties in the loose aggregates that are formed in flocculated colloids. In the case of the periodic, three-dimensional array of Cd_4S_4 clusters formed in zeolites, each individual cluster interacts with its nearest neighbors to form a supercluster.[241] This interaction cannot be due to the direct overlap of cluster wavefunctions, since these clusters are separated by about 0.6 and 0.9 nm in zeolite Y and A, respectively. Instead, they interact via through-bond interactions. Quantitative treatment of this problem has not yet appeared. The non-linear optical properties of larger (10 nm to 50 nm) CdS_xSe_{1-x} crystallites in silicate glasses (commercially sold as color-glass filters) have attracted widespread experimental interest.[242] Non-linear optical four-wave mixing experiments have shown large third-order X_3 coefficients and picosecond response times in the available samples. The operative non-linear mechanism is thought to be a simple band filling[243,244] in the few color-glass samples that have been quantitatively investigated. Non-linear optical studies have also been done on CdS clusters in ionomers. It has been shown that the simple band-filling mechanism is not important due to an extremely short carrier lifetime.[245,246] There have been several related theoretical papers on giant oscillator strength[247] local field effects[248] and excitation-induced blue shift.[249]

In the area of metal clusters, there has been extensive work on the optical properties of metallic colloidal particles, individually and in flocculated aggregates.[250] In the diameter range of about 2 nm and larger, quantum size effects as described for semiconductors are generally not present. Nevertheless, observations have been reported[251] which suggest quantum effects to exist even in micron-sized crystals. Photoelectron spectroscopy on mass-selected metal clusters in supersonic jets has shown a size-dependent development of band structure in approximate agreement with the simple jellium model.

3.8.1. *Nanometer-sized sandwich structures*

In a nanometer-sized sandwich structure[230] two different semiconductor parts are connected. Illumination into one part may produce a response in the other part or at the interface between the two. The first example was found in experiments where small amounts of cadmium salt were added to a ZnS sol. As the solubility product of CdS is smaller than that of ZnS, Zn^{2+} ions are substituted by Cd^{2+} ions on the surface of the particles and a layer of approximate composition $CdZnS_2$ is formed. Just a few Cd^{2+} ions on a ZnS particle are sufficient to quench the fluorescence of the latter. At higher cadmium amounts the fluorescence of the 1:1 layer of zinc and cadmium sulfide appears upon illumination into the ZnS part of the sandwich. These findings show that the transfer of charge carriers from one part of the sandwich structure to the other is possible.[252] More recently, sandwich structures between cadmium sulfide as the light-absorbing semiconductor part having a relatively small band gap and titanium oxide or zinc oxide as the large band gap part have been described.[252,253] Such structures form spontaneously when the separately prepared solutions of the colloids are mixed under certain conditions where there is a large excess of Cd^{2+} ions in alkaline solution, polyphosphate acting as stabilizer in a TiO_2 sol. The formation of the sandwich is recognized by the quenching of the fluorescence of CdS. The effect was explained as immediate transfer of the electron formed in the illuminated CdS part of the TiO_2 part as the conduction band in TiO_2 is on a less negative potential than that of CdS. The positive hole, on the other hand, cannot move to the TiO_2 part as it would be there on a much higher positive potential than in CdS. The result of this electron transfer is an efficient primary charge separation. The TiO_2–CdS sandwich thus acts as a small diode of almost molecular dimensions or like an n–p junction. Similar effects have been found with sandwich structures of Cd_3P_2 and ZnO.[253] Cadmium phosphide can be made with different band gaps by varying the particle size.

Quenching of the fluorescence of cadmium phosphide by ZnO was more efficient the larger the band gap of the Cd_3P_2 part.

A phenomenon quite different from the ones just described was observed in the case of CdS–Ag_2S[36] and AgI–Ag_2S[37,225] structures. Such structures are formed upon the addition of silver ions to a CdS sol or H_2S to an AgI sol, respectively. In both cases a strong red fluorescence arises which moves into the infra-red region with increasing size of the Ag_2S part. This fluorescence is quenched by a small amount of Ag_2S. The new red fluorescence peaks at 850 nm (1.45 eV photon energy) at low Ag_2S deposits. A second maximum at 1,050 nm (1.18 eV) appears at higher Ag_2S concentrations, which shifts to longer wavelengths with increasing Ag_2S concentration, and, at almost complete conversion of AgI into Ag_2S, a weak fluorescence at 1,250 nm (0.99 eV) remains that corresponds to beh band-gap energy of non-quantitized Ag_2S.

The explanation of these findings seems as follows. Small silver sulfide deposits (a) are strongly quantitized, the conduction band lying at more negative potential than that of AgI. The hole generated in illuminated AgI moves to the Ag_2S part at the interface, and the 850 nm

emission is brought about by the recombination of the electron in the conduction band of AgI with this hole in Ag_2S. When the Ag_2S deposit is sufficiently large (b), its conduction band is at a less negative potential and the electron can also be transferred from AgI to Ag_2S. The recombination occurs now in the Ag_2S part, the emitted light having longer and longer wavelengths as the band gap of Ag_2S becomes smaller with increasing size of this part of the sandwich.

4. PROPERTIES

If the atomic structure of nanocrystalline materials differs from the structures of glasses and crystals, the structure-dependent properties of nanocrystalline materials are expected to be different from the properties of the chemically identical substances in the glassy or crystalline state. In the following sections the existing observations on the properties of nanocrystalline materials will be summarized. Most studies have been performed for nanocrystalline substances produced by consolidation of small crystallites (Fig. 8).

4.1. *Self Diffusion*

The numerous interfaces in nanocrystalline materials provide a high density of short circuit diffusion paths. Thus, nanocrystalline materials are expected to exhibit an enhanced self diffusivity in comparison to single crystals or conventional polycrystals with the same chemical composition. This idea was confirmed by self diffusion measurements in nanocrystalline copper.[261-263] Table 5 summarizes the measured diffusivities in nanocrystalline Cu (8 nm crystal size) in comparison to lattice diffusivity and to the diffusivity in grain boundaries in Cu bicrystals. The measurements in nanocrystalline Cu were carried out by using the ^{67}Cu isotope which was diffused from the free surface into a plate shaped nanocrystalline specimen of Cu.

The measured diffusivities in the nanocrystalline Cu are about 14 to 20 orders of magnitude higher than lattice diffusion and about 2 to 4 orders of magnitude larger than grain boundary self diffusion. The enhancement in comparison to boundary diffusion may result from the following three effects. In conventional grain boundaries, rigid body relaxation[264] is known to reduce the boundary free volume. Rigid body relaxation requires translational displacements of the lattices of the two crystals forming the boundary relative to one another. Clearly, a translational displacement is possible only if the dimensions of the crystals are large in comparison to the translational displacement which is in the order of a few lattice constants or less. Hence, the small size of the crystals in nanocrystalline materials may limit the rigid body relaxation because the various boundaries surrounding every crystal require different rigid body relaxations due to their different atomic structure (cf. Fig. 6). However, these different relaxations are not possible because the small crystals cannot distort elastically by sufficient amounts to account for the different relaxations of the various boundaries

Table 5. Self Diffusivity (m^2/s) in Nanocrystalline Cu, Cu Grain Boundaries and Lattice Self Diffusion in Cu

Temperature (K)	Nanocrystalline copper (8 nm)	Grain boundary diffusion*	Lattice diffusion
393	1.7×10^{-17}	2.2×10^{-19}	2×10^{-31}
353	2×10^{-18}	6.2×10^{-21}	2×10^{-34}
293	2.6×10^{-20}	4.8×10^{-24}	4×10^{-40}

*Assumed boundary width about 1 nm.

surrounding the crystal. As a consequence, boundaries contributing to an enhanced diffusivity in nanocrystalline materials may differ structurally from boundaries in conventional polycrystals. The increased diffusion rate may also originate from an enhanced diffusivity along the triple junctions between three grain boundaries. These triple junctions form a connective network along which short circuit transport may occur at higher rates than along the grain boundaries. Thirdly, in nanocrystalline materials, the impurity concentration in grain boundaries is probably lower than in boundaries of conventional polycrystals. If all impurities of a nanocrystalline material segregate to the boundaries, the concentration of impurities in the boundary cores is still less than 10% (cf. Section 3.1). Conventional polycrystals of the highest possible purity contain enough impurities to segregate more than a monolayer of impurities in every boundary. Although the actual concentration depends on temperature and the interaction energy between the boundary and the impurity atoms, grain boundary migration experiments suggest that boundaries in conventional materials contain (even at high temperatures) large amounts of solute atoms which may reduce boundary diffusivity.

If boundary diffusion is the dominant mode of self diffusion in nanocrystalline materials, the depth profile of the tracer concentration, $C(x)$, should be proportional to $\exp(-x^2/2Dt)$ where x is the depth, measured from the specimen surface, D is the boundary diffusivity and t is the time. The above relationship implies that the tracer has been diffused from a free surface into the material at constant temperature. This is the arrangement used in most diffusion experiments. Close to the free surface ($x \leqslant 10^2$ nm) all experimental data reported for nanocrystalline materials[261,262] deviate from this relationship. The reason for this deviation is not yet understood. Hence, an unambiguous evaluation of the data is difficult. The diffusivities given in Table 5 are obtained by using the $C(x)$ profiles at $x \geqslant 10^2$ nm. Impurities in the surface region as well as grain growth have been suggested to cause the deviation. The high diffusivities have been confirmed[273] by NMR measurements in nanocrystalline Cu (10 nm crystal size) utilizing the motional narrowing of the NMR lines at high temperatures. The narrowing results from the averaging of the traceless dipole interaction by the motion of the nuclei during diffusional motion.[280,282] Comparable low activation enthalpies as the ones observed in nanocrystalline materials have been reported only for fast ionic conductors and for fast diffusors in metallic alloys. Thus, nanocrystalline materials may be utilized technologically in areas where solids with high diffusivities are needed.

4.2. *Solute Diffusion*

In amorphous alloys, the non-periodic structure results in a spectrum of trapping sites which can account for the experimental data on hydrogen diffusion.[265–268] Similar effects are noticed in nanocrystalline materials. In fact, studies of the hydrogen solubility and diffusion in nanocrystalline Pd have confirmed the idea that the structure of the interfaces of such materials manifests itself in a distribution of sites of different trapping energies for hydrogen.[269–271] Figure 45 shows a comparison of the diffusion coefficient of hydrogen in nanocrystalline and single-crystalline palladium. The observed dependence of D on the hydrogen concentration may be interpreted as follows. At low hydrogen concentrations, the hydrogen atoms become trapped in the boundaries at sites of low energy. Their diffusivity is therefore rather small. By increasing the hydrogen concentration, the traps are gradually filled. If finally the diffusivity of hydrogen involves migrations between very shallow traps only because all deep traps are filled, the value of the diffusion coefficient increases compared to that found for the diffusion in a single-crystal. A further increase of the hydrogen

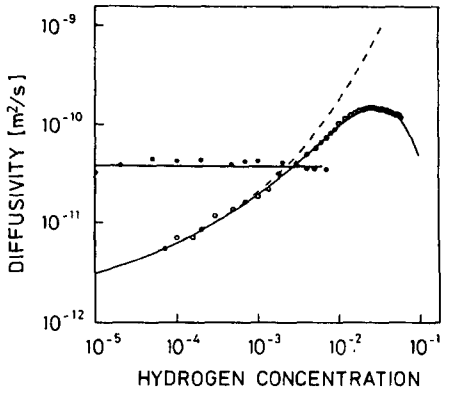

FIG. 45. Diffusion coefficients of hydrogen at 293 K as a function of hydrogen concentration in single-crystalline (●) and nanocrystalline Pd (○). The curves which are fitted to the experimental data refer to the cases with (full line) and without (broken line) hydrogen-hydrogen interaction.[270]

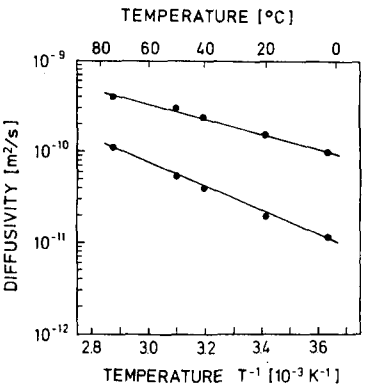

FIG. 46. Arrhenius plot of the hydrogen diffusivity in nanocrystalline Pd at different hydrogen concentrations. The upper graph represents the results at a hydrogen concentration of 3×10^{-2}, the lower one at 10^{-3}.[263]

concentration leads to an increase of the hydrogen–hydrogen interaction, and hence the diffusion of hydrogen becomes more and more impeded. This blocking of sites reduces the diffusivity if the hydrogen concentration exceeds the concentration of about 2.5×10^{-2} (Fig. 45). The experimental data on nanocrystalline materials can be fitted to curves calculated under the assumption of a gaussian distribution of site energies for hydrogen and a quasi-chemical approach for the hydrogen–hydrogen interaction.[269,270] The diffusion coefficient of hydrogen observed in nanocrystalline Pd is not only a function of its concentration but of temperature, too. Apparently, the dependence of the diffusion coefficient on the hydrogen concentration does not change its character within the temperature interval 275 K to 348 K.[272] In Fig. 46 the hydrogen diffusivity coefficients, which were found at concentrations of 3×10^{-2} or 10^{-3}, respectively, are displayed. The data may be represented by straight lines in an Arrhenius plot. The activation enthalpy of the hydrogen diffusion at the lower concentration (10^{-3}) is 0.25 eV and thus higher than the one at the higher concentration (3×10^{-2}), for which a value of 0.16 eV is obtained. The pre-exponential factors of the diffusion coefficient are 2.5×10^{-7} m^2/s at a hydrogen concentration of 3×10^{-2} and 10^{-7} m^2/s at 10^{-3}. The fact that an Arrhenius behavior has been observed in spite of a spectrum of trapping-site energies may be due to the small temperature interval investigated (73 K). Diffusion measurements over a more extended temperature regime should lead to a positive curvature of the Arrhenius curves. Therefore, the numbers given for the hydrogen diffusion represent effective values, which are likely to be valid in the investigation regime only.

For substitutional solute atoms, no trapping effects are expected. In fact, the diffusion of silver in nanocrystalline copper, was measured at various temperatures between 303 K and 373.[279] As may be seen from Fig. 47 the activation enthalpy for the diffusion is 0.39 eV (below 343 K) and 0.63 eV above 353 K in comparison to about 2 eV for lattice diffusion and about 1 eV for grain boundary diffusion of Ag in Cu. Again, the evaluation of the Cu/Ag data (Fig. 47) is not unambiguous because close to the free surface the measured concentration profile deviated from the expected $\exp(-x^2/2Dt)$ relationship as was the case for tracer diffusion in Cu. If a specimen contains a large concentration of solute atoms (as was the case in the silver-diffusion experiments), diffusion along the interfaces may cause the interfaces to migrate.[274–276] This effect has been termed diffusion-induced grain-boundary migration

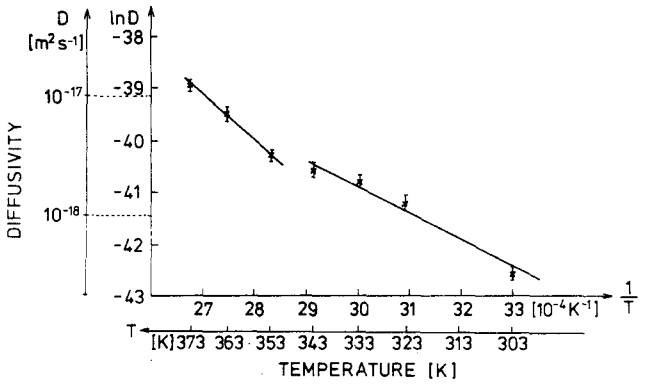

FIG. 47. Temperature dependence of the diffusion coefficients of Ag in nanocrysalline Cu (10 nm). The vertical lines indicate the error bars of the measurements. The activation enthalpies and the pre-exponentials are 0.39 ± 0.1 eV and 1×10^{-12} m^2/s, respectively, for temperatures below 343 K and 0.63 ± 0.1 eV and 3×10^{-8} m^2/s, respectively, for temperatures above 353 K.[279]

(DIGM). Considerable errors in both the magnitude and temperature dependence of the apparent diffusion coefficient may arise if DIGM is neglected.[274] In the system Cu–Ag, no DIGM has been reported so far.[275,276] Solute diffusion experiments have also been performed for the diffusion of Ni in nanocrystalline Cu in the temperature regime between 500°C and 700°C.[283] Although rapid grain growth occurred in this temperature regime, the diffusivities observed (varying between 3.8×10^{-16} cm^2 s^{-1} at 500°C and 7.6×10^{-13} cm^{2}s^{-1} at 700°C) are still several orders of magnitude larger than bulk diffusion. Due to the grain growth process, the interpretation of the data is difficult. Preliminary measurements of solute diffusivities in nanocrystalline ceramics have been performed for Hf diffusion in nanocrystalline TiO_2.[277,278] The samples were prepared by depositing a thin layer of Hf, about 2.5 nm thick, onto the free surface of a flat nanocrystalline TiO_2 specimen. The diffusion profiles were obtained by using Rutherford backscattering analysis. In order to prevent fast surface diffusion and measure grain boundary and volume diffusion, the samples were sintered prior to the Hf deposition under 1 GPa at 550°C, resulting in a density of 98% and no interconnected pores (cf. Fig. 9). The corresponding backscattering spectra are shown in Fig. 48. As expected, no diffusion was observed at temperatures below 500°C. At 650°C, the diffusion coefficient was about 4×10^{-15} cm^2/s, which is approximately the same as that of the self diffusion coefficient of Ti in single crystalline rutile. The difficulties encountered in measuring the diffusion

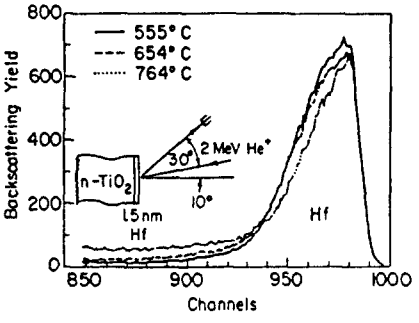

FIG. 48. Hf diffusion profiles in nanocrystalline TiO_2 measured by Rutherford backscattering for different annealing temperatures. The TiO_2 was sintered at 1 GPa at 550°C prior to Hf deposition and diffusion.[278]

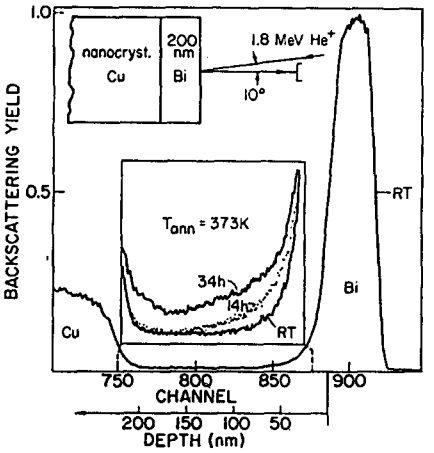

FIG. 49. He backscattering spectra for a nanocrystalline Cu sample (10 nm crystal size) with a 200 nm thick Bi film deposited onto its free surface after sputter cleaning. The spectra shown in one of the inserts indicate the Bi distribution before annealing at 373 K. The backscattering geometry used is shown in the upper inset.[286]

coefficient of nanocrystalline materials seem similar to those in glassy materials. During diffusion, the atomic arrangements in boundaries may change by analogy to the relaxation observed in glassy materials. Systematic investigations of the diffusion in nanocrystalline materials which have been pre-annealed to different extents may help to clarify this problem in a similar way as was done for glassy materials.[284,285]

4.3. *Enhanced Solute Solubility*

The solubility of a solute, A, in a solvent B, is controlled by the chemical potential μ_A of A in B. Obviously, if the atomic structure of B is changed, the chemical potential and hence the solubility of A in B may be enhanced (or reduced). In other words, the solute solubility of nanocrystalline materials is expected to be different from the one of single crystals or glasses with the same chemical composition. Five examples of this effect have been reported so far: the solubility of H in Pd, Bi in Cu, Fe in Ag and Fe in Cu. According to Fig. 36, the solubility of H in Pd (at concentrations of $\leqslant 10^{-3}$) is increased by a factor of 10 to 100 relative to a Pd single crystal.[269] A similar effect was observed[286] for Bi in Cu (Fig. 49). The solubility of Bi in crystalline Cu is less than 10^{-4} at 100°C. The vertical displacement of the curves (Fig. 49) suggests a solubility of Bi in nanocrystalline Cu of about 4%; in other words, a solubility enhancement by about 10,000 relative to crystalline Cu.[286] Structural studies of nanocrystalline alloys (Section 3.8) evidenced the formation of Ag/Fe and Cu/Fe solid solutions in the nanocrystalline state, whereas Ag/Fe and Cu/Fe polycrystals exhibit virtually no solid solubility.

Measurements of the hydrogen activity up to concentrations of 0.7 have been carried out recently.[271] The results obtained and the structural implications have been discussed in Section 3.7.4.

4.4. *Specific Heat*

The curves of the specific heat as a function of temperature measured for nanocrystalline and polycrystalline Cu or Pd as well as for a metallic glass ($Pd_{72}Si_{18}Fe_{10}$) are summarized in

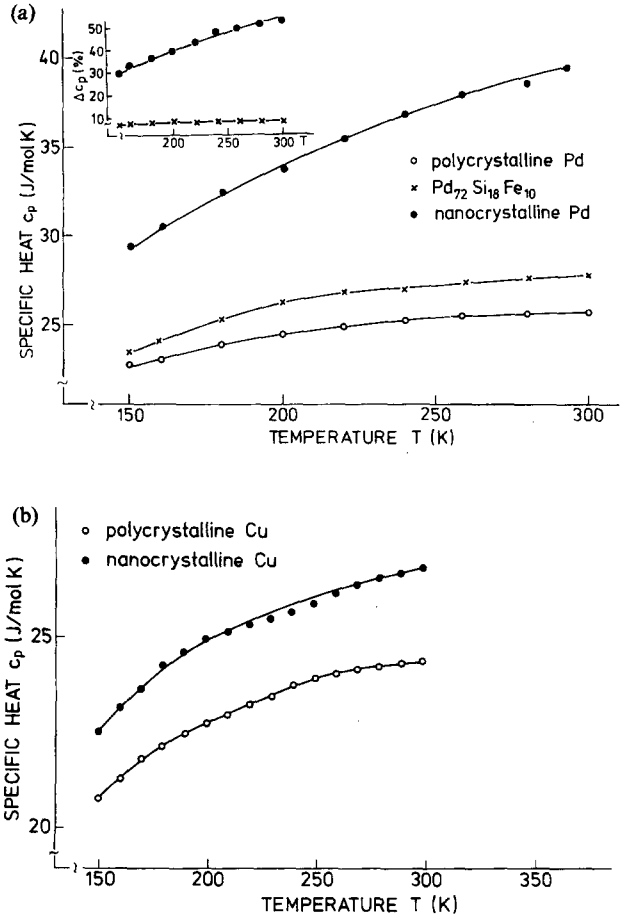

FIG. 50. (a) The specific heat (c_p) of polycrystalline Pd in comparison with nanocrystalline Pd and a $Pd_{72}Si_{18}Fe_{10}$ metallic glass. The enhancement Δc_p of the nanometer-sized crystalline Pd (●) and the metallic glass (×) relative to the polycrystalline Pd is shown in the upper left-hand corner. (b) The specific heat (c_p) of polycrystalline Cu (○) in comparison with nanocrystalline Cu (●).[287]

Fig. 50.[287] The enhancement of c_p in going from the polycrystalline to the nanocrystalline state varies between 29% and 53% for Pd in the temperature range investigated (Fig. 50a). The corresponding values for Cu are 9% and 11% (Fig. 50b). The c_p values of the polycrystalline Pd and glassy state ($Pd_{72}Si_{18}Fe_{10}$) differ by about 8% and about 50% of which originate from the different atomic structure. The residual portion is due to the deviating chemical composition. Cu and Pd are diamagnetic and paramagnetic metals, respectively. Hence, electronic and magnetic contributions to the specific heat in the temperature range between 150 and 300 K are negligible. The specific heat of nanocrystalline Cu and Pd is, thus, due to the thermally induced variation of the vibrational and configurational entropy of the materials (i.e. due to lattice vibrations, variation of equilibrium defect concentration, etc.). The deviation of the crystalline and nanocrystalline states is unlikely to result from internal surfaces because small-angle X-ray diffraction (Section 3.3.1), positron annihilation (Section 3.7.1), and hydrogen solubility measurements (Section 3.7.4) gave little evidence for a large amount of free internal surfaces, e.g. at pores. The different enhancements of c_p of Pd and Cu in the nanocrystalline state seem to be consistent with the different densities of

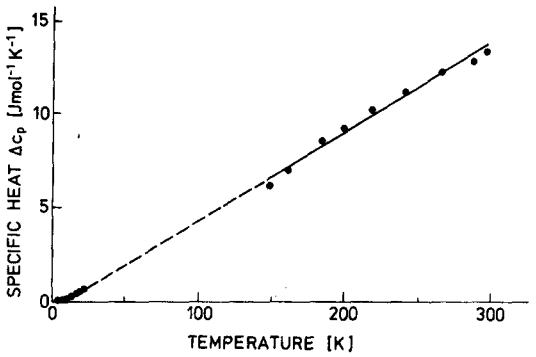

FIG. 51. Excess specific heat, Δc_p (specific heat of nanocrystalline Pd minus the specific heat of single crystalline Pd) of nanocrystalline Pd (6 nm crystal size).[290]

both substances. In fact, the lower relative density of nanocrystalline Pd in comparison to nanocrystalline Cu (produced under similar conditions) suggests a more open atomic structure of the grain boundary component in the case of Pd, and hence weaker interatomic coupling, which should enhance c_p. This argument implies that the enhancement of c_p is primarily due to the grain boundary component. If this is so, grain growth should reduce the specific heat of the nanocrystalline materials to that of polycrystals. This was, in fact, observed when the nanocrystalline Cu and Pd samples were annealed at 750 K to initiate grain growth. The grain size of the samples after annealing was 20 nm. In the case of Pd, it was also noticed that during the heat-up cycle an exothermic reaction took place at about 350 K. Subsequent cooling to 200 K revealed that the enhancement of the specific heat was reduced to about 5%. The specific heat measurements on nanocrystalline Pd have been recently expanded into the low temperature regime indicating an enhancement which depends linearly on the temperature (Fig. 51).

Measurements of the specific heat of nanocrystalline metals (Ru and AlRu) generated by high-energy ball milling (cf. Section 2.3.1) indicated similar changes as reported above.[288] Figure 52 displays the specific heat of Ru before and after 32 hr ball milling versus temperature. After 32 hr milling the specific heat increased by 15% to 20%. The specific heat increase, Δc_p, of Ru and AlRu at a constant temperature of 210 K is shown in Fig. 53 as

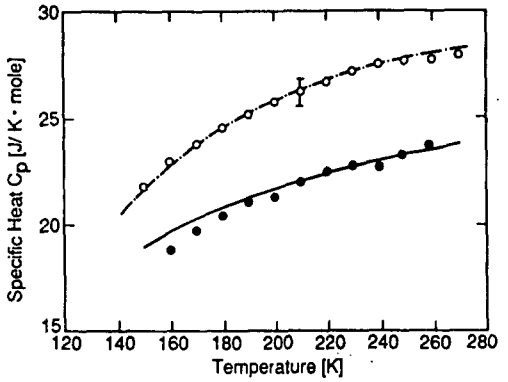

FIG. 52. Specific heat, C_p, for Ru before and after 32 hr milling as a function of temperature. The solid line shows data of a single crystal of Ru.[288]

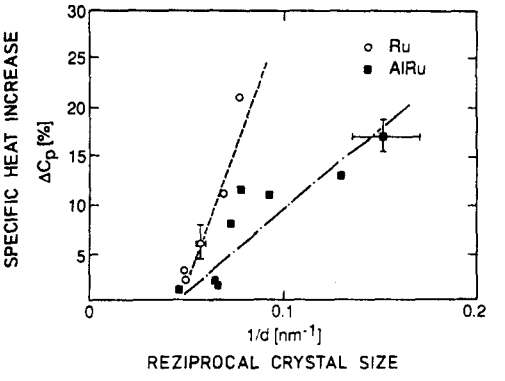

FIG. 53. Increase of the specific heat for Ru and AlRu as a function of reciprocal crystal size.[288]

a function of reciprocal crystal size. Δc_p increased almost linearly with $1/d$. Annealing the Ru and AlRu samples with the smallest crystal size, i.e. the largest increase in Δc_p, for 3 days at 1,370 K resulted in a partial reduction of Δc_p from 20% to 7% for Ru and from 15% to 5% for AlRu. Apparently, a significant portion of the observed Δc_p is in fact associated with the particle-size reduction and lattice disorder produced by the ball milling. The residual enhancement of the specific heat after long annealing times may be due to Fe impurities introduced during ball milling. Ru–Fe solid solutions probably have a lower Debye temperature than pure Ru.

4.4.1. *Low temperature measurements of the specific heat*

The specific heat, C, at very low temperatures of nanocrystalline Cu is displayed in Fig. 54 in a double-logarithmic plot of C vs temperature T for two samples with different average crystallite sizes. In normal metals (non-magnetic, non-superconducting), the specific heat at low temperatures is known to be given by $C = \gamma T + \beta T^3$, yielding for bulk Cu the solid line shown in Fig. 54. For nanocrystalline samples, C is enhanced by a factor of 5 to 10 relative to bulk Cu, with the larger enhancement occurring in samples with smaller grain sizes. An enhancement of C at temperatures above 1 K has been reported in the literature, e.g. for small vanadium crystals, and was attributed to Einstein oscillators due to weakly bound atoms at the surfaces of the particles.[384] The enhancement seen below 1 K in nanocrystalline Cu (Fig. 54) may be further analyzed by measuring the magnetic-field dependence of C. This has been done for the sample with a crystal size of 6 nm. The strong increase of C in a magnetic field $B = 6\ T$ with decreasing temperature below about 0.4 K is due to the Zeeman splitting of ^{63}Cu and ^{65}Cu nuclei, leading to a contribution $C_N = b_N T^{-2}$. As may be seen from Fig. 54, C strongly decreases in a magnetic field of 6 T below 1 K and increases above 1 K. The solid curved line in Fig. 54 is a fit of the experimental data by the following function: $C = \gamma T + \beta T^3 + b_N T^{-2} + c_s$, where γ, β, b_N and C_s are constants with the following values: $\gamma = 1.55 \cdot 10^{-5}$ J/gK^2, $\beta = 2.5 \cdot 10^{-6}$ J/gK^4 and $b_N = 1.3 \cdot 10^{-6}$ JK/g for the nanocrystalline Cu. For comparison, for bulk Cu one obtains $\gamma = 1.09 \cdot 10^{-5}$ J/gK^2, $\beta = 7.6 \cdot 10^{-7}$ J/gK^4, and $b_N = 1.8 \cdot 10^{-6}$ JK/g. C_S represents a two-level non-degenerate Schottky anomaly with an energy splitting $E = g\mu_B B$ with $B \approx 6\ T$. This

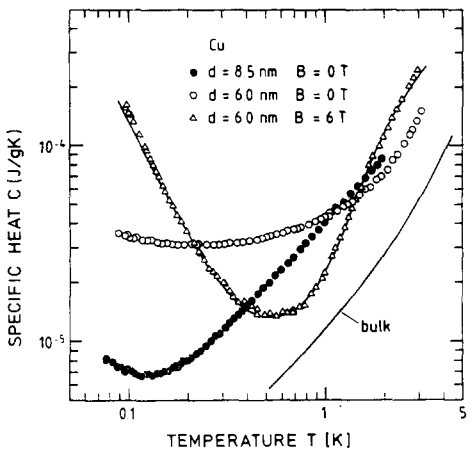

FIG. 54. Low temperature specific heat of nanocrystalline Cu for two different grain sizes (6 nm and 8.5 nm). The measurements for the 6 nm Cu were carried out without a magnetic field and at 6 T. For comparison, the solid line shows the specific heat of bulk Cu.[289]

suggests that magnetic excitations might account for the anomalously large specific heat below 1 K in $B = 0$.

The excitations are suppressed in a large magnetic field. At present, the origin of these excitations is unknown. From the magnitude of C_S, we infer that $2 \cdot 10^{-19}$ g^{-1} excitations participate, that is roughly 0.2% of the total number of atoms. Magnetic impurities at this level were not present in the samples (for $d = 6$ nm; Fe: 50 ppm, Co: 20 ppm, Ni: 71 ppm, Mn and Cr: < 10 ppm). Isolated small particles with an odd number of electrons should carry a magnetic moment of 1 μ_B.[385] With $d = 6$ nm, the number of crystallites is too small by more than one order of magnitude in order to account for the observed C_S, apart from the fact that the present nanocrystallites are not isolated. Magnetization measurements at low temperatures are underway to directly check for magnetic moments in nanocrystalline Cu which might perhaps originate from extremely weakly bonded Cu atoms at grain boundaries. It may be of interest to note that a similar anomalous behavior in the low-temperature specific heat was found in isolated Ag and Au colloidal particles of about the same size.[386]

4.5. *Entropy*

The measured excess specific heat[287] of the as-compacted nanocrystalline Pd (6 nm grain size) (Fig. 51) may be used to compute the excess entropy (ΔS) due to the grain boundaries:

$$\Delta S = \int_0^T \frac{\Delta c_p}{T} \, dT$$

where Δc_p is the difference between the specific heat of nanocrystalline and polycrystalline Pd and T is the absolute temperature.

If the Δc_p vs T curve (Fig. 51) is approximated by a straight line with the slope $A = 0.77 \times 10^{-25}$ J/at K^2, one obtains $\Delta S = AT_0$. At $T_0 = 300$ K (Fig. 51): $S = 2.3 \times 10^{-23}$ J/at K.[290] If the volume fraction of grain boundaries is assumed to be 50% and if the atoms in the centers of the crystallites are assumed to contribute little to the excess entropy, one obtains for $\Delta S = 4.6 \times 10^{-23}$ J/at K which is about $4k$, where k is Boltzmann's constant. For most metals the entropies of fusion and evaporation are about $1k$ and $10k$, respectively (Richards' and Trouton's rule). In other words, the excess entropy of the nanocrystalline Pd at ambient temperature is larger than the entropy of fusion and comparable to the entropy increase during evaporation. Attempts to measure the absolute entropy of nanocrystalline metals by means of an electrochemical method are in progress.

A theoretical interpretation of the large enthalpies and entropies of nanocrystalline materials has been proposed recently[291] on the basis of the following two assumptions. (i) The energy of grain boundaries scales with their excess volume, V.[292] (ii) A universal equation of state of a metal may be obtained by appropriate scaling.[293] Neglecting temperature effects, the binding energy E per atom may be represented as a function of a scaling parameter a only.[293]

$$E = A \cdot E(a) \tag{1}$$

with A being the cohesive energy and $E(a)$ the binding energy. The proposed scaling law is given by

$$E(a) = \exp(-a) \cdot (-1 - a - 0.05a^3) \tag{2}$$

with

$$a = (r_1 - r_2)/l \tag{3}$$

where r_1 and r_2 are the radii of the Wigner-Seitz cells at the equilibrium and expanded state. l is a length scale characteristic for a particular material leading to an equation of state of the following form:

$$P(V) = -\left(\frac{A}{4\pi r^2 l}\right) \cdot \frac{dE(a)}{da} \tag{4}$$

This equation provides a simple relationship between the energy and the free volume. In fact, it has been shown by comparison with first-principle calculations that the relationship between binding energy and free volume can be quantitatively described in terms of a simple two-parameter scaling law of a universal function and knowledge of only three input parameters is required. These input parameters are the equilibrium specific volume per atom, V_o, the equilibrium bulk modulus, B_o, and a length scale, l, as determined for most metallic elements and semiconductors according to Ref. 293. The derived universal equation of state agrees with measured compression data during shock wave consolidation. In order to compute the properties of nanocrystalline materials, this concept was extended to large expansions by the application of a negative hydrostatic pressure. This model was then utilized to describe the thermodynamic properties of atoms located in grain boundaries as function of the excess volume of these boundaries. Figure 55 shows the computed excess volume as derived from the above equation of state for Cr if a negative pressure is applied. The excess volume vs pressure dependence scales with the slope of the energy curve [eq. (1)] and reaches a minimum of about -25.8 GPa negative pressure at a critical excess volume of 0.44. At the critical excess volume, V_C, the grain boundary becomes mechanically unstable. The excess enthalpy per atom, H, is found to reach values as high as 5×10^{-19} J/at at the critical volume. This excess enthalpy corresponds to 70% of the enthalpy of sublimation and is characteristic for the high degree of disorder present in the boundaries. In fact, measurements of the energy stored in the boundaries of nanocrystalline materials[294] have indicated energies up to 30% of the heat of fusion. The boundary excess entropy (S) was estimated by using the relationship for an isothermal volume expansion $\Delta S = \gamma \cdot C_v \cdot \ln(V/V_0)$ where γ is the Grüneisen parameter, V and V_0 are the volumes of the solid before and after isothermal

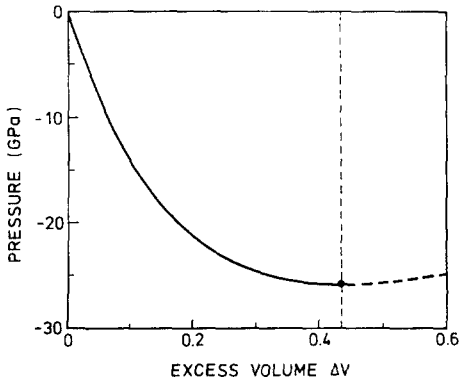

FIG. 55. Equation of state of a grain boundary in Cr. Pressure as a function of excess volume.[291]

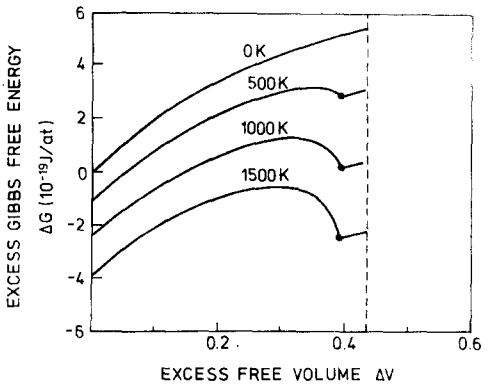

FIG. 56. The excess Gibbs free energy ΔG at different temperatures ranging from 0 K to 1,500 K (per Cr atom located in a grain boundary) as a function of the excess free volume, ΔV. This curve suggests that the grain boundaries can be entropy-stabilized at elevated temperatures for excess volumes close to a critical excess volume indicated by a broken vertical line.[291]

expansion, and C_v is the specific heat at constant volume. γ was computed from the equation of state [eq. (4)] by using the Slater approximation.[295]

From ΔH and ΔS, the excess Gibbs Free Energy, ΔG per Cr atom located in the grain boundaries was computed for different temperatures ranging from 0 to 1,500 K (Fig. 56). It was found that grain boundaries at elevated temperatures with excess volume close to ΔV_c become more stable than boundaries with smaller excess volumes. The local minimum of the entropy was predicted to stabilize the grain boundaries and hence the nanocrystalline structure. The boundary energy minimum is separated from the single crystal state ($\Delta V = 0$) by an energy barrier of about 2×10^{-19} J/at (1 eV). This barrier prevents grain growth for those grains surrounded by boundaries having large excess volumes, whereas materials with grain boundaries having low excess volumes would coarsen. The thermodynamic properties may be used to explain the experimentally observed stability of certain regions in nanocrystalline metals up to temperatures close to the melting point (cf. Section 3.5).

4.6. *Thermal Expansion*

Measurements of the thermal expansion of nanocrystalline copper (8 nm crystal size) have been carried out between 110 K and 293 K, yielding $31 \times 10^{-6}\,K^{-1}$ in comparison to $16 \times 10^{-6}\,K$ for copper single crystals.[298] A similar enhancement was observed for nanocrystalline Pd if the crystal size was about 10 nm. Recently, these results have been questioned on the basis of dilatometric data. Obviously, further measurements are required to clarify the controversial situation. As the crystalline component of a nanocrystalline material seems to contribute insignificantly to the enhancement of the thermal expansion coefficient, the average thermal expansion of the boundary component would be about four times larger than the lattice expansion if nanocrystalline materials are assumed to exhibit an enhanced expansion. In fact, this enhancement would agree with direct measurements of the thermal expansion of grain boundaries in Cu and Au by dilatometry[296] and X-ray diffraction.[297] The thermal expansion of grain boundaries in a Cu polycrystal (17 μm grain size) was found to be about four times the lattice expansion.[296] The expansion of a 22.5° (001) twist boundary (low energy boundary) in Au (normal to the boundary plane) was (X-ray diffraction) enhanced by a factor of three.[297] In fact, the X-ray diffraction data indicate a mean square displacement of the atoms in the grain boundaries $\langle u^2 \rangle$ at 298 K of about $0.012\,A^2$ which is almost twice the bulk value ($0.007\,A^2$). The difference between both $\langle u^2 \rangle$ values leads to the conclusion, that the curvature of the effective interatomic potential is less for atoms in the boundaries than in the bulk. In passing it seems worth noting the following two aspects of this result. By varying the crystal size (volume fraction of the grain boundaries) and the chemical composition, the thermal expansion of nanocrystalline materials can be tuned to any pre-determined value between the expansion of the crystal lattice and the boundary expansion.

4.7. *Optical and Infra-Red Absorption*

Optical and infra-red absorption measurements have been performed for nanocrystalline Si films.[300] Figure 57 shows a typical dependence of the absorption coefficient on photon energy for samples deposited at different temperatures. Each curve was obtained by combining results from several samples of various thickness between a few hundred nanometers and 12 μm, deposited under the same conditions. A pronounced red shift of the absorption was noticed with increasing deposition temperature up to about 350°C. If the

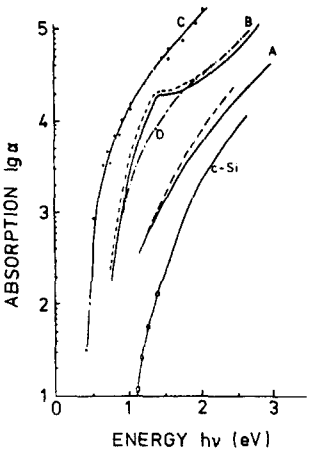

FIG. 57. Optical absorption of polycrystalline Si films deposited at various temperatures and hydrogen contents. A: 110°C, ≈12%; B: 260°C, ≈4%; C: 350°C, ≈1% D: 400°C. The hydrogen content was estimated from the IR data for each curve except at 400°C. Broken curves show the absorption after annealing in UHV at 650–800°C. The curve labeled c-Si shows the data for a Si single crystal.[300]

deposition temperature was increased to 400°C a blue shift is observed. Such a phenomenon has been found in hydrogenated amorphous Si as well and was discussed in some detail by Freeman and Paul.[301] Figure 57 indicates that all curves extrapolate approximately to $h\nu \approx 0.5$ eV for $\alpha \to 0$. This suggests that the absorption at low energies is associated with some rather well defined states in the gap which might be, for example, due to (paired) dangling bonds at the (reconstructed) interfaces between the crystallites. With increasing deposition temperature the relative amount of the crystalline component increases as well as the crystallite size. This might explain why the optical absorption with increasing deposition temperature passes through a maximum, as the total number of weak bonds (or other states associated with the interfaces) is likely to display a maximum. The results of the infra-red absorption measurements suggest the following structural conclusions. (i) The width of the individual components of the Si–H stretching modes observed indicates that they are associated with well defined sites which are unlikely to be found in an amorphous network or on internal surfaces of voids. (ii) The H content decreases with increasing crystallite size as does the number of Si atoms in the intercrystalline boundaries relative to those in the bulk. (iii) The position of the absorption peaks around 2,100 cm^{-1} agrees well with that of a broad band due to the hydrogen adsorbed at the surface of single crystalline Si.[302] The structure of nanocrystalline Si films prepared by chemical transport in a low pressure hydrogen plasma has also been studied by time-resolved photomodulation studies.[303] The transient photomodulation spectra were measured in the time domain from 10^{-7} to 10^{-2} s, spectral range from 0.25 to 1.25 eV, and temperature range from 80 to 300 K. The properties of the spectra are compatible with the presence of two phases, termed amorphous and crystalline. The amorphous phase exhibits many similarities to amorphous Si. In fact, both materials have similar photomodulation bands that exhibit three components: band tail, dangling bonds (associated with absorption), and bleaching. The temperature dependencies of the photomodulation band strengths in both materials obey an exponential law. At low temperatures the photomodulation at the band tails prevails, while at high temperatures the dangling bonds dominate. The dependence on the pump intensity is similar in both materials. Also, the correlation energies of the dangling bond defects are about the same (≈0.4–0.5 eV). There

are, however, also obvious differences between the "amorphous" phase in nanocrystalline Si and amorphous Si. The photomodulation peak in the steady-state spectra is at the same energy as in amorphous Si only from the smallest grain size. Samples with larger grain sizes deviate from this value indicating structural deviations between both materials. In nanocrystalline Si the bond tail-contribution is observable up to 150 K, while in amorphous Si it is observable up to 240 K. The demarcation energy measured in coarser-grained samples increases at about the same rate with time in nanocrystalline Si as in amorphous Si, but is deeper in the nanocrystalline material. These observations are compatible with a broader exponential distribution of states in the tail (59 meV in nanocrystalline Si and 46 meV in amorphous Si), indicating that the amorphous phase in the nanocrystalline Si is more disordered than in amorphous Si. There is, furthermore, a difference in the energies of the dangling bonds. For the transient photomodulation in amorphous Si the onset of absorption associated with dangling bonds is at 0.65 eV and the onset of bleaching at 1.1 eV; the corresponding numbers for nanocrystalline Si are around 0.5 and 0.9 eV and 0.6 and 1.0 eV. If we assume that the gap E_g is the sum of these energies, then E_g has between 1.4 eV and 1.6 eV compared to 1.75 eV in amorphous Si. The smaller gap may also be related to the larger disorder. It is not possible to directly measure E_g of the amorphous phase in nanocrystalline Si to confirm this conclusion.

4.8. *Magnetic Properties*

Measurements of the saturation magnetization (M_s) of nanocrystalline iron (6 nm crystal size) revealed a reduction of M_s by about 40% relative to the saturation magnetization of bulk α-iron.[304] For comparison, in metallic iron glasses (extrapolated to pure iron), M_s is only reduced by about 2% relative to α-Fe.[304]

A reduction of the Curie temperature (T_c) of Ni by about 40°C has been reported if the crystal size was reduced to about 70 nm.[305,306] This reduction was attributed to a reduction of T_c of the grain boundary regions. The interior of the crystals was assumed to have the same T_c as a singly crystal of Ni. The magnetic behavior of such a system was modeled by a Landau approximation suggesting a continuous reduction of T_c with decreasing grain size.

The magnetic microstructure of nanocrystalline Fe was found to differ from the one of crystalline and amorphous iron and iron alloys.[307] It is well known that the magnetic microstructure of crystalline and amorphous iron as well as iron alloys consist of ferromagnetic domains separated by domain walls. In nanocrystalline iron no domain structure was revealed by applying the Bitter technique, Kerr microscopy and/or Lorentz electron microscopy.[307] The observations reported suggest the following magnetic microstructure. Every crystallite of a nanocrystalline Fe specimen is a single ferromagnetic domain. The magnetization of neighboring crystallites is controlled by two factors: the crystal anisotropy (which tries to align the magnetization of every crystallite in one of the easy directions) and the magnetic interaction between neighboring crystallites (which tries to align the magnetization of adjacent crystals into a common direction). As the crystallites are crystallographically oriented at random, a magnetic microstructure results in which the magnetization of the crystallites is correlated over distances comparable to a few crystal diameters only. Long range correlations resulting in domain formation are prevented by the random crystal orientation and the crystal anisotropy.

Recently, a study[308] of magnetic phase transitions in nanocrystalline Er has been carried out. For nanocrystalline Er (10–70 nm grain size), the three normally observed magnetic transitions of erbium vanish and a new low-temperature transition to superparamagnetic

behavior arises. On the other hand, for nanocrystalline Er with larger grain diameters, the normal magnetic transitions re-appear but at different temperatures, while the low-temperature superparamagnetic behavior is retained.

A method of producing soft magnetic Fe-based alloys by means of nanocrystalline structures has been proposed recently.[309] Conventionally used as magnetic materials for high-frequency transformers, magnetic heads, saturable reactors, etc. are mainly ferrites having the advantage of low eddy current losses. However, since ferrites have a low saturation magnetic flux density and poor temperature characteristics, it is difficult to miniaturize magnetic cores made of ferrites for high-frequency transformers, etc. Thus, in these applications, alloys having particularly small magnetostriction are desired because they have relatively good soft magnetic properties even when internal strain remains after impregnation, molding or working, which tend to deteriorate magnetic properties thereof. As soft magnetic alloys having small magnetostriction, 6.5–wt% silicon steel, Fe–Si–Al alloys, 80–wt% Ni Permalloy, etc. are known which have saturation magnetostriction of nearly 0. Recently, as an alternative to such conventional magnetic materials, amorphous magnetic alloys having a high saturation magnetic flux density have been attracting much attention, and those having various compositions have been developed. Amorphous alloys are mainly classified into two categories: iron-base alloys and cobalt-base alloys. Fe-base amorphous alloys are advantageous in that they are less expensive than Co-base amorphous alloys, but they generally have larger core loss and lower permeability at high frequency than the Co-base amorphous alloys. On the other hand, despite the fact that the Co-base permeability varies as the time passes, this poses problems in practical use. It was therefore attempted[309] to generate nanocrystalline Fe-base alloys with specified magnetic characteristics such as core loss, time variability of core loss, low magnetostriction which keeps it from suffering from magnetic deterioration by impregnation and deformation. The alloys were generated by the addition of Cu and at least one element selected from the group consisting of Nb, W, Ta, Zr, Hf, Ti and Mo to an Fe-base alloy having an essential composition of Fe–Si–B. Initially, the alloy has a glassy structure obtained by melt-spinning. During a subsequent annealing treatment in an inert gas atmosphere (between 450°C and 700°C for 5 min up to 24 hr), the alloy crystallizes to 50% or more. The crystallites have a bcc α-Fe structure in which Si, B etc. are dissolved. The crystallites are uniformly distributed. The average diameter is 50 nm or less, preferentially in the size regime of 50 to 20 nm. When the average crystal diameter exceeds 100 nm, good soft magnetic properties are not obtained. The resulting materials exhibited core losses as low as 200 mW/cm^3 and effective permeabilities of 10^5 or more.

The magnetic properties of nanocrystalline (40 nm) yttrium iron garnets (YIG) were studied by ferromagnetic resonance. The nanocrystalline substance was produced by spray-drying followed by low temperature sintering.[382] The ferromagnetic resonance line width (ΔH) was noted to increase linearly with the logarithm of the crystal size.[299] This increase indicates that a cut-off effect for spinwaves is not the dominant mechanism controlling H. The increase of H was interpreted[299,383] in terms of the coupling between the uniform ferromagnetic resonance precession mode at $k = 0$ and the precession modes of the same frequency at $k \neq 0$. The coupling centers are proposed to be the magnetic lattice irregularities which act as scattering centers. With decreasing grain size the density of scattering centers increases and hence ΔH should increase inversely proportional to the grain size.

The phase transition from the paramagnetic to the antiferromagnetic state (Néel temperature, T_N) has been studied in nanocrystalline FeF_2 by Mössbauer spectroscopy.[394] In comparison to the narrow temperature interval of less than 2 K in FeF_2 single crystals, the nanocrystalline FeF_2 (crystal size 10 nm) exhibits a range of transformation temperatures

extending from 78 K to 66 K. In fact, the observed distribution of Néel temperatures in the nanocrystalline FeF_2 indicates that the crystallites transform at the same Néel temperature (78 K) as a bulk single crystal, whereas the T_N of the boundaries extends over a temperature regime of 12 K. This result may be understood as follows.

T_N is known to depend on the number of nearest neighbors (N) and the spacings (S) between a particular atom and its neighboring atoms. According to the EXAFS and small angle scattering experiments (of Section 3.3.1 and 3.6.2) N is reduced and S is expanded in the boundary regions in comparison to a FeF_2 single crystal. Hence the average spin/spin coupling between adjacent boundary atoms is reduced which lowers T_N. The reduction depends on the local boundary structure and thus a spectrum of Néel temperatures results. This interpretation agrees with the observed reduction of the Debye temperature from 298 K (FeF_2 single crystal) to 86 K for the nanocrystalline FeF_2.[394]

4.9. *Electrical Resistivity*

Systematic studies of the electric resistivity of nanocrystalline materials have recently been performed for nanocrystalline Cu, Pd and Fe specimens.[364–366] The crystal sizes of the various materials studied varied between 6 nm and 25 nm. The total metallic impurity content of the Pd specimens was $\leqslant 0.5$ at%. The specimens contained between 0.3 at% and 1 at% oxygen and about 1 at% C.[364] Metallographic studies by means of scanning electron microscopy revealed residual porosities between 1 and about 10% in Cu and Fe, whereas very few (<0.1%) pores were noticed in nanocrystalline Pd.[365] Figure 58 shows the electric dc-resistivity of nanocrystalline Pd specimens as a function of temperature for various grain sizes. The measured temperature coefficient of the electric resistivity of nanocrystalline Pd and Cu was found to decrease when the crystal size was reduced (Fig. 59). The observed temperature and grain size dependence of the electric resitivity as well as the temperature coefficient may be understood in terms of electron scattering inside the crystallites as well as scattering of the electron by the boundaries by analogy to the treatment of the electric dc-resistivity of thin metallic films.[367–378] The interaction of grain boundaries with conduction electrons has been treated by considering the boundaries as potential barriers of a given height and width scattering the conduction electrons. This scattering may either be described in terms of the reflection of the electrons by the boundaries or the transmission through the

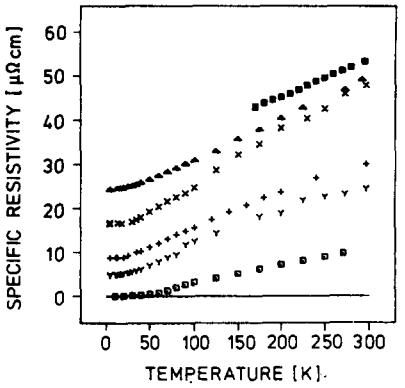

FIG. 58. Specific electric dc-resistivity of nanocrystalline Pd as a function of temperature and crystal size (■ 10 nm, ▲ 12 nm, × 13 nm, + 22 nm, ϒ 25 nm) in comparison to coarse-grained pure Pd polycrystal (□).[365]

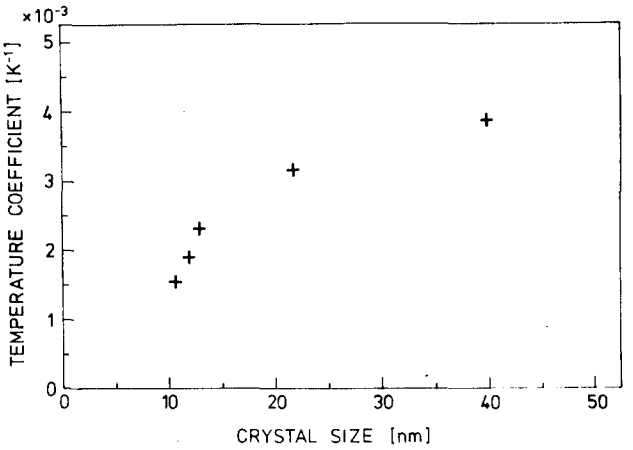

FIG. 59. Temperature coefficient of the electric dc-resistivity of nanocrystalline Pd as a function of crystal size.[365]

boundaries. The results of both treatments differ in details. However, the basic predictions are the same and may be summarized as follows. (i) If the grain boundary barrier height and/or width is increased, the electron scattering by the boundary becomes stronger. (ii) If the crystal size approached or becomes less than the electron mean free, the conductivity as well as the temperature coefficients decreases. In fact, even negative values of the temperature coefficients have been predicted.[378] On the other hand, if the grain size is large in comparison to the electron mean free path, the conductivity and the temperature coefficient due to boundary scattering are expected to approach the bulk limit. If the resistivity of nanocrystalline metals is considered in the light of these results, the following conclusions may be drawn. If the crystal size is smaller than the electron mean free path, grain boundary scattering dominates and hence the conductivity as well as the temperature coefficient is expected to decrease as was observed (Fig. 59). For grain sizes larger than the electron mean free path, the conductivity and the temperature coefficient deviate considerably from the corresponding bulk values. In other words, electron scattering by volume scattering effects inside of the crystals occurs and becomes the dominant scattering mode suggesting a high density of point or line defects in the crystallites. The residual impurity content or porosity cannot account for the deviation. The observed temperature dependency of the resistivity was utilized[364] to deduce the Debye temperature of the nanocrystalline material. The Debye temperature of nanocrystalline Pd was found to be reduced by about 100 K relative to a single crystal of Pd.

Studies of the transversal magnetoresistance[364] indicated a parabolic resistivity increase in the magnetic field. This effect may be understood if it is assumed that the grain boundaries contribute little to the magnetoresistance due to their high resistivity and hence strong electron scattering. In other words, it is the crystalline component of the material which controls the magnetoresistance and hence a similar field dependence is expected for a nanocrystalline material and a single crystal. This was indeed the case.

Crystal size effects in piezoelectric materials were studied by Multani.[379,380] PZT was found to exhibit an enhanced decrement of the piezoelectric tensor value d_{33} when the grain size was reduced. In fact, for a grain size of about 40 nm, d_{33} was as high as 300 μ C cm^{-2}.[379] The increase was interpreted in terms of the cut-off of long wave length modes due to the small crystal size. In fact, this concept has been successfully tested for small isolated PZT

crystals.[269] The significance of the high density of grain boundaries in nanocrystalline materials as pinning centers for ferroelectric domain walls has been deduced[381] from the observed enhancement of energy loss of fast electrons traversing through a ferroelectric medium ($BaTiO_3$) when heated through the phase transition temperature. The energy loss was explained in terms of the domain switching time which becomes close to the electron transit time when the temperature approaches the critical value.[381]

4.10. *Mechanical Properties*

4.10.1. *Elastic properties*

The elastic constants of nanocrystalline materials were measured[312,360] by the following four independent methods.[315,360]

(i) Elastic bending of a thin, plate shaped specimen supported at both ends and loaded with a constant force in the middle. The amount of bending was measured inductively with an accuracy of $\pm 2\,\mu$m. The accuracy of the elastic modulus deduced from these measurements was $\pm 4\%$.

(ii) Measurements of the propagation velocity of a longitudinal or transversal sound wave (frequency 10 and 50 MHz) through nanocrystalline specimens. From the measured sound velocity (accuracy 2%), the shear and the Young's moduli were computed by means of the standard equations assuming that the material is free of porosity. In fact, if a portion of the lower density of nanocrystalline materials would originate from macroscopic porosity, the elastic constants computed from the measured velocities of sound could be up to 5% larger than the values listed in Table 6.

(iii) In transparent specimens the sound velocity was determined by Brillouin scattering using laser light with $\gamma = 358$ nm and a 90° diffraction geometry.

(iv) The free decay of torsional oscillations in a torsion pendulum at 1 to 5 Hz.[360]

The elastic constants of the metallic nanocrystalline materials were found to be reduced by 30% or less whereas ionic crystals showed a reduction of more than 50% (Table 6).

These results were interpreted as follows. Due to the free volume of a grain boundary, the average interatomic spacings in the boundary regions are increased relative to the perfect lattice. If the interatomic potential in grain boundaries is assumed to be the same as in the perfect lattice, the elastic constants (averaged over all components) of a nanocrystalline material are expected to be reduced in comparison to the crystalline state due to the reduced elastic moduli of the boundaries. In fact, a further reduction of the modulus may result from the change of the interatomic potential between boundary atoms in comparison to the crystal lattice. Such a change was suggested on the basis of X-ray diffraction data[297] (cf. also Section 4.5).

Table 6. Elastic Properties of Nanocrystalline and Conventional Materials[312,360]

Material	Crystal size (nm)	Young's modulus E (1,000 N/mm^2)	Shear modulus G (1,000 N/mm^2)
Pd	8	88 (123)*	32–35 (43)*
Mg	12	39 (41)*	15 (15)*
CaF_2		38 (111)*	19 (42)*

*The numbers in brackets indicate the values for an isotopic conventional polycrystal.

In order to test this interpretation, the grain boundaries of nanocrystalline Mg and Pd were doped with oxygen and water, by adsorbing (at 20°C) O_2 and H_2O at the free surfaces of the small Pd crystals prior to the compaction process (Fig. 8). The interior of the crystals remained unchanged because both dopants cannot penetrate into the lattice at ambient temperature. If the elastic constants of the nanocrystalline substances depend primarily on the elastic properties of the boundaries, the incorporation of O_2 and H_2O should affect the elastic constants. Indeed, the doping reduced E and G to 31,000 and 12,000 N/mm^2.

Weller *et al.*[360] measured the shear modulus and the internal friction, Q^{-1}, of nanocrystalline Pd from the free decay of torsional oscillations in the frequency (f) range 1 Hz to 5 Hz with a maximum strain of $\epsilon < 10^{-5}$ in an inverted torsion pendulum between 4 K and 650 K. The internal friction was determined from the logarithmic decrement ν by $Q^{-1} = \nu/\pi$. The absolute value of the shear modulus $G \propto f^2$ was derived by a comparison of the oscillation frequencies of the nanocrystalline and a well annealed coarse-grained Pd specimen, taking the shear modulus of the latter from the literature. In order to measure the temperature variation of G and Q^{-1} either linear heating or a step-wise heating program with measurements at constant temperature were performed. The value of G at ambient temperature (35 GPa) agreed with the data obtained by the other methods (Table 6). The observed temperature variation of G during heating was interpreted in terms of the annealing out of interfacial defects. The activation enthalpy of this process was found to be 0.72 ± 0.05 eV. This result seems comparable to the activation enthalpies obtained for self and solute diffusion in nanocrystalline materials (Sections 4.1 and 4.2). It may be noticed that 0.72 eV is about half the activation enthalpy of grain boundary diffusion in Pd. The theoretical interpretation of the reduction of the Young's modulus in terms of the reduced atomic density in the grain boundary region agrees with X-ray diffraction experiments on boundaries in thin Au bicrystals.[297] The variation of the intensity of the X-ray diffraction spots of a 22.5° (001) twist boundary as a function of temperature (between 100 K and 275 K) suggests an enhancement of the mean square displacement $\langle u^2 \rangle$ of the boundary region relative to the one of the lattice by almost 50%. Since the Young's modulus is proportional to $\langle u^2 \rangle^{-1}$ the elastic modulus of the 22.5° (001) twist boundary was suggested to be about 66% of the bulk value, i.e. 5.3×10^{10} Pa under the assumption that all other contributions are to the boundary modulus equal to their bulk counterparts. The reduction agrees roughly with the data summarized in Table 6. Recently, three theoretical attempts have been made to understand the elastic constant of nanocrystalline materials. Fecht[291] computed the elastic constants in terms of the excess free volume of the grain boundaries (Fig. 55). The excess free volume of the boundaries is argued to reduce the average interaction forces between the atoms in the boundary region. This estimated modus reduction based on the assumptions is, however, more than an order of magnitude larger than the experimental observations (Table 6). In the second approach,[314] the elastic constants were investigated by means of a computer simulation method, the elastic constants in what was called a "grain-boundary superlattice". Such a (somewhat hypothetical) material consists of a periodic arrangement of thin slabs A and A′ of equal thickness, λ, of the same material. The two crystal slabs were rotated with respect to one another about the axis normal to the slab by a certain angle, θ. The computations were performed for a $\Sigma 5$(001)-twist boundary ($\theta = 36.7°$ rotation, about a common (001) axis of A and A′) in Cu. By computing the elastic response of this system the elastic modulus of the (001)-twist boundary was deduced. An embedded-atom method (EAM) potential[315] as well as a Lennard–Jones (LJ) potential for Cu[316] have been applied. Both potentials yield an increase in the Young's modulus (Y) and a corresponding decrease of the shear modulus (G) as λ becomes smaller. For example, if the slabs A and A′ have

a thickness of ten unit cells, Y is increased by about 20% and G is reduced by nearly the same amount. The physical reasons for these changes are as follows. Due to the destruction of the perfect-crystal planar stacking at the interface, atoms which were originally separated by perfect-crystal distances have been pushed together more closely. Essentially as a consequence of Pauli's principle, the bicrystal expands locally for all but very special geometries. However, in spite of the subsequent increase in the average interatomic distances a significant fraction of atoms is found at separations much shorter (up to about 10%) than in the perfect crystal. Within a given shell, distances shorter than the related ideal-crystal value are expected to strengthen the elastic constants whereas expanded distances result in their softening. Due to the anharmonicity of the interatomic potential, shortened distances are weighted more heavily than the expanded ones and therefore the elastic modulus of a boundary may be enhanced although the average atomic density is reduced. The effect is less pronounced for the EAM than for the LJ potential. Recently, Adams *et al.*[363] have performed similar computations. In fact, the elastic constants of a $\Sigma5(001)$-twist boundary in Cu were calculated using the EAM. In order to obtain the biaxial Young's modulus, a small tensile stress (0.05%) was applied to the system (two crystals and a boundary) perpendicular to the boundary plane. The atomic positions were then adjusted to minimize the total energy. The modulus of the two crystal lattices were found to be almost unaffected by the presence of the boundary unless a region of 1 nm on both sides of the boundary is considered. However, in this boundary region the Young's modulus was found to be enhanced from about 0.7×10^{12} erg/cm^2 to about 1.05×10^{12} erg/cm^2. This enhancement of the Young's modulus seems to result from the volume expansion in the boundary (computed to be about 15%). On the other hand, this volume expansion was found to decrease the shear modulus of the boundary region from about 0.75×10^{12} erg/cm^3 to almost zero.

4.10.2. *Internal friction*

The internal friction Q^{-1} (Fig. 60) was measured in nanocrystalline Pd below 300 K and was found to be about 2 to 3 times smaller than in well annealed coarse-grained Pd.[360] In the as-prepared specimen, small internal friction peaks were observed at 120 K, 220 K, and 400 K which annealed out after heating the specimen once to 640 K. Above 300 K

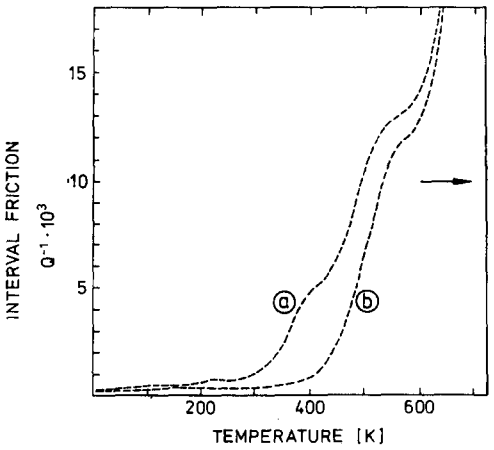

FIG. 60. Temperature variation of the internal friction Q^{-1} of nanocrystalline Pd with a heating rate of 150 K/hr,[360] (a) after 5 GPa compation at 295 K and (b) in a second run after heating to 640 K.

the internal friction increases steeply and shifts toward higher temperatures after annealing (Fig. 60). These internal friction phenomena may be interpreted in terms of viscous sliding of interfacial boundaries.[361,362] Alternatively they may, however, also be due to some kind of dislocation movement because in this temperature regime considerable internal friction is observed in well annealed coarse-grainted Pd, too. The general increase of Q^{-1} above 300 K as well as the shoulder at 520 K, are shifted to higher temperatures with increasing measuring frequency. This indicates thermal activation of the interfacial loss processes. The maximum at 520 K may be due to a particular atomic re-ordering process in the interfaces which is mechanically reversible under the alternating external stress. From the present results, an activation energy of 1.3 eV is estimated for this process assuming a pre-exponential factor of $10^{13}s^{-1}$. However, the temperature shift of the "520 K-process" with frequency variation is smaller than predicted by these activation parameters.

4.10.3. *Hardness and fracture*

The synthesis of a nanocrystalline ceramic (TiO_2 rutile) has been carried out[317,318] by producing small titanium crystals and then oxidizing them to TiO_2 prior to compaction (cf. Section 2.1.2). The nanocrystalline compacts, which are well bonded on consolidation even at room temperature, densify rapidly above 770 K (Fig. 9) with only a small increase in grain size, leading to hardness values similar to those of sintered coarser-grained commercial TiO_2, but at temperatures some 600 K lower. The Vickers microhardness of such specimens measured at ambient temperature is shown in Fig. 61 as a function of sintering temperature for three different TiO_2 (rutile) samples, the nanocrystalline sample with 12 nm initial average grain size was compacted at 1.4 GPa. The two samples with 1.3 μm initial grain size were compacted at 1.4 GPa and 0.1 GPa.[278,319] The latter sample, prepared essentially in accord with standard ceramic processing methods, was the only one of these three which was sintered with the aid of polyvinylalcohol. Obviously, the hardness of the nanocrystalline sample is about two or more times the hardness of the two other samples due to the faster sintering. The enhanced hardness of the 1.3 μm sample consolidated at 0.1 GPa above

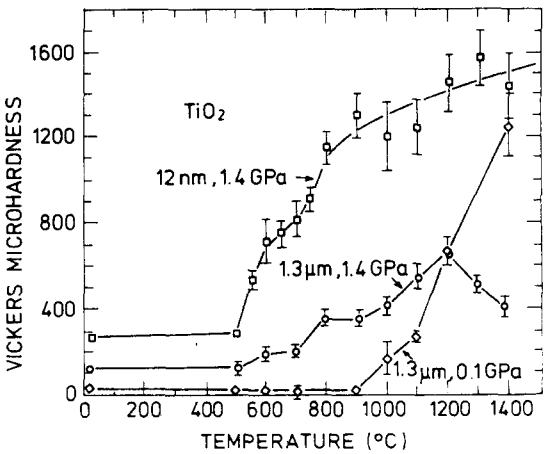

FIG. 61. Vickers microhardness in kp/mm^2 to TiO_2 (rutile) measured at room temperature as a function of one-half hour sintering at successively increased temperatures. Results for a nanocrystalline sample (squares) with an initial average grain size of 12 nm compacted at 1.4 GPa are compared with those for coarser-grained compacts with 1.3 μm initial average grain size sintered at 0.1 GPa with (diamonds) and at 1.4 GPa without (circles) the aid of polyvinyl alcohol from commercial powder.[319]

Table 7. Vickers Hardness, H, and Fracture Toughness, K_{IC}, of Nanocrystalline TiO_2[278,319]

Temperature (°C)	as prepared	600	800	1000
H (Vickers)	210	190	630	925
K_{IC} (MPa$\sqrt{m}$)	0.8	1.0	2.8	2.8
Porosity (%)	25	20	10	5

1,200°C is due to the sintering aid. For reference, the Vickers microhardness of a single crystal of TiO_2 measured under identical conditions is $1{,}036 \pm 66$ kgf/mm^2. Fracture toughness studies on these samples, made by measuring the crack lengths emanating from microindentations at higher loads, appear to confirm the similar or better mechanical properties of the TiO_2 in comparison with the coarser-grained material and single crystal TiO_2 (rutile) as well. Table 7 shows that both hardness and toughness increase with increasing sintering temperature (decreasing porosity). The values of hardness and fracture toughness after sintering at about 800–900°C are typical of well sintered bulk ceramics, indicating that good mechanical properties can be achieved in nanocrystalline TiO_2 after low temperature sintering. Usually, hardening and fracture toughness do not scale; hardening treatments tend to make materials more brittle with reduced fracture toughness. In the present case, however, the hardening and toughening result from the elimination of porosity which increases the overall strength of the material.

The results of these investigations indicate that nanocrystalline compacts, although already rather well bonded on compaction at room temperature, densify rapidly above 500°C, with only a small increase in grain size (cf. Fig. 9). The hardness and K_{IC} values obtained are comparable to or greater than those of single-crystal TiO_2 or coarser-grained compacts, but at temperatures some 400 to 600°C lower than conventional sintering temperatures and without the need for sintering aids.

A fractographic study[320] of nanocrystalline TiO_2, crystal size 12 nm (formed by post oxidation of small Ti crystals), indicated some remarkable differences between nanocrystalline and conventional TiO_2 ceramics. The sintering temperature for completely transgranular fracture of the nanocrystalline samples was about 1,100°C, or 200°C lower than that of the commercial coarser-grained material. For samples sintered at the same temperature, the voids in the commercial material are larger and more numerous than those in the nanocrystalline material. The microhardness of the nanocrystalline samples (Fig. 61) may, at least in part, be attributed by the different void morphology. The fracture mode observed indicates that the oxidation process as well as the particle collection and compacting procedures play a crucial role. In other words, by performing these steps under well-controlled conditions, the material properties may be improved. Some of the observations reported in Section 4.10.5 are closely related to the hardness and fracture of nanocrystalline materials.

4.10.4. *Low-temperature ductility of nanocrystalline ceramics*

It has been observed that conventionally brittle ceramics become ductile, permitting large (e.g. 100%) plastic deformations at low temperature (e.g. 293 K), if a ceramic material is generated in the nanocrystalline form.[318] The ductility may to some extent originate from the diffusional flow of atoms along the intercrystalline interfaces. The deformation rate $\dot{\epsilon}$ of diffusional creep (Coble creep) by interfacial diffusion is given by

$$\dot{\epsilon} = \frac{\sigma \Omega B \delta D_b}{d^3 kT}. \tag{5}$$

Here σ is the tensile stress, Ω the atomic volume, d the average crystal size, B a numerical constant, D_b the boundary diffusivity, k the Boltzmann constant, T the temperature and δ is the thickness of the boundaries. Nanocrystalline ceramics are expected to exhibit a diffusional creep rate which is enhanced relative to conventional ceramics by a factor of about 10^{11} due to the reduction of d (from 10 μm in conventional polycrystals to 10 nm) and the enhancement of the boundary diffusivity (cf. Sections 4.1 and 4.2). Figures 62a and b show the plastic deformation of nanocrystalline CaF_2 at 353 K which results in sinusoidal bending and plastic flow into a filamentary form. The space on the right side of the nanocrystalline CaF_2 specimen in Fig. 62a is initially empty and closes up during compression in the direction indicated by the arrows. Plastic deformation of nanocrystalline TiO_2 by indenting (with a diamond indenter) at ambient temperature is presented in Fig. 62c. Indentation of a conventional TiO_2 polycrystal under the same conditions as in Fig. 62c resulted in multiple cracking (Fig. 62e). If the deformation rate is larger than the creep rate of the

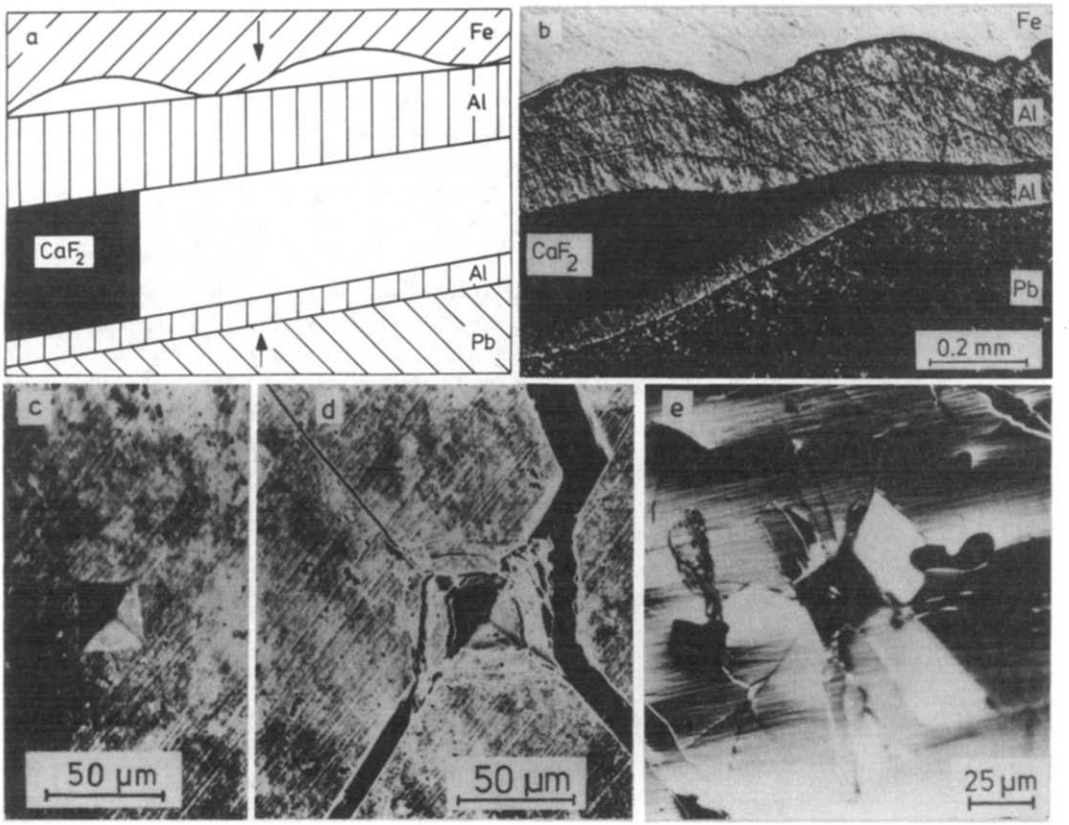

FIG. 62. Illustration of the mechanical properties of nanocrystalline materials. (a) Schematic drawing indicating the deformation procedure applied. (b) Plastic deformation of nanocrystalline CaF_2 by an arrangement as shown in (a). The deformation was carried out at 353 K and the deformation time was about 1 s. (c) Indentation of nanocrystalline TiO_2 at 293 K (load 2 N, deformation time 10 s). The hardness of the material (deduced from the size of the indent) was 250 HV. (d) Brittle behavior of nanocrystalline TiO_2 (293 K, load 2 N). The indentation was generated by reducing the loading time from 10 s (c) to 1 s. (e) Indentation of a conventional TiO_2 polycrystal under conditions similar to those in (c) (293 K, load 5 N). The hardness deduced was about 800 HV. The different brightness of the fractured areas results from tilting of these areas relative to incident light.[318]

nanocrystalline ceramic, the material should exhibit a ductile–brittle transition, as was indeed observed (Fig. 62d).

The observed plasticity of the nanocrystalline ceramic does not seem to be related to residual porosity, as has been proposed. In fact, the plastic flow of a nanocrystalline CaF_2 specimen into the transparent, filamentary form (Figs 62a and b) would be hard to understand in terms of residual porosity. Furthermore, notched specimens of nanocrystalline TiO_2 have been tested in bending[318] and exhibited plastic deformation without any crack growth. Notched specimens of brittle porous materials fracture without plastic deformation.

The possibility to utilize the plasticity of nanocrystalline ceramics for net shape forming processes has been demonstrated recently at low temperatures where little or no grain growth occurs.[387] If the plastic deformation is performed at temperatures of about 50% at the absolute melting point (e.g. for TiO_2 at about 800°C), total strains as high as 0.6 were obtained in a period of about 15 hr.[388] Figure 63 shows a nanocrystalline TiO_2 sample before and after compression for 15 hr at 810°C. Due to the high temperature, the grain size increased from about 50 nm to approximately 1 μm. The grains were noticed to remain equiaxed and with the exception of a few residual pores at grain triple junctions no porosity was detected. Strain rates as high as $8 \cdot 10^{-5}\,s^{-1}$ were observed at true stresses of 52 MPa. These rates are quite sufficient for technological applications. The increasing grain size during deformation was noted to reduce the strain rate. However, this effect does not seem to pose a basic problem, because doping of nanocrystalline ceramics (e.g. TiO_2 by Y or Al) has been demonstrated to reduce grain growth dramatically. The available data do not yet permit to specify the mechanisms involved in the low temperature plasticity of nanocrystalline ceramics.

Grain boundary sliding, grain rotation and grain shape accommodation by diffusional processes seem to play a crucial role, i.e. processes which are typical for superplasticity.[389] In fact, superplastic flow in ceramics has been reported previously, however, the temperatures were considerably higher and technologically more difficult to achieve. Creep with high strains

FIG. 63. Nanocrystalline TiO_2-sample before and after compression at 810°C for 15 hr with a stress of 40 MPa. The initial crystal size was about 40 nm.[388]

was reported in Al_2O_3 at 1,750–1,950°C,[390] Al_2O_3 doped with Cr_2O_3 and Y_3O_3 at 1,500°C[391] and MgO doped Al_2O_3 at 1,420°C.[392] Only in ceramics with liquid phases at the interfaces was super-plastic flow found at lower temperatures.[393]

Ductile nanocrystalline ceramics may be used as a new type of ceramic material in their own right. However, the plasticity may also be utilized for processing by extrusion or rolling. Subsequently, the material may be fully or partially converted back into a conventional ceramic. Partial conversion (e.g. by surface annealing) results in a material which exhibits at the surface the properties (e.g. hardness and chemical resistivity) of a conventional ceramic. The interior of such a material would still be ductile. If grain growth is inhibited, the nanocrystalline morphology and properties may be maintained permanently and at temperatures up to the melting point.

This approach deviates from the conventional strategy to defeat the brittleness of ceramics by improvements in processing and composition. Macrodefect-free cement, chemically modified silicon nitrides and transformation-toughened zirconia,[322,323] represent successful improvements based on these two strategies. The last of these was originally proposed[324] with the provocative title "Ceramic steel?", because doped zirconia, like high-tensile steel, depends on a partial phase transformation to temper strength with shock resistance: an advancing crack triggers a local transformation which hinders further propagation of the crack. None of these improvements has gone far enough. Jack[321] described the technological, economic and organizational problems, that dimmed the promise of silicon nitride, which "has now been the ceramic of the decade for three decades". The ceramic engine, outside Japan at least, still seems a long way from practical realization. Obviously, there is still a scope for new approaches.[325]

4.10.5. *Plastic deformation of nanocrystalline metals*

The plastic deformation of nanocrystalline metals has been studied[326] for Ni with a grain size of about 70 nm. The stress–strain curves and the positron lifetime spectra were measured simultaneously in order to obtain information about the type of defects controlling the deformation process. The stress–strain curve (Fig. 64a) differs from the one of polycrystalline Ni. If the load was removed, a reversible strain recovery of about 3% was noticed (Fig. 64) irrespective of the number of loading cycles. Practically no work hardening occurs during deformation contrary to polycrystals or single crystals of Ni (Fig. 64b). Simultaneous measurements by positron annihilation revealed a high concentration of vacancy-like defects (Fig. 65). If the stress was 1,100 MPa or more, a new component ($\tau_2 \approx 510$ ps) in the positron lifetime spectrum was noticed. This component was associated with the formation of vacancy clusters. In terms of these results, the deformation process was modeled[327,328] as follows. At small stresses ($\leqslant$1,100 MPa), grain boundary sliding is the dominant deformation mode resulting in the emission of vacancies due to climb of grain boundary dislocations. At high stresses, these vacancies condense in the form of clusters. Aggregates of such clusters form microcracks which finally provide the nuclei for the brittle fracture of the material. Therefore, the plasticity and strength of nanocrystalline materials were suggested to be determined primarily by the boundaries and their physicochemical features and not by the microstructure (e.g. the types of defects) in the grains as in polycrystalline materials. The stress necessary to initiate plastic deformation in nanocrystalline and polycrystalline Pd and Cu as a function of grain size has been studied by Choksi *et al.*[329] in the grain size regime from 25 μm to 6 nm. The question of interest was whether or not the yield stress required to initiate plastic flow is correctly predicted by the Hall–Petch relationship[330,331] in the entire range of grain sizes. The results obtained suggest a deviation from this relationship below

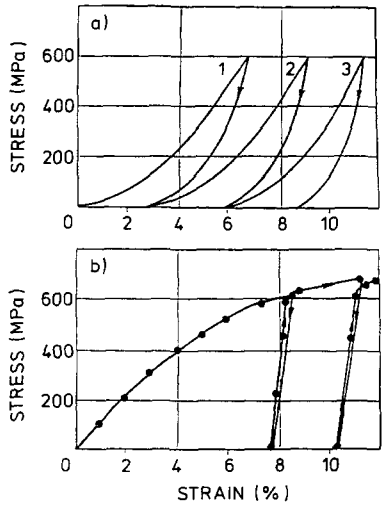

FIG. 64. Stress–strain curve of (a) nanocrystalline Ni (70 nm crystal size) and (b) polycrystalline Ni (2 μm crystal size).[326]

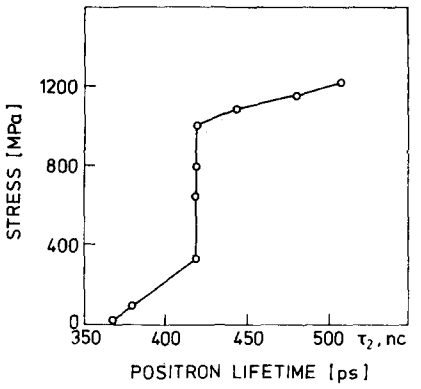

FIG. 65. Positron lifetime in nanocrystalline Ni (70 nm) as a function of the (compression) stress. The material is the same as in Fig. 64.[326] The deformation corresponds to the section 1 of the stress–strain curve in Fig. 64a.

a critical grain size, d^*. In fact, for grain sizes $d > d^*$ the yield stress increased (Fig. 66a) inversely proportional to $d^{1/2}$ as was predicted by the Hall–Petch relationship. However, for $d < d^*$ the stress necessary to initiate plastic flow becomes smaller as the grain size is reduced (Fig. 66b). In other words, reducing the grain size hardens the material for $d > d^*$ and softens it in the size regime $d < d^*$. This effect was interpreted in terms of grain boundary sliding and diffusional creep by analogy to the plasticity observed in nanocrystalline ceramics[318] discussed in the previous section.

Nanocrystalline iron whiskers (5–30 nm crystal size) produced by a chemical vapor deposition technique,[332] show extaordinary strength up to 8 GPa.[333] The grain boundaries between neighboring α-iron crystals and the phase boundaries between the α-iron and the precipitates seem to be several interatomic spacings wide and seem to contain mixed metallic and covalent bonding.

4.11. *Kinetic Effects*

The observation of phase transitions altered by the presence of a high density of grain boundaries has been reported for several alloy systems with and without plastic deformation. A nanocrystalline mixture of Co and Te crystals (average crystal size 50 nm) subjected to plastic deformation was noticed[334] to result in the formation of the $CoTe_2$ phase in a temperature regime where the diffusivity is negligible. The observed phase transition was attributed to a high supersaturation ($\geqslant 10^{-4}$) of vacancies. Grain boundary migration was suggested to be the mechanism of vacancy formation.[335–337] Nanocrystalline α-Fe (average crystal size 100 nm), deformed by rolling at pressures of about 2,000 MPa (at ambient temperature), exhibited a polymorphic transformation from α-Fe containing 32% γ-Fe (before rolling) to α-Fe containing 8% γ-Fe (after rolling).[338]

A thin bismuth film deposited on nanocrystalline Pd was found[317] by helium backscattering to form the equilibrium intermetallic Pd_3Bi at much lower temperatures (395 K) than in evaporated thin film samples. Similarly, in nanocrystalline mixtures of Cu and Er

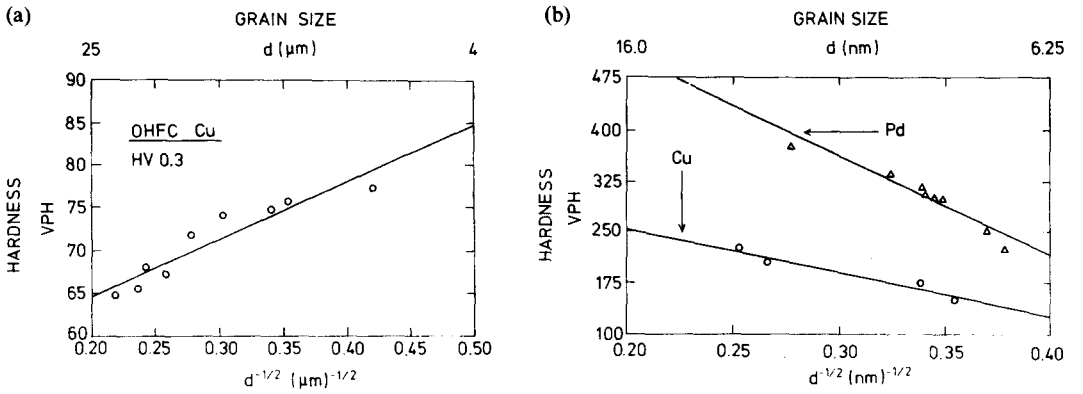

FIG. 66. Variation of hardness of Cu and Pd as a function of grain size in the regime of conventional polycrystals (a) and of nanocrystalline materials (b). It may be noticed that the hardness increases with decreasing grain size for conventional polycrystals. The contrary applies for the nanocrystalline samples.[329]

crystals, the formation of the equilibrium CuEr compound was noticed (using X-ray diffraction) after compaction. This experiment shows that the inert gas condensation method (cf. Section 2.1.2) is clean enough to subsequently react particles with one another, even when highly reactive metals like Er are being used. It also demonstrates that the intermixing of the particles of two metals in the convective helium-gas flow and on the rotating cold finger is sufficient to almost totally react the powder by compaction alone.

The formation of metastable face-centered-cubic (fcc) chromium and vanadium structures has been reported for thin sandwich layers of these materials on fcc substrates (gold, silver)[339] and is believed to result from the elastic coupling between the substrate lattice and the chromium or vanadium lattice, respectively. Similar observations on the formation of new phases have been reported by Trusov *et al.* for other alloy systems.[336,337,340] For example,[340] annealing of nanocrystalline mixtures of Cu (15 nm) and Ni (50 nm) homogenized several orders of magnitude faster than anticipated from bulk diffusivity. The rapid homogenization was interpreted to result from a high supersaturation of vacancies.

Phase transformations of the martensitic type seem to be prevented by nanocrystalline morpohologies. A comparative study by means of high and low temperature X-ray diffraction[341] of the martensitic phase transition in Fe–Ni alloys with Ni contents between 31 and 36 wt% with a crystal size of 4 nm, a coarse-grained polycrystal and isolated nanometer-sized (7 nm) crystals with the same chemical composition embedded in paraffin led to the following result. The martensitic phase transition from γ-Fe (fcc structure) to α-Fe (bcc structure) observed in the coarse-grained polycrystal dose not occur in the isolated nanometer-sized crystals as well as in the nanocrystalline material obtained by consolidation of the nanometer-sized crystals. Two reasons are conceivable for this effect. The small crystals as well as the nanocrystalline materials do not contain suitable nucleation sites for the α-phase. Alternatively, the growth of the α-phase in inhibited. Previous studies[342–345] on the nucleation of martensite in nanometer-sized crystals have given evidence to a lack of nucleation sites. Growth inhibition is conceivable in the nanocrystalline material due to constraints for the following reasons. Imagine a polycrystalline structure of γ-Fe crystals with a few nanometer diameter. If one of these crystals transforms by a martensitic shear process into an α-Fe structure, it has to be sheared elastically, plastically or by both shear

modes to maintain compatibility with the surrounding (yet untransformed γ-Fe crystals). Both, the elastic or the plastic shear require unrealistically high shear stresses. If the martensitic shear is 0.7, a simple estimate shows that the elastic shear energy to maintain compatibility of the transformed crystal with the neighboring ones would be larger than the latent heat of fusion. Similarly, plastic shear of an Fe crystal with a diameter of a few nm requires stresses close to the theoretical shear stress due to the energy of the slip steps formed at the boundaries. As adjacent crystals have different crystallographic orientations, a martensitic transformation by shearing several crystals cooperatively seems to be impossible. The stabilization of the austenitic phase by the nanocrystalline morphology may be of technological interest. The critical temperature of A15 or B1 superconductors (e.g. Nb_3Sn or V_3Si) increases if the solute concentration is enhanced. However, the enhancement is limited by the martensitic phase transition at higher Sn or Si concentrations.[358,359] This martensitic phase transition may be prevented in nanocrystalline Ni_3Sn or V_3Si alloys.

4.12. *Recrystallization*

The recrystallization of nanocrystalline metals has been investigated by several authors. Nevertheless, the understanding seems to be still fragmentary and the interpretation of the existing observations is controversial. Some of the experimental observations are reviewed in Section 3.5 on the thermal stability of nanocrystalline materials. In a series of papers[340,346,347] published in the Soviet Union, the view is advocated that a high supersaturation of vacancies is the most significant process occurring during recrystallization of nanocrystalline metals. Positron annihilation measurements were claimed[348] to evidence the vacancy supersaturation during recrystallization of nanocrystalline Ni (crystal size 15 nm). Prior to annealing the positron lifetime spectra of the nanocrystalline Ni consisted of two components (lifetimes and intensities $\tau_1 = 138 \pm 3$ psec, $I_1 = 55 \pm 2\%$ and $\tau_2 = 281 \pm 10$ psec, $I_2 = 45 \pm 2\%$). These two components were interpreted to arise from the annihilation of positrons coming from the bulk and the interfaces between the Ni crystals, respectively. After annealing the specimen for 200 min at 300°C in vacuum, the spectrum showed a sharp increase of the lifetime and intensity of the short-lived component up to $\tau_1 = 188 \pm 6\%$ psec, $I_1 = 86 \pm 3\%$. Nickel foils (99.99%) subjected to annealing and plastic deformation (40%) were observed to exhibit positron lifetimes of 134 and 183 psec, respectively. Thus, the heating to 300°C of the nanocrystalline specimens was suggested to have resulted in a defect structure (vacancy concentration) characteristic of heavily deformed Ni. Studies of the microstructure by scanning electron microscopy revealed crystal growth from 15 nm (20°C) to 150 nm (300°C) and 200 nm (500°C). The physical reason for the high vacancy supersaturation was proposed to be the athermal emission of vacancies from grain boundary dislocation during boundary migration.[349] The driving force for this process was proposed to be the reduction of the total free energy of the system due to grain growth. In fact, evidence for the emission of non-equilibrium vacancies by migration boundaries has been presented previously in conventional polycrystals.[350] This effect was rationalized in terms of growth accidents[351] which is physically similar to the climb of grain boundary dislocations. During recrystallization of nanocrystalline materials Trusov *et al.*[352–354] noticed the rate of plastic deformation to be enhanced by a factor of about 10^4 relative to materials with a grain size of $\geqslant 10^2$ μm. This enhancement was attributed to a high supersaturation of vacancies. The vacancies are proposed to be generated during recrystallization of the nanocrystalline materials.[348,355,356] The vacancies are envisioned to enhance dislocation climb processes and thus increase the rate of plastic deformation.

4.13. *Radiation Damage*

The structural changes induced by high-energy ions (He, Ne, Ar, Xe) in a nanocrystalline $Fe_{60}Cu_{40}$ alloy (8 nm grain size) were studied by resistivity measurements.[357] Irradiation with heavy ions resulted in a rapid resistivity decrease with increasing doses whereas light ions had practically no effect. This difference may be understood in terms of the atomic rearrangements induced by the cascade effects in the grain boundaries. The diameter of the cascades was for Ne, Ar and Xe about three times the crystal size of the material. Hence every cascade comprises several grains. If the initial high resistivity (about 200 $\mu\Omega$ cm) is primarily due to the low conductivity of the boundary regions, the material may be considered as a two component system consisting of highly conductive crystals embedded in a matrix of grain boundaries with low conductivity. During cascade formation, atoms in the grains as well as boundary atoms are displaced leading to a structural modification of the interfaces. If the new interfacial structure has an enhanced electric conductivity, cascade formation leads to the formation of conductive links between the grains and finally—at high cascade concentrations—approaches the percolation limit. This picture is supported by two experimental facts. In the case of He ion irradiation no cascades and very few atomic rearrangements are introduced. Hence the critical number of conductive links cannot be achieved even at high doses and no resistivity decrease will be observed. On the contrary, for heavy ions and dense displacement cascades, the critical link density will be achieved at lower doses if heavier ions were implanted. Indeed, the percolation occurred for Xe at 0.01 dpa instead of 0.02 dpa for Ar ions of comparable energy.

5. NANOGLASSES

By analogy to nanocrystalline materials, the generation of glasses called "nanoglasses" was recently proposed.[10,395,396] The production of such a glass was carried out by a similar procedure as described in Fig. 8. If the material evaporated has the ability to form a glass upon rapid cooling, the evaporation and subsequent rapid cooling process in the helium atmosphere leads to the formation of nanometer-sized glassy droplets rather than nanometer-sized crystallites. Subsequent consolidation of these droplets results in a glassy solid with enhanced free volume. The enhanced free volume originates from the mechanical shear of the droplets during compaction and the regions of contact between adjacent droplets. The contact region between two droplets differs structurally and/or chemically from the atomic structure in the centre of the droplets for the following reason (Fig. 67). The surface atoms of an isolated glassy droplet in a vacuum form a glassy (short range ordered) atomic arrangement with the atoms in the interior of the droplet so that certain interatomic spacings are preferred between the surface atoms and the atoms in the interior. If two (originally isolated) glassy droplets are brought into contact (e.g. contact region between A and B), the interatomic spacings between the surface atoms belonging originally to the two different droplets deviate from the interatomic spacings between the atoms in the interior due to the misfit between A and B. Although some relaxational motion of the atoms in the region of contact occurs, a different distribution of interatomic spacings in the interfacial regions results in comparison to a bulk glass with the same chemical composition. Similar arguments apply to the atomic structure of a region in which a glassy droplet is mechanically sheared during compaction. Due to the non-periodic structure of a glass, a region of enhanced free volume is generated as is known from the structure of shear bands in metallic glasses. In fact, by analogy to the structure of nanocrystalline materials, the atomic structure of the interfacial regions between

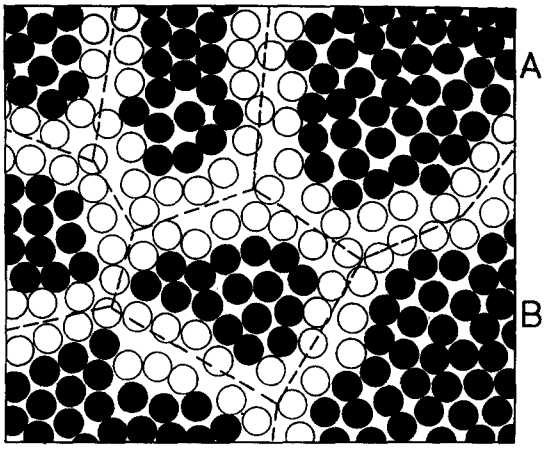

FIG. 67. Schematic cross section through a two-dimensional nanoglass. The atoms are represented by circles. The material consists of small regions in the interior of which (full circles) the interatomic spacings are similar to a bulk glass. In the interfacial region (broken lines, open circles) a broad spectrum of interatomic spacings exists.

the droplets and the regions of mechanical shear are proposed to exhibit a broad distribution of interatomic spacings (Fig. 67). This speculation agrees with recent measurements by Mössbauer spectroscopy.[396]

The observed Mössbauer spectra of a $Pd_{75}Si_{25}$ nanoglass doped with Fe and the corresponding quadrupole splitting distribution are shown in Fig. 68b, in comparison to the spectrum of a chemically identical glass prepared by melt spinning (Fig. 68a). Obviously both materials exhibit different spectra and different distributions of the quadrupole splitting. In fact, the quadrupole splitting of the nanoglass may be considered as a superposition of the following two components; one (narrow) component (solid line in Fig. 68b) which

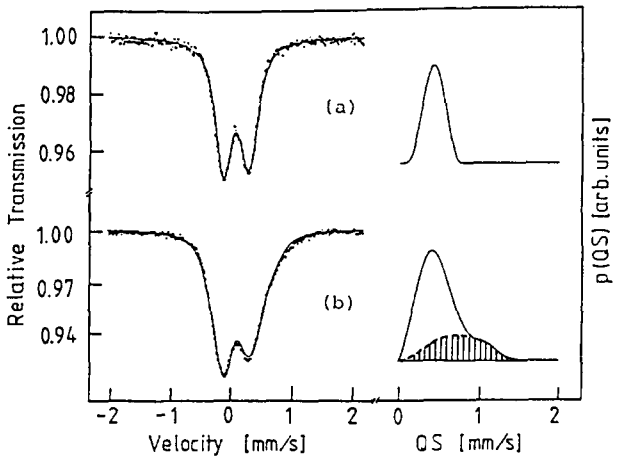

FIG. 68. (a) Mössbauer spectrum and distribution, $p(QS)$, of the quadrupole splitting (SQ) of a melt spun $Pd_{70}Fe_3Si_{27}$ metallic glass.[396] (b) Mössbauer spectrum and distribution, $p(QS)$, of the quadrupole splitting (QS) of a nanoglass with the same chemical composition as in (a). The diameter of the droplets used to generate the glass was about 4 nm.[396] The quadrupole splitting consists of two components. A narrow one (solid line) similar to the quadrupole splitting of (a) and a broad component (broken line, hatched area) which is observed in the nanoglass only.[396]

corresponds to a conventional (e.g. melt-spun) glass, and a second broad component (broken line in Fig. 68b) which is observed in the nanoglass only. This result may be understood as follows. The quadrupole splitting is known to depend on the nearest neighbor configuration only. Hence, the nanoglass consists structurally of two components. One component in which the atoms are arranged similarly to a Pd–Si-glass generated by melt spinning. In the second component, the distribution of the interatomic spacings between nearest neighbors is much wider than in the melt-spun glass as suggested by the broad distributions of the quadrupole splitting. If this broad distribution is due to the interdroplet region, the structure of the nanoglass may be manipulated in a controlled way as follows. The volume fraction of the interdroplet region decreases if the droplet size is made larger. As a consequence, by varying the diameter and/or chemical composition of the consolidated glassy droplets, the relative volume fractions of the glassy and the broad second component can be manipulated. In other words, by varying the size of the glassy droplets used for consolidation, one may be able to vary (at constant chemical composition) the atomic structure of nanoglasses continuously between the short-range ordered structure of a conventional glass and structure with a broad distribution of interatomic spacings. If the chemical composition of the surface region of an isolated glass droplet differs from the interior of the droplet (e.g. due to surface segregation effects), the interfacial regions deviate chemically as well as structurally from the center.

Although the atomic structure of nanoglasses has been discussed in similar terms as was done for nanocrystalline materials, there seems to be the following fundamental difference between both materials. As was pointed out in the first section, nanocrystalline systems preserve the low energy structure in the interior of the crystallites at the expense of the boundary regions where the misfit between adjacent crystal lattices is concentrated so that a structure far away from equilibrium (with a large free volume and a broad distribution of interatomic spacings) is formed. In the case of nanoglasses, the glassy interior of the droplets (Fig. 67) is not a low energy structure. Hence the atomic misfit of the transition region between adjacent glassy droplets (e.g. between A and B in Fig. 67) in the as-consolidated state may not remain in this region if the nanoglass is held for some time at ambient temperature. In fact, the diffusional rearrangement of individual atoms may allow the system to redistribute the misfit and free volume from the interfacial regions to other regions within the structure in order to reduce the total free energy of the systems. Hence some time after consolidation, the nanoglass may have lost its structural memory to the initial state in the sense that the free volume distribution of the as-compacted state is replaced by a new free volume distribution of lower free energy. In fact, such rearrangements have been observed in computer simulations of glassy structures into which "vacancies" or "dislocations" have been introduced by removing an atom or by local shear. In other words, nanoglasses may exhibit structural features which differ from the ones of nanocrystalline materials as well as from glasses prepared by one of the conventional methods.

Acknowledgements

The financial support by the BMFT (Contract No. 03 M 00234) and the Deutsche Forschungsgemeinschaft (G. W. Leibniz program) is gratefully acknowledged. The author appreciates the numerous helpful discussions with colleagues from various laboratories in Germany, Japan and the United States. He also would like to thank Professor P. Haasen for reading the manuscript and for suggesting several modifications.

REFERENCES

1. H. GLEITER, *Proceedings of the Second Risø International Symposium on Metallurgy and Materials Science* (edited by N. Hansen *et al.*), Roskilde, p. 15 (1981).
2. R. BIRRINGER, U. HERR and H. GLEITER, *Suppl. Trans. Japan Inst. Metals* **27,** 43 (1986).
3. X. ZHU, R. BIRRINGER, U. HERR and H. GLEITER, *Phys. Rev.* **B 35,** 9085 (1987).
4. H. GLEITER, *Proc. Ninth Int. Vac. Congress and Fifth Int. Conf. Sol. Surf.* (edited by J. L. Segovia), Asociation Espanola de Vacio Y Sus Aplicationes, Madrid, p. 397 (1983).
5. R. W. SIEGEL and H. HAHN, *Current Trends in Physics of Materials* (edited by M. Yusouff), World Scientific Publ. Co., Singapore, p. 403 (1987).
6. R. BIRRINGER and H. GLEITER, *Advances in Materials Science, Encyclopedia of Mat. Sci. and Eng.* (edited by R. W. Cahn), Pergamon Press, Oxford, p. 339 (1988).
7. H. E. SCHAEFER, R. WÜRSCHUM and R. BIRRINGER, *J. Less-Common Metals* **140,** 161 (1988).
8. C. SURYANARAYANA and F. H. FROES, *Proc. Physical Chemistry of Powder Metals Production and Processing* (edited by W. Murray and D. G. C. Robertson), TMS Publ. Warrandale P.A., 269 (1989).
9. R. BIRRINGER, *Mater. Sci. Eng.* **A 117,** 33 (1989).
10. H. GLEITER, *Europhysics News* **20,** 130 (1989).
11. J. JING, R. BIRRINGER, U. GONSER and H. GLEITER, *J. Non-cryst. Solids* **113,** 167 (1989).
12. J. WEISSMÜLLER, R. BIRRINGER and H. GLEITER, *Phys. Lett.* **A145,** 130 (1990).
13. M. J. WEINS, H. GLEITER and B. CHALMERS, *J. appl. Phys.* **42,** 2639 (1971).
14. K. L. MERKLE, J. F. REDDY, C. L. WILEY and D. J. SMITH, *Phys. Rev. Lett.* **59,** 2887 (1987).
15. H. GLEITER, *Mater. Sci. Eng.* **52,** 91 (1982).
16. M. S. MULTANI and V. K. WADHAWAN (eds), *Phase Transition Journal Section B*, Special Issue (in press).
17. R. P. ANDRES, R. S. AVERBACK, W. L. BROWN, L. E. BRUS, W. A. GODDARD, A. KALDOR, S. G. LOUIE, M. MOSCOVITS, P. S. PEERCY, S. J. RILEY, R. W. SIEGEL, F. SPAEPEN and Y. WANG, *J. Mater. Res.* **4,** 740 (1989).
18. D. W. JOHNSON, *Adv. Ceram.* **21,** 3 (1987).
19. E. MATIJEVIC, *Ultrastructure Processing of Ceramics, Glasses and Composites* (edited by L. L. Hench and D. R. Ulrich), J. Wiley, New York (1984).
20. P. VINCENCINI (ed.), *Ceramic Powders. Materials Science Monographs* **16,** Elsevier, Amsterdam (1983).
21. H. HAUSNER, *Ceramic Materials and Components for Engines* (edited by W. Bunk and H. Hausner) Dt. Keram. Gesell., p. 27 (1986).
22. H. HAUSNER, *Ber. Dt. Keram. Gesell.* **55,** 194 (1978).
23. C. HAYASHI, *Physics Today* **48,** 44 (1987).
24. C. R. VEALE, *Fine Powders Appl. Science Publ.* London, p. 5 (1972).
25. P. FAYET and L. WÖSTE, *Z. Phys.* **D3,** 177 (1986).
26. R. B. WRIGHT, J. K. BATES and D. M. GRUEN, *Inorg. Chem.* **17,** 2275 (1978).
27. D. LEOPOLD, J. Ho and W. C. LINEBERGER, *J. Chem. Phys.* **86,** 1715 (1987).
28. M. L. MANDICH, V. E. BONDYBEY and W. D. REENTS, *J. Chem. Phys.* **86,** 4245 (1987).
29. G. BENASSAYAG, J. ORLOFF and L. W. SWANSON, *J. Physique, Colloq.* **C7,** Suppl. No. 11, 389 (1986).
30. R. UYEDA, *J. Cryst. Growth* **24,** 69 (1974).
31. C. G. GRANQVIST and R. A. BUHRMAN, *J. appl. Phys.* **47,** 2200 (1976).
32. H. ABE, W. SCHULZE and B. TESCHE, *J. Chem. Phys.* **47,** 95 (1980).
33. K. SATTLER, J. MÜHLBACK and E. RECKNAGEL, *Phys. Rev. Lett.* **45,** 821 (1980).
34. R. S. BOWLES, J. J. KOLSTAD, J. M. CALO and R. P. ANDRES, *Surf. Sci.* **106,** 117 (1981).
35. E. CHOI and R. P. ANDRES, *Physics and Chemistry of Small Clusters* (edited by P. Jena, B. K. Rao and S. N. Khanna), Plenum Press, New York, p. 61 (1987).
36. R. W. SIEGEL and J. A. EASTMAN, *Mater. Res. Soc. Symp.* **132,** 3 (1989).
37. R. W. SIEGEL and H. HAHN, *Current Trends in Physics of Materials* (edited by M. Yussouff), World Scientific Publ. Co., Singapore, p. 403 (1987).
38. J. KARCH, R. BIRRINGER and H. GLEITER, *Nature* **330,** 556 (1987).
39. J. JING, Ph.D. Thesis, U. Saarbrücken, p. 8 (1989).
40. R. S. AVERBACK, H. HAHN, H. J. HÖFLER, J. L. LOGAS and T. C. SHEN, *Mater. Res. Soc. Symp.* **153,** 3 (1989).
41. A. YANAGIDA, S. YATSUYA and K. MIHAMA, *Jap. J. appl. Phys.* **26,** L 25 (1987).
42. S. IWAMA, K. HAYAKAWA and T. ARIZUMI, *J. Cryst. Growth* **66,** 189 (1984).
43. J. A. EASTMAN, *Mater. Res. Soc. Symp.* **132,** 27 (1989).
44. Z. LI, H. HAHN and R. W. SIEGEL, *Mater. Lett.* **6,** 342 (1988).
45. S. YATSUYA, T. KAMAKURA, K. YAMAUCHI and K. MIHAMA, *Jap. J. appl. Phys.* **25,** L 42 (1986).
46. H. HAHN and R. S. AVERBACK, *Appl. Phys. Lett.* (in press).
47. H. TRAPP, Ph.D. Thesis, U. Saarbrücken (1990).
48. Y. LIU, Q.-L. ZHANG, F. K. TITTEL, R. F. CURL and R. E. SMALLEY, *J. Chem. Phys.* **85,** 7434 (1986).
49. M. D. MORSE, *Chem. Rev.* **86,** 1049 (1986).
50. K. LAIHING, R. G. WHEELER, W. L. WILSON and M. A. DUNCAN, *J. Chem. Phys.* **87,** 3401 (1987).
51. E. A. ROHLFING, D. M. COX, R. PETKOVIC-LUTON and A. KALDOR, *J. Phys. Chem.* **88,** 6227 (1984).
52. K. LAIHING, P. Y. CHENG and M. A. DUNCAN, *J. Phys. Chem.* **91,** 6521 (1987).

53. G.-M. CHOW and P. R. STRUTT, *Mater. Res. Soc. Symp.* **132,** 61 (1989).
54. W. R. CANNON, S. C. DANFORTH, J. H. FLINT, J. S. HAGGERTY and R. A. MARRA, *J. Am. Ceram. Soc.* **65,** 324, 330 (1982).
55. G. W. RICE and R. L. WOODIN, *J. Am. Ceram. Soc.* **71,** C181 (1988).
56. M. CAUCHETIER, O. CROIX, M. LUCE, M. MICHON, J. PARIS and S. TISTCHENKO, *Cer. Int.* **11,** 13 (1987).
57. L. M. SHEPPARD, *Adv. Materials and Processes* **4,** 53 (1987).
58. G. W. RICE and R. L. WOODIN, *Applications of Lasers to Industrial Chemistry*, Proc. SPIE, **458** (1984).
59. R. A. FIATO, G. W. RICE and S. L. SOLED, U.S. Patents 4659681, 4668647.
60. DEGUSSA, Patent Nr. DE 762 723 (1942).
61. DEGUSSA, Frankfurt, *Tech. Bull. Pigments* **56,** 12 (1982).
62. A. T. LIU and KLEINSCHMIT, *Novel Ceramic Fabrication Processes and Applications* (edited by R. W. Davidge) Institute of Ceramics, Shelton, p. 1 (1986).
63. E. WAGNER and H. BRUNNER, *Angew. Chem.* **72,** 744 (1960).
64. M. CAREY LEA, *Am. J. Sci.* **37,** 479 (1989).
65. J. TURKEVICH, P. C. STEVENSON and J. HILLIER, *Discuss Faraday Soc.* **11,** 55 (1951).
66. R. M. WILENZICK, D. C. RUSSELL, R. H. MORRISS and S. W. MARSHALL, *J. Chem. Phys.* **47,** 533 (1967).
67. S. T. LIN, M. T. FRANKLIN and K. J. KLABUNDE, *Langmuir* **2,** 259 (1986).
68. A. E. BERKOWITZ and J. L. WALTER, *J. Mater. Res.* **2,** 277 (1987).
69. R. ROSSETTI, J. L. ELLISON, H. M. GIBSON and L. E. BRUS, *J. Chem. Phys.* **80,** 4464 (1984).
70. M. MEYER, C. WALBERG, K. KURIHARA and J. H. FENDLER, *J. Chem. Commun.* **90,** 279 (1984).
71. Y. WANG, A. SUNA, W. MAHLER and R. KASOWSKI, *J. Chem. Phys.* **87,** 7315 (1987).
72. N. F. BORRELLI, D. W. HALL, H. J. HOLLAND and D. W. SMITH, *J. appl. Phys.* **61,** 5399 (1987).
73. P. J. ANDERSON and P. L. MORGAN, *Trans Farad. Soc.* **60,** 930 (1964).
74. A. W. SEARCY, *J. Am. Ceram. Soc.* **70,** 155 (1983).
75. M. KIM, U. DAHMEN and A. W. SEARCY, *J. Am. Ceram. Soc.* **70,** 164 (1987).
76. R. ROY, *Ceramic Microstructures 86.* Int. Materials Symp.: Role of Interfaces, University of California, CA, July, p. 6 (1986).
77. D. M. ROY, R. ROY and R. A. ROY, *Mater. Lett.* **4,** 323 (1986).
78. G. W. KRIECHBAUM and P. KLEINSCHMIT, *Advanced Materials* **10,** 330 (1989).
79. A. FOJTIK, H. WELLER, U. KOCH and A. HENGLEIN, *Ber. Bunsen-Ges. Phys. Chem.* **88,** 969 (1984).
80. M. L. STEIGERWALD, A. P. ALIVISATOS, J. M. GIBSON, T. D. HARRIS, R. KORTAN, A. J. MULLER, A. M. THAYER, T. M. DUNCAN, D. C. DOUGLASS and L. E. BRUS, *J. Am. Chem. Soc.* **110,** 3046 (1988).
81. R. H. HOLM, *Acc. Chem. Res.* **10,** 427 (1977).
82. BOON K. TEO, K. KEATING and Y.-H. KAO, *J. Am. Chem. Soc.* **109,** 3494 (1987).
83. Y. WANG and N. HERRON, *J. Phys. Chem.* **91,** 257 (1987).
84. S. UMEMURA, *Final Report of the Ultrafine Particles Project, Research Development Corporation of Japan*, 5–2, Nagatacho 2-chome, Chiyoda-ku, Tokyo 100, Japan (1986).
85. H. WATANABE, *The Physics and Fabrikation of Microstructures and Microdevices* (edited by M. J. Kelly and C. Weisbuch), Springer-Verlag, Berlin, p. 158 (1986).
86. T. INOSHITA and H. WATANABE, *Optoelectron. Devices Technol.* **1,** 33 (1986).
87. T. INOSHITA and H. WATANABE, *Microclusters* (edited by S. Sugano, Y. Nishina and S. Ohnishi), Springer-Verlag, Tokyo, p. 281 (1987).
88. S. KASHU, E. FUCHITA, T. MANABE and T. HAYASHI, *Jap. J. appl. Phys.* **23,** L910 (1984).
89. T. TAKAGI, *Z. Phys.* **D3,** 272 (1986).
90. I. YAMADA, C. J. PALMSTROM, E. KENNEDY, J. W. MAYER, H. INOKAWA and T. TAKAGI, *Mater. Res. Soc. Symp. Proc.* **37,** 401 (1985).
91. T. INA, M. HANAI, H. ITO and Y. MINOWA, *Proceedings of the 5th International Conference on Ion and Plasma Assisted Techniques*, CEP Consultanta Ltd, Edinburgh, p. 16 (1985).
92. R. BIRRINGER, Ph.D. Thesis, University of the Saarland, FB 12.1 (1985).
93. E. HORT, Diploma Thesis, University of the Saarland, FB 12.1 (1985).
94. U. HERR, Diploma Thesis, University of the Saarland, FB 12.1 (1985).
95. Y. KAWAMURA, M. TAKAGI and M. AKAI, *Mater. Sci. Eng.* **98,** 449 (1988).
96. E. HELLSTERN, H. J. FECHT, Z. FU and W. L. JOHNSON, *J. appl. Phys.* **65,** 305 (1989).
97. P. H. SHINGU, B. HUANG, S. R. NISHITANI and S. NASU, *Suppl. Trans. Japan Inst. Metals* **29,** 3 (1988).
98. W. SCHLUMP and H. GREWE, In Proc. DGM Conf., *New Materials by Mechanical Alloying Techniques* (edited by E. Arzt and L. Schultz), Calw-Hirsau, Oct. 1988 (to be published).
99. M. J. LUTON, C. S. JAYANATH, M. M. DISKO, S. MATRAS and J. VALLONE, *Mater. Res. Soc. Symp. Proc.* **132,** 79 (1989).
100. E. HELLSTERN, H. J. FECHT, C. GARLAND and W. L. JOHNSON, *Mater. Res. Soc. Symp. Proc.* **132,** 137 (1989).
101. A. K. LEE, L. E. SANCHEZ-CALDERA, J. H. CHUN and N. P. SUH, *Mater. Res. Soc. Symp. Proc.* **132,** 87 (1989).
102. N. P. SUH, *ASME J. Eng. Ind.* **104,** 327 (1982).
103. N. P. SUH, N. TSUDA, M. G. MOON and N. SAKA, *ibid* **104,** 332 (1982).
104. J. P. RIVIÈRE, P. BROUILLAUD and J. F. DINHUT, *Radiation Effects and Defects in Solids* (in press).
105. S. K. MENON, T. R. JERVIS and M. NASTASI, *Mater. Res. Soc. Symp. Proc.* **80,** 269 (1987).

106. S. J. SAVAGE and F. H. FROES, *J. Metals* **36**, 20–33 (1984).
107. T. R. ANANTHARAMAN, Metallic glasses: production, properties and applications, *Trans. Tech.* p. 1 (1984).
108. J. BIGOT, *Preparation of Metallic Glasses and its Influence on the Properties*, Summer School on Amorphous Metals, World Scientific, Publ. Co., Singapore, p. 18 (1986).
109. H. BESTGEN, Microstructures of Amorphous and Microcrystalline Electrodeposited Co–P, Ni–P and Fe–P, *Proc. 5th Conf. Rap. Quenched Met.*, p. 443 (1985).
110. R. SONNENBERGER, H. BESTGEN and G. DIETZ, *Z. Phys. B.* **61**, 289 (1984).
111. R. SONNENBERGER, E. PFANNER and G. DIETZ, *Z. Phys. B.* **63**, 203 (1986).
112. G. MCMAHON and U. ERB, *Microstructural Science 1989*, IMS Conf. (in press).
113. S. VEPREK, Z. IQBAL, H. R. OSWALD and A. B. WEBB, *J. Phys.* **C14**, 295 (1981).
114. H. J. SCHLADITZ, *Z. Metall.* **59**, 18 (1968).
115. H. G. F. WILSDORF, O. T. INAL and L. E. MURR *Z. Metall.* **69**, 701 (1978).
116. B. M. GALLOIS, R. MATHUR, S. R. LEE and J. Y. YOO, *Mater. Res. Soc. Symp. Proc.* **132**, 49 (1989).
117. R. A. ROY and R. ROY, *Abstracts, Materials Research Society Annual Meeting*, Boston, Massachusetts, p. 377 (1982).
118. D. W. HOFFMAN, R. ROY and S. KOMARNENI, *Ceram. Bull.* **62**, 375 (1983).
119. R. A. ROY and R. ROY, *Mater. Res. Bull.* **19**, 169 (1984).
120. D. W. HOFFMAN, R. ROY and S. KOMARNENI, *J. Am. Ceram. Soc.* **67**, 468 (1984).
121. R. ROY, S. KOMARNENI and D. M. ROY, *Multiphase Ceramic Composites Made by Sol–Gel Technique. Better Ceramics Through Chemistry* (edited by C. J. Brinkler *et al.*), Elsevier, North Holland, p. 347 (1984).
122. D. W. HOFFMAN, R. ROY and S. KOMARNENI, *Mater. Lett.* **2**, 245 (1984).
123. D. W. HOFFMAN, S. KOMARNENI and R. ROY, *J. Mater. Sci. Lett.* **3**, 439 (1985).
124. Y. SUWA, R. ROY and S. KOMARNENI, *J. Am. Ceram. Soc.* **68**, C-238 (1985).
125. R. ROY, Y. SUWA and S. KOMARNENI, *Nucleation and Epitaxial Growth in Diphasic (Crystalline and Amorphous) Gels; Science of Ceramic Chemical Processing* (edited by L. L. Hench and D. R. Ulrich), Wiley, New York, p. 247 (1986).
126. Y. SUWA, S. KOMARNENI and R. ROY, *J. Mater. Sci. Lett.* **5**, 21 (1986).
127. Y. SUWA, R. ROY and S. KOMARNENI, *Mater. Sci. Eng.* **83**, 151 (1986).
128. G. VILMIN, S. KOMARNENI and R. ROY, *J. Mater. Sci.* **22**, 3556 (1987).
129. K. H. JO and K. H. YOON, *Mater. Res. Bull.* **24**, 1 (1989).
130. A. HENGLEIN and R. J. TAUSCH-TREML, *Colloid Interface Sci.* **80**, 84 (1981).
131. M. MOSTAFAVI, J. L. MARIGNIER, J. AMBLARD and J. BELLONI, *Radiat. Phys. Chem.* **34**, 605 (1989).
132. S. MOSSERI, A. HENGLEIN and E. JANATA, *J. Phys. Chem.* **93**, 6791 (1989).
133. A. HENGLEIN, *Chem. Phys. Lett.* **154**, 473 (1989).
134. TH. D. KOBLÉ, Diploma Thesis, University of the Saarland (1987).
135. H. J. WEBER, Diploma Thesis, University of Stuttgart (1989).
136. W. DICKENSCHEID, Diploma Thesis, University of the Saarland, FB 11 (1990).
137. H. HAHN and R. S. AVERBACK, *Appl. Phys. Lett.* **67**, 1113 (1990).
138. E. HORT, Diploma Thesis, University of the Saarland, FB 12.1 (1985).
139. F. TRAEGER and G. PULITZ, *Metal Clusters*, Springer Verlag, Berlin, p. 122 (1986).
140. H. FRITZSCHE, M. TANIELIAN, C. C. TSAI and P. J. GACZI, *J. appl. Phys.* **50**, 3366 (1979).
141. H. HAHN, J. LOGAS, TH. BIER and R. S. AVERBACK, *Mater. Res. Soc. Symp. Proc.* **132**, 35 (1989).
142. R. S. AVERBACK, H. HAHN, H. J. HÖFLER, J. L. LOGAS and T. C. SHEN, *Mater. Res. Soc. Symp.* **153**, 3 (1989).
143. R. J. BROOK, *Proc. Brit. Ceram. Soc.* **32**, 7 (1982).
144. R. W. SIEGEL, S. RAMASAMY, H. HAHN, LI ZONGQUAN, LU TING and R. GRONSKY, *J. Mater. Res.* **3**, 1367 (1988).
145. W. WUNDERLICH, Y. ISHIDA and R. MAURER, *Scr. Metall.* **24**, 403 (1990).
146. G. J. THOMAS, R. W. SIEGEL and J. A. EASTMAN, to be published.
147. G. WALLNER, E. JORRA, H. FRANZ, J. PEISL, R. BIRRINGER, H. GLEITER, T. HAUBOLD and W. PETRY, *Mater. Res. Soc. Symp. Proc.* **132**, 149 (1989).
148. E. JORRA, H. FRANZ, J. PEISL, G. WALLNER, W. PETRY, R. BIRRINGER, H. GLEITER and T. HAUBOLD, *Philos. Mag.* **B 60**, 159 (1989).
149. G. POROD, *Small Angle X-ray Scattering* (edited by O. Glatter and O. Kratky), Academic Press, London–New York, pp. 17–51 (1982).
150. O. GLATTER, *J. appl. Cryst.* **13**, 7 (1980).
151. J. BOURDON, *Growth and Properties of Metal Clusters*, Elsevier Publ. Co., Amsterdam (1980).
152. S. SUGANO, Y. NISHINA and S. OHNISHI, *Microclusters*, Springer Series on Materials Science, Vol. 4, Springer Verlag, Berlin, p. 126 (1987).
153. J. FRIEDEL, *Dislocations*, Pergamon Press, Oxford, p. 25 (1964).
154. R. W. SIEGEL and H. HAHN, *Nanophase Materials in Currents Trends in the Physics of Materials* (edited by M. Yussouff), World Scientific Publ. Co., Singapore, p. 403 (1987).
155. J. E. EPPERSON, R. W. SIEGEL, J. W. WHITE, T. E. KLIPPERT, A. NARAYANASAMY, J. A. EASTMAN and F. TROUW, *Mater. Res. Soc. Symp. Proc.* **132**, 15 (1989).
156. U. HERR, Diploma Thesis, University of the Saarland, FB 12.1 (1985).
157. V. I. NOVIKOV, S. V. SVIRIDA and A. N. SEMENICHIN, *Soviet Powder Metallurgy and Metal Ceramics* **11**, 36 (1984).

158. V. I. NOVIKOV, S. V. SVIRIDA, L. I. TRUSOV, V. N. GRYAZNOV and T. P. GELEISHVILI, *Metallofizika* **6,** 114 (1984).
159. H.-E. SCHAEFER, W. ECKERT, O. STRITZKE, R. WÜRSCHUM and W. TEMPL, *Positron Annihilation* (edited by L. Dorikens-Vanpraet, M. Dorikens and D. Segers), World Scientific Publ. Co., Singapore, p. 79 (1989).
160. H.-E. SCHAEFER, Habilitationsschrift University of Stuttgart (1981).
161. C. LANDSBERGER, G. WALLNER and J. PEISL, private communication.
162. A. P. MILLS and R. J. WILSON, *Phys. Rev.* **B26,** 490 (1982).
163. O. STRITZKE, R. WÜRSCHUM, W. ECKERT, R. MAURER and H.-E. SCHAEFER, *Verhandl. DPG* (VI) **23,** M-26.4 (1988).
164. V. G. GRYAZNOV, L I. TRUSOV, V. N. LAPOVOK, V. I. NOVIKOV, E. V. KNYAZEV, T. P. GELEISHVILI and M. V. KVERNADZE, *Sov. Phys. Sol. State* **25,** 1315 (1983).
165. V. I. NOVIKOV, L. I. TRUSOV, V. N. LAPOVOK and T. P. GELEISHVILI, *Soviet Powder Metallurgy and Metal Ceramics* **23,** 355 (1984).
166. V. I. NOVIKOV, L. I. TRUSOV, V. I. LAPOVOK and T. P. GELEISHVILI, *Soviet Powder Metallurgy and Metal Ceramics* **3,** 29 (1984).
167. V. I. NOVIKOV, L. I. TRUSOV, V. N. LAPOVOK and T. P. GELEISHVILI, *Soviet Powder Metallurgy and Metal Ceramics* **23,** 195 (1984).
168. L. I. TRUSOV, J. A. VOSKRESENSKIJ, V. I. NOVIKOV, V. N. LAPOVOK, V. N. TROIZKIJ, V. I. CUKALIN and T. V. REZCIKOVA, *Soviet Powder Metallurgy and Metal Ceramics* **10,** 34 (1987).
169. L. I. TRUSOV, J. A. VOSKRESENSKIJ, J. A. REPIN, V. I. NOVIKOV, S. V. SVIRIDA and A. N. SEMENICHIN, *Solid State Physics* **29,** 2061 (1987).
170. M. J. LUTON, C. S. JAYANTH, M. M. DISKO, S. MATRAS and J. VALLONE, *Mater. Res. Soc. Symp. Proc.* **132,** 79 (1989).
171. R. W. SIEGEL, H. HAHN, S. RAMASAMY, L. ZONGQUAN, L. TING and R. GRONSKY, *J. Phys.* **49,** C5–681 (1988).
172. H. HAHN, J. LOGAS and R. S. AVERBACK, *J. Mater. Res.* **5,** 216 (1990).
173. M. R. FITZSIMMONS and S. L. SASS, *J. Phys.* **49,** C5–71 (1988).
174. K. R. MILKOVE, P. LAMARRE, F. SCHMUECKLE, M. D. VAUDIN and S. L. SASS, *J. Phys.* **46,** C4–71 (1985).
175. V. TIENSUU, S. ERGUN and L. ALEXANDER, *J. appl. Phys.* **35,** 1718 (1964).
176. F. BETTS and A. BIENENSTOCK, *J. appl. Phys.* **143,** 4591 (1972).
177. H. GLEITER, *Mater. Sci. Eng.* **52,** 91 (1982).
178. C. N. J. WAGNER, T. B. LIGHT, N. C. HALLER and W. E. LUKENS, *J. appl. Phys.* **39,** 3690 (1968).
179. J. A. EASTMAN and L. J. THOMPSON, to be published.
180. T. B. LIGHT and C. N. J. WAGNER, *J. appl. Cryst.* **1,** 199 (1968).
181. K. R. MILKOVE, P. LAMARRE, F. SCHMÜCKLE, M. D. VAUDIN and S. L. SASS, *J. Phys.* **46,** C4–71 (1985).
182. J. WONG, *Mater. Sci. Eng.* **80,** 107 (1986).
183. P. A. LEE, P. H. CITRIN and R. EISENBERGER, *Rev. Mod. Phys.* **53,** 769 (1981).
184. G. STEGEMANN, JÜL Report 2075 (1986), KFA Jülich, ISSN 0366-0885.
185. H. E. SCHAEFER, R. WÜRSCHUM, M. SCHEYTT, R. BIRRINGER and H. GLEITER, *J. Mater. Sci. Forum* **15–18,** 955 (1987).
186. R. BIRRINGER, U. HERR and H. GLEITER, *Suppl. Trans. Japan Inst. Metals* **27,** 43 (1986).
187. X. ZHU, R. BIRRINGER, U. HERR and H. GLEITER, *Phys. Rev.* **B 35,** 9085 (1987).
188. D. G. STEARNS and M. B. STEARNS, *Topic of Current Physics, Vol. 40. Microscopic Methods in Metals*, Springer, Berlin (1986).
189. F. SPAEPEN, *Mater. Res. Soc. Symp. Proc.* **132,** 127 (1989).
190. T. HAUBOLD, R. BIRRINGER, B. LENGELER and H. GLEITER, *Phys. Lett.* **135,** 461 (1989).
191. J. P. RIVIÈRE, P. BOULLAUD and J. F. DINHUT, *Radiation Effects and Defects in Solids* (in press).
192. H. E. SCHAEFER, R. GUGELMEIER, M. SCHMOLZ and A. SEEGER, *Microstructural Characterization of Materials by Non-Microscopical Techniques* (edited by N. Hessel Andersen *et al.*), Risø National Laboratory, Roskilde, p. 489 (1984).
193. W. WEILER and H. E. SCHAEFER, *J. Phys.* **F 15,** 1651 (1985).
194. H. E. SCHAEFER, *Phys. Status Solidi* (*a*) **102,** 47 (1987).
195. H. E. SCHAEFER, R. WÜRSCHUM, R. SCHWARZ, D. SLOBODIN and S. WAGNER, *Appl. Phys.* **A40,** 145 (1986).
196. H. E. SCHAEFER and R. WÜRSCHUM, *Phys. Lett.* **A119,** 370 (1987).
197. H. E. SCHAEFER, R. WÜRSCHUM, M. SCHEYTT, R. BIRRINGER and H. GLEITER, *Mater. Sci. Forum* **15–18,** 955 (1987).
198. R. WÜRSCHUM, M. SCHEYTT and H. E. SCHAEFER, *Phys. Status Solidi* (*a*) **102,** 119 (1987).
199. H. E. SCHAEFER, R. WÜRSCHUM, R. BIRRINGER and H. GLEITER, *Phys. Rev.* **B38,** 9549 (1988).
200. H. E. SCHAEFER, R. WÜRSCHUM, R. BIRRINGER and H. GLEITER, *J. Less-Common Metals* **140,** 161 (1988).
201. K. L. MERKLE and D. J. SMITH, *Phys. Rev. Lett.* **59,** 2887 (1987).
202. H. E. SCHAEFER, W. ECKERT, O. STRITZKE, R. WÜRSCHUM and W. TEMPL, *Positron Annihilation* (edited by L. Dorikens-Vanpraet, M. Dorikens and D. Segers), World Scientific Publ. Co., Singapore, p. 79 (1989).
203. K.-P. ARNOLD, C. BAINES, K.-P. DÖRING, K. FÜRDERER, M. GLADISCH, D. HERLACH, M. KRENKE, G. MAJER, J. MAJOR, H.-J. MUNDINGER, J. ROSENKRANZ, W. SCHÄFER, L. SCHIMMELE, M. SCHMOLZ, W. SCHWARZ and A. SEEGER, *SIN Newsletter* **19,** 91 (1987).
204. A. MÖSSLANG, H. GRAF, G. BALZER, E. RECKNAGEL, A. WEIDINGER and TH. WICHERT, *Phys. Rev.* **27,** 2674 (1983).
205. U. HERR, J. JING, R. BIRRINGER, U. GONSER and H. GLEITER, *Appl. Phys. Lett.* **50,** 472 (1987).

206. R. V. POUND, G. B. BENEDECK and R. DREVER, *Phys. Rev. Lett.* **7,** 405 (1961).
207. D. L. WILLIAMSON, S. BUCKSHPAN and R. INGALLS, *Phys. Rev.* **B6,** 4194 1972).
208. J. TYSON, A. OWENS and J. C. WALKER, *J. Magn. Mater.* **35,** 126 (1983).
209. J. KORECKI and U. GRADMANN, *Phys. Rev. Lett.* **55,** 2491 (1985).
210. American Institute of Physics Handbook, 3rd ed, American Institute of Physics, New York, p. 4–115 (1972).
211. S. RAMASAMY, J. JIANG, H. GLEITER, R. BIRRINGER and U. GONSER, *Solid State Comm.* **74,** 851 (1990).
212. J. JING, Ph.D. Thesis, University of the Saarland, FB 12.1 (1989).
213. R. KIRCHHEIM, T. MÜTSCHELE, W. KIENINGER, H. GLEITER, R. BIRRINGER and T. D. KOBLÉ, *Mater. Sci. Eng.* **99,** 457 (1988).
214. T. MÜTSCHELE and R. KIRCHHEIM, *Scr. Metall.* **21,** 135 (1987).
215. R. GRIESSEN, *Phys. Rev.* **B 30,** 7575 (1983).
216. T. MÜTSCHELE and R. KIRCHHEIM, *Scr. Metall.* **21,** 1101 (1987).
217. Z. IQBAL, A. P. WEBB and S. VEBREK, *Appl. Phys. Lett.* **36,** 163 (1980).
218. S. VEPREK, Z. IQBAL, H. R. OSWALD and A. P. WEBB, *J. Phys.* **C14,** 295 (1981).
219. M. H. BRODSKY, *Light Scattering in Solids. Topics in Applied Physics* (edited by M. Cardona), Springer-Verlag, Berlin, Vol. 8, p. 179 (1975).
220. G. KANELLIS, J. F. MORHANGE and M. BALKANSKI, *Phys. Rev.* **B21,** 1543 (1980).
221. C. A. MELENDRES, A. NARAYANASAMY, V. A. MARONI and R. W. SIEGEL, *J. Mater. Res.* **4,** 1246 (1989).
222. U. HERR, J. JING, U. GONSER and H. GLEITER, *Solid State Commun.* (in press).
223. R. BIRRINGER, U. HERR and H. GLEITER, *Suppl. Trans. Japan Inst. of Metals* **27,** 43 (1986).
224. F. C. LARCHE and J. W. CAHN, *Acta Metal.* **21,** 1051 (1973).
225. F. C. LARCHE and J. W. CAHN, *Acta Metal.* **26,** 1579 (1978).
226. J. W. CAHN and F. C. LARCHE, *Acta Metal.* **32,** 1915 (1984).
227. W. C. JOHNSON and J. I. D. ALEXANDER, *J. appl. Phys.* **59,** 2735 (1986).
228. A. KELLY and R. B. NICHOLSON, *Prog. Mater. Sci.* **10,** 276 (1963).
229. P. H. SHINGU, B. HUANG, S. R. NISHITANI and S. NASU, *Suppl. Trans. Japan Inst. Metals* **29,** 3 (1988).
230. A. HENGELEIN, *Chem. Rev.* **89,** 1861 (1989).
231. R. P. ANDRES, R. S. AVERBACK, W. L. BROWN, L. E. BRUS, W. A. GODDARD, A. KALDOR, S. G. LOUIE, M. MOSCOVITS, P. S. PEERCY, S. J. RILEY, R. W. SIEGEL, F. SPAEPEN and Y. WANG, *J. Mater. Res.* **4,** 740 (1989).
232. L. E. BRUS, *J. Phys. Chem.* **90,** 2555 (1986).
233. L. BRUSS, *IEEE J. Quantum Electron* **QE-22,** 1909 (1986).
234. H. WELLER, A. FOJTIK and A. HENGLEIN, *Chem. Phys. Lett.* **117,** 485 (1985).
235. L. BRUS, *New J. of Chem.* **11,** 123 (1987).
236. Y. WANG, A. SUNA, W. MAHLER and R. KASOWSKI, *J. Chem. Phys.* **87,** 7315 (1987).
237. M. L. STEIGERWALD, A. P. ALIVISATOS, J. M. GIBSON, T. D. HARRIS, R. KORTAN, A. J. MULLER, A. M. THAYER, T. M. DUNCAN, D. C. DOUGLAS and L. E. BRUS, *J. Am. Chem. Soc.* **110,** 3046 (1988).
238. Y. NOSAKA, K. YAMAGUCHI, H. MIYAMA and H. HAYASHI, *Chem. Lett.* **605,** 1988.
239. CH.-H. FISCHER and A. HENGLEIN, *J. Phys. Chem.* **93,** 5578 (1989).
240. D. HAYES, O. I. MICIC, M. T. NENADOVIC, V. SWAYAMBUNATHAN and D. MEISEL, *J. Phys. Chem.* **93,** 4603 (1989).
241. N. HERRON, Y. WANG, M. EDDY, G. STUCKY, D. E. COX, K. MOLLER and T. BEIN, *J. Am. Chem. Soc.* **111,** 530 (1989).
242. R. K. JAIN and R. C. LIND, *J. Opt. Soc. Am.* **73,** 647 (1983).
243. T. ROUSSIGNOL, D. E. RICARD, J. LUKASIK and C. FLYTZANIS, *J. Opt. Soc. Am.* **B4,** 5 (1987).
244. G. R. OLBRIGHT, N. TEYGHAMBARIAN and S. W. KOCH, *Opt. Lett.* **12,** 413 (1987).
245. Y. WANG and W. MAHLER, *Opt. Comm.* **61,** 233 (1987).
246. E. S. HILINSKI, P. A. LUCAS and Y. WANG, *J. Chem. Phys.* **89,** 3435 (1988).
247. T. TAKAGAHARA and E. HANAMURA, *Phys. Rev. Lett.* **56,** 2533 (1986).
248. D. S. CHEMLA and D. A. B. MILLER, *Opt. Lett.* **11,** 522 (1986).
249. L. BANYAI and S. W. KOCH, *Phys. Rev. Lett.* **57,** 2722 (1986).
250. D. FORNASIERO and F. GRIESER, *J. Chem. Phys.* **87,** 3213 (1987).
251. P. MARQUARDT and G. NIMTZ, *Phys. Rev.* **B 40,** 7996 (1989).
252. L. SPANHEL, H. WELLER and A. HENGLEIN, *J. Am. Chem. Soc.* **109,** 6632 (1987).
253. L. SPANHEL, A. HENGLEIN and H. WELLER, *Ber. Bunsen-Ges. Phys. Chem.* **91,** 1359 (1987).
254. L. SPANHEL, H. WELLER, A. FOJTIK and A. HENGLEIN, *Ber. Bunsen-Ges. Phys. Chem.* **91,** 88 (1987).
255. A. HENGLEIN, M. GUTIÉRREZ, H. WELLER, A. FOJTIK and J. JIRKOVSKY, *Ber. Bunsen-Ges. Phys. Chem.* **93,** 593 (1989).
256. J. JIANG, S. RAMASAMY, U. GONSER and H. GLEITER, to be published.
257. P. AYYUB, M. MUSTANSI, V. R. PALKAR and R. VIJAYARAGHAVAN, *J. Phys. C. Solid State Phys.* **21,** 2229 (1988).
258. H. N. OK and J. G. MULLEN, *Phys. Rev.* **168,** 550 (1968).
259. D. SCHROEER and W. TRIFTSHÄUSER, *Phys. Rev. Lett.* **20,** 1242 (1968).
260. W. KEUNE, J. LAUER, U. GONSER and D. L. WILLIAMSON, *J. Phys.* (Suppl.) **3,** C2–69 (1979).
261. R. BIRRINGER, H. HAHN, H. HÖFLER, J. KARCH and H. GLEITER, *Defect and Diffusion Forum* **59,** 17 (1988).
262. J. HORVATH, R. BIRRINGER and H. GLEITER, *Solid State Comm.* **62,** 391 (1987).

263. J. HORVATH, DIMETA-88, International Conference on Diffusion in Metals and Alloys, Balatonfüred, Hungary, September 5–9, 1988; to be published in *Material Science Forum.*
264. H. GLEITER, *Mater. Sci. Eng.* **52,** 91 (1982).
265. R. KIRCHHEIM, F. SOMMER and G. SCHLUCKEBIER, *Acta Metall.* **30,** 1059 (1982).
266. R. KIRCHHEIM, *Acta Metall.* **30,** 1069 (1982).
267. R. KIRCHHEIM, *Acta Metall.* **35,** 271 (1987).
268. R. KIRCHHEIM and U. STOLZ, *Acta Metall.* **35,** 281 (1987).
269. T. MÜTSCHELE and R. KIRCHHEIM, *Scr. Metall.* **21,** 135 (1987).
270. R. KIRCHHEIM, T. MÜTSCHELE, W. KIENINGER, H. GLEITER, R. BIRRINGER and T. D. KOBLÉ, *Mater. Sci. Eng.* **99,** 457 (1988).
271. T. MÜTSCHELE and R. KIRCHHEIM, *Scr. Metall.* **21,** 1101 (1987).
272. T. MÜTSCHELE, Ph.D. Thesis, University of Stuttgart (1987).
273. W. DICKENSCHEID, Diploma Thesis, University of the Saarland, FB 11 (1990).
274. A. M. GLAESER and J. W. EVANS, *Acta Metall.* **34,** 1545 (1986).
275. P. G. SHEWMON and G. MEYRICK, *Interface Migration and Control of Microstructure* (edited by C. S. Pande, D. A. Smith, A. H. King and J. Walter), ASM Publications, p. 7 (1986).
276. C. A. HANDWERKER, *Diffusion Phenomena in Thin Films* (edited by D. Gupta and P. Ho), Noyes Publications, New York, p. 245 (1988).
277. H. J. HÖFLER, H. HAHN and R. S. AVERBACK, unpublished.
278. R. S. AVERBACK, H. HAHN, H. J. HÖFLER, J. L. LOGAS and T. C. SHEN, *Mater. Res. Soc. Symp.* **153,** 3 (1989).
279. S. SCHUMACHER, R. BIRRINGER, R. STRAUSS and H. GLEITER, *Acta Metall.* **37,** 2485 (1989).
280. N. BLOEMBERGEN, E. M. PURCELL and R. V. POUND, *Phys. Rev.* **73,** 679 (1948).
281. P. PANISSOD and T. MIZOGUCHI, *Proceedings of the 4th International Conference on Rapidly Quenched Metals* (edited by T. Masumoto and Y. Susuki), Sendai, p. 1621 (1982).
282. P. PANISSOD, *Microscopic Methods in Metals* (edited by U. Gonser), Springer Verlag Berlin, p. 365 (1986).
283. L. N. PARITSKAYA, V. I. NOVIKOV and V. S. KRUZHANOV, *Soviet Powder Metallurgy and Metal Ceramics* **21,** 554 (1982).
284. J. HORVÀTH, J. OTT, K. PFAHLER and W. ULFERT, *Mater. Sci. Eng.* **97,** 409 (1988).
285. J. HORVÀTH, K. PFAHLER, W. ULFERT, W. FRANK and H. KRONMÜLLER, *Mater. Sci. Forum* **15–18,** 523 (1987).
286. H. HAHN, H. J. HÖFLER and R. S. AVERBACK, DIMETA-88, International Conference on Diffusion in Metals and Alloys, Balatonfüred, Hungary, September 5–9, 1988; to be published in *Materials Science Forum.*
287. J. RUPP and R. BIRRINGER, *Phys. Rev.* **B 36,** 7888 (1987).
288. E. HELLSTERN, H. J. FECHT, Z. FU and W. L. JOHNSON, *J. appl. Phys.* **65,** 305 (1989).
289. G. GOLL and H. v. LÖHNEYSEN, private communication.
290. D. KORN, A. MORSCH, R. BIRRINGER, W. ARNOLD and H. GLEITER, *J. Phys.* **49,** C5–769 (1988).
291. H. J. FECHT, *Acta Metall.* (in press).
292. D. WOLF, *Phil. Mag.* **B 59,** 667 (1989).
293. J. H. ROSE, J. R. SMITH, F. GUINEA and J. FERRANTE, *Phys. Rev.* **B 29,** 2963 (1984).
294. H. J. FECHT, E. HELLSTERN, Z. FU and W. L. JOHNSON, submitted to *Met. Trans.*
295. T. H. K. BARRON, J. G. COLLINS and G. K. WHITE, *Adv. Phys.* **29,** 609 (1980).
296. H. J. KLAM, H. HAHN and H. GLEITER, *Acta Metall.* **35,** 2101 (1987).
297. M. R. FITZSIMONS, E. BURKEL and S. L. SASS, *Phys. Rev. Lett.* **61,** 2237 (1988).
298. R. BIRRINGER and H. GLEITER, *Advances in Materials Science, Encyclopedia of Mat. Sci. and Eng.* (edited by R. W. Cahn), Pergamon Press, Oxford, p. 339 (1988).
299. J. E. SHELBY, *J. Non-Cryst. Solids* **34,** 111 (1979).
300. S. VEPREK, Z. IQBAL, H. R. OSWALD and A. P. WEBB, *J. Phys.* **C 14,** 295 (1981).
301. E. C. FREEMAN and W. PAUL, *Phys. Rev.* **B 20,** 716 (1979).
302. G. E. BECKER and G. W. GOEBELI, *J. Chem. Phys.* **38,** 2942 (1963).
303. L. CHEN, J. TAUC and Z. VARDENY, *Phys. Rev.* **B 39,** 5121 (1989).
304. R. BIRRINGER, U. HERR and H. GLEITER, *Suppl. Trans. Japan Inst. Metals* **27,** 43 (1986).
305. R. Z VALIEV, R. R. MULYUKOV, KH. YA. MULYUKOV, V. I. NOVIKOV and L. I. TRUSOV, *Pisma v szurnal teckhnicheskoi fiziki* **15,** 78 (1989).
306. R. Z. VALIEV, YA. D. VISHNYAKOV, R. R. MULYUKOV and G. S. FAINSHTEIN, *Physica status solidi* (in press).
307. W. GEIBEL, Diploma Thesis, University of the Saarland, FB 12.1 (1989).
308. A. COWEN, B. STOLZMANN, R. A. AVERBACK and H. HAHN, *J. appl. Phys.* **61,** 3317 (1987).
309. Y. YOSHIZAWA, K. YAMAUCHI and S. OGUMA, European Patent 0 271 657-A2, 22.06.1988.
310. H. J. WEBER, Diploma Thesis, University of Stuttgart (1989).
311. U. KRAG, Diploma Thesis, University of the Saarland (1990).
312. D. KORN, A. MORSCH, R. BIRRINGER, W. ARNOLD and H. GLEITER, *J. Phys.* **49,** C5–769 (1988).
313. J. PROVAN and O. BAMIRO, *Acta Metall.* **25,** 309 (1977).
314. D. WOLF and J. F. LUTSKO, *Phys. Rev. Lett.* **60,** 1170 (1988).
315. M. S. DAW and M. I. BASKES, *Phys. Rev.* **B 29,** 6443 (1984).
316. J. F. LUTSKO, D. WOLF and S. YIP, *J. Phys.* **49,** C5–375 (1988).

317. R. W. SIEGEL and H. HAHN, *Current Trends in Physics of Materials* (edited by M. Yousouff), World Scientific, Singapore, p. 403 (1987).
318. J. KARCH, R. BIRRINGER and H. GLEITER, *Nature* **330,** 556 (1987).
319. R. W. SIEGEL, H. HAHN, S. RAMASAMY, L. ZONGQUAN, L. TING and R. GRONSKY, *J. Phys.* C5 **49,** 681 (1988).
320. Z. LI, S. RAMASAMY, H. HAHN and R. W. SIEGEL, *Mater. Lett.* **6,** 195 (1988).
321. K. H. JACK, *High-Technology Ceramics, Past, Present and Future; Ceramics and Civilisation* (edited by W. D. Kingery), Vol. 3, American Ceramic Society, Westerville, p. 259 (1986).
322. N. CLAUSSEN and A. H. HEUER, *Encyclopedia of Materials, Science and Engineering* (edited by M. B. Bever), Pergamon and MIT, p. 5129 (1986).
323. F. F. LANGE, *J. Mater. Sci.* **17,** 225 (1982).
324. R. C. GARVIE, R. H. HANNINK and R. T. PASCOE, *Nature* **258,** 703 (1975).
325. R. W. CAHN, *Nature* **332,** 761 (1988).
326. L. I. TRUSOV, V. I. NOVIKOV, I. A. REPIN, J. J. KAZILIN and V. J. GANELIN, *Metallofizika* **10,** 104 (1988).
327. V. I. NOVIKOV, L. I. TROSOV, V. N. LAPOVOK, A. I. KAPUSTIN, S. V. SVIRIDA and E. N. YAKOVLEV, *Soviet Powder and Metal Ceramics* **24,** 735 (1985).
328. V. I. NOVIKOV, S. V. SVIRIDA, L. I. TRUSOV, V. N. LAPOVOK, V. G. GRJAZNOV and T. P. GELEISHVILI, *Metallofizika* **6,** 114 (1984).
329. A. H. CHOKHSI, A. ROSEN, J. KARCH and H. GLEITER, *Scr. Metall.* **23,** 1679 (1989).
330. E. O. HALL, *Proc. Phys. Soc. Lond.* **B 64,** 747 (1951).
331. N. J. PETCH, *J. Iron Steel Inst.* **174,** 25 (1953).
332. H. J. SCHLADITZ, *Z. Metallk.* **59,** 18 (1968).
333. H. G. F. WILSDORF, O. T. INAL and L. E. MURR, *Z. Metallk.* **69,** 701 (1969).
334. V. I. NOVIKOV, S. V. SVIRIDA, L. I. TRUSOV, V. N. LAPOVOK, V. M. GRYAZNOV and T. P. GELEISHVILI, *Metallofizika* **6,** 114 (1984).
335. V. N. LAPOVOK, V. I. NOVIKOV, S. V. SVIRIDA, A. N. SEMENIKHIN and L. I. TRUSOV, *Fiz. Met. Metalloved.* **57,** 718 (1984).
336. V. I. NOVIKOV, S. V. SVIRIDA, L. I. TRUSOV, V. N. LAPOVOK, V. P. FEDOTOV and J. A. VOSKRESENSKIJ, *Metallofizika* **6,** 97 (1984).
337. V. I. NOVIKOV, L. I. TRUSOV, V. N. LAPOVOK and T. P. GELEISHVILI, *Soviet Powder Metallurgy and Metal Ceramics* **23,** 355 (1984).
338. V. I. NOVIKOV, P. F. RELUSHKO, L. I. TRUSOV and YU. A. LOPUKHOV, *Sov. Phys. Solid State* **26(1),** 2071 (1984).
339. M. B. BRODSKY, *J. Phys.* C **5,** 349 (1984).
340. V. N. LAPOVOK, V. I. NOVIKOV, S. V. SVIRIDA, A. N. SEMENIKHIN and L. I. TRUSOV, *Sov. Phys. Solid State* **25(6),** 1063 (1983).
341. M. KLINGEL, R. BIRRINGER and H. GLEITER, unpublished.
342. K. E. EASTERLING and P. SWANN, *Acta Metall.* **19,** 117 (1971).
343. M. UMEMOTO and W. S. OWEN, *Metall. Trans.* **5,** 2041 (1974).
344. Y. INOKUKI and B. CANTOR, *Acta Metall.* **30,** 343 (1982).
345. W. KRAUSS, S. K. PABI and H. GLEITER, *Acta Metall.* **37,** 25 (1989).
346. V. N. LAPOVOK, V. I. NOVIKOV, S. V. SVIRIDA, A. N. SEMENIKHIN and L. I. TRUSOV, *Sov. Phys. Sol State* **25,** 1063 (1983).
347. S. S. GORELIK and M. S. BLANTER, *Izv. Akad. Nauk SSSR, Metally* **2,** 90 (1982).
348. L. I. TRUSOV, V. G. GRYAZNOV, V. I. NOVIKOV and T. P. GELEISHVILI, *Sov. Phys. Solid State* **27(9),** 1634 (1985).
349. V. I. NOVIKOV, V. YA. GANELIN, L. I. TRUSOV, V. G. GRYAZNOV, V. P. LAPOVOK and S. É. ZEER, *Sov. Phys. Solid State* **28(4),** 705 (1986).
350. C. GOTTSCHALK, K. SMIDODA and H. GLEITER, *Acta Metall.* **28,** 1653 (1980).
351. H. GLEITER, *Acta Metall.* **27,** 1754 (1979).
352. V. I. NOVIKOV, L. I. TRUSOV, V. N. LAPOVOK and T. P. GELEISHVILI, *Poroshk. Metall.* **5,** 30 (1984).
353. V. I. NOVIKOV and V. K. PORTNOI, *Superplasticity of Ultra-Fine-Grained Materials*, Metallurgiya, Moscow, p. 12 (1981).
354. V. I. NOVIKOV, L. I. TRUSOV, V. N. LAPOVOK and T. P. GELEISHVILI, *Poroshk. Metall.* **3,** 29 (1984).
355. V. N. LAPOVOK, V. I. NOVIKOV, S. V. SVIRIDA, A. N. SEMENIKHIN and L. I. TRUSOV, *Fiz. Tverd. Tela* (Leningrad) **25,** 1846 (1983), *Sov. Phys. Solid State* **25,** 1063 (1983).
356. S. S. GORELIK and M. S. BLANTER, *Izv. Akad. Nauk. SSSR Metally* **2,** 90 (1982).
357. J. P. RIVIÈRE, P. BOUILLAUD and J. F. DINHUT, *Radiation Effects and Defects in Solids 1990* (in press).
358. B. W. BATTERMANN and C. S. BARRETT, *Phys. Rev. Lett.* **13,** 390 (1964).
359. M. GORINGE and U. VALDRE, *Phys. Rev. Lett.* **14,** 823 (1965).
360. M. WELLER, J. DIEHL and H. E. SCHAEFER, *Phil. Mag. A*, (in press).
361. T. S. KÊ, *Suppl. Trans. Japan Inst. Metals* **27,** 679 (1986).
362. K. IWASAKI, *Phys. Stat. Sol.* (*a*) **90,** K 35 (1985).
363. J. B. ADAMS, W. G. WOLFER and S. M. FOILES, *Phys. Rev.* **B 40,** 9479 (1989).
364. H. J. WEBER, Diploma Thesis, University of Stuttgart (1989).
365. P. KRAG, Diploma Thesis, University of the Saarland, FB 12.1 (1990).
366. R. BIRRINGER, private communication.

367. H. HOFFMANN, *Festkörperprobleme: Advances in Solid State Physics* (edited by J. Treusch), Vieweg, Braunschweig, Vol. XXII, p. 255 (1982).
368. K. FUCHS, *Proc. Camb. Philos. Soc.* **34,** 100 (1983).
369. Y. NAMBA, *Japan J. appl. Phys.* **9,** 1326 (1970).
370. A. F. MAYADAS, M. SHATZKES and J. F. JANAK, *Appl. Phys. Lett.* **14,** 345 (1969).
371. A. F. MAYADAS and M. SHATZKES, *Phys. Ref.* **B 1,** 1382 (1970).
372. F. WARKUSZ, *Electrocomponent Sci. Technol.* **9,** 105 (1981).
373. F. WARKUSZ, Electrical and mechanical properties of thin metal films, Size effects, *Prog. Surf. Sci.* **10,** 287 (1980).
374. C. R. TELLIER and A. J. TOSSER, *Size Effects in Thin Films*, Elsevier, Amsterdam (1982).
375. A. F. MAYADAS and M. SHATZKES, *Phys. Rev.* **B1,** 1382 (1970).
376. C. R. TELLIER, *Thin Solid Films* **51,** 311 (1978).
377. F. WARKUSZ, *Thin Solid Films* **161,** 1 (1988).
378. G. REISS, J. VANCEA and H. HOFFMANN, *Phys. Rev. Lett.* **56,** 2100 (1986).
379. V. R. PALKAR and M. S. MULTANI, *Mater. Res. Bull.* **14,** 1353 (1979).
380. M. S. MULTANI, .V R. PALKAR, S. G. GOKARN and R. VIJAYARAGHAVAN, *Mater. Res. Bull.* **17,** 101 (1982).
381. P. AYYUB, M. S. MULTANI, M. R. SRINIVASAN, A. ROY and H. C. JAIN, *Phys. Rev.* **B 32,** 2835 (1985).
382. M. S. MULTANI, N. G. NANADIKAR and A. V. GURJAR, *Mater. Res. Bull.* **14,** 1251 (1979).
383. M. S. MULTANI, P. AYUUB, V. R. PALKAR and R. VIJAYARAGHAVAN, *Bull. Mater. Sci.* **6,** 327 (1984).
384. O. VERGARA, D. HEITKAMP and H. V. LÖHNEYSEN, *J. Phys. Chem. Solids* **45,** 251 (1984).
385. R. DENTON, B. MÜHLSCHLEGEL and D. J. SCALAPINO, *Phys. Rev.* **B 7,** 3589 (1973).
386. G. GOLL, Diploma Thesis, University Karlsruhe (1988).
387. R. BIRRINGER and J. KARCH, *Ceram. Int.* (in press).
388. H. HAHN, J. LOGAS, H. J. HOEFLER and R. S. AVERBACK, *Mater. Res. Soc. Symp.* (in press).
389. J. W. EDINGTON, K. S. MELTON and C. P. CUTLER, *Prog. Mater. Sci.* **21,** 61 (1976).
390. A. H. HEUER, D. J. SELLERS and W. H. RHODES, *J. Am. Ceram. Soc.* **52,** 468 (1969).
391. J. D. FRIDEZ, C. CARRY and A. MOCELLIN, *Advances in Ceramics, Vol. 10* (edited by W. D. Kingery), American Ceramics Society, Columbus, OH (1984).
392. K. R. VENKATACHARI and R. RAJ, *J. Am. Ceram. Soc.* **69,** 135 (1986).
393. J.-G. WANG and R. RAJ, *J. Am. Ceram. Soc.* **67,** 399 (1984).
394. J. JIANG, S. RAMASAMY, R. BIRRINGER, U. GONSER and H. GLEITER, to be published.
395. J. WEISSMÜLLER, R. BIRRINGER and H. GLEITER, *Phys. Lett.* **A 145,** 130 (1990).
396. J. JING, A. KRÄMER, R. BIRRINGER, H. GLEITER and U. GONSER, *J. Non-cryst. Solids* **113,** 167 (1989).